

Summer 2018

Charge Dynamics in the Metallic and Superconducting States of the Electron-Doped 122-Type Iron Arsenides

Zhen Xing

College of William and Mary - Arts & Sciences, zxing@email.wm.edu

Follow this and additional works at: <https://scholarworks.wm.edu/etd>



Part of the [Physics Commons](#)

Recommended Citation

Xing, Zhen, "Charge Dynamics in the Metallic and Superconducting States of the Electron-Doped 122-Type Iron Arsenides" (2018). *Dissertations, Theses, and Masters Projects*. Paper 1530192704.

<http://dx.doi.org/10.21220/s2-b785-e450>

This Dissertation is brought to you for free and open access by the Theses, Dissertations, & Master Projects at W&M ScholarWorks. It has been accepted for inclusion in Dissertations, Theses, and Masters Projects by an authorized administrator of W&M ScholarWorks. For more information, please contact scholarworks@wm.edu.

Charge Dynamics in the Metallic and Superconducting States of the Electron-doped
122-type Iron Arsenides

Zhen Xing

Harbin, Heilongjiang, China

Master of Science, College of William & Mary, 2013
Bachelor of Science, Harbin Institute of Technology, 2011

A Dissertation presented to the Graduate Faculty
of The College of William & Mary in Candidacy for the Degree of
Doctor of Philosophy

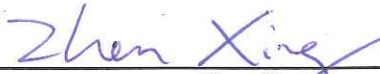
Department of Physics

College of William & Mary
May, 2018

APPROVAL PAGE

This Dissertation is submitted in partial fulfillment of
the requirements for the degree of

Doctor of Philosophy



Zhen Xing

Approved by the Committee, March 2018



Committee Chair

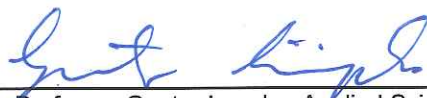
Associate Professor M. Mumtaz Qazilbash, Physics
College of William & Mary



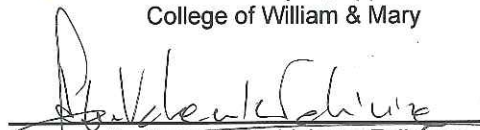
Associate Professor Seth Aubin, Physics
College of William & Mary



Associate Professor Enrico Rossi, Physics
College of William & Mary



Professor Gunter Luepke, Applied Science
College of William & Mary



Dr. Anne-Marie Valente-Feliciano
Jefferson Lab

ABSTRACT

Understanding charge dynamics and the origin of superconductivity in iron-based materials is one of the most important topics in condensed matter physics. Among different structures of iron-based materials, 122-type iron arsenides are of considerable interest due to their diverse phase diagrams, relatively high superconducting transition temperatures, and the availability of high quality single crystals. In this dissertation, we study temperature and frequency dependence of charge dynamics of the electron-doped 122-type iron arsenides in the metallic and superconducting states using broadband infrared spectroscopy at cryogenic temperatures.

We have investigated the charge dynamics and the nature of many-body interactions in metallic La- and Pr- doped CaFe_2As_2 . From the infrared part of the optical conductivity, we discover that the scattering rate of mobile carriers above 200 K exhibits saturation at the Mott-Ioffe-Regel limit of metallic transport. However, the dc resistivity continues to increase with temperature above 200 K due to the loss of Drude spectral weight. The loss of Drude spectral weight with increasing temperature is seen in a wide temperature range in the uncollapsed tetragonal phase, and this spectral weight is recovered at energy scales about one order of magnitude larger than the Fermi energy scale in these semimetals. The phenomena noted above have been observed previously in other correlated metals in which the dominant interactions are electronic in origin. Further evidence of significant electron-electron interactions is obtained from the presence of quadratic temperature and frequency-dependence scattering rate at low temperatures and frequencies in the uncollapsed tetragonal structures of La- and Pr-doped CaFe_2As_2 . We also observe weakening of electronic correlations and a decrease of Drude spectral weight upon the transition to the collapsed tetragonal phase in Pr-doped CaFe_2As_2 .

We have measured infrared reflectance spectra of $\text{BaFe}_{1.9}\text{Pt}_{0.1}\text{As}_2$ in the normal and superconducting states. We find that this superconductor has fully gapped Fermi surfaces. Importantly, we observe strong-coupling electron-boson interaction features in the infrared absorption spectra. By using two modeling methods which include strong-coupling effects via the Eliashberg function, we obtain a good quantitative description of the energy gaps and the temperature dependent strong-coupling features. Our experimental data and analysis provide compelling evidence that superconductivity in $\text{BaFe}_{1.9}\text{Pt}_{0.1}\text{As}_2$ is induced by the coupling of electrons to a low energy bosonic mode.

TABLE OF CONTENTS

	Acknowledgements	iii
	Dedications	iv
Chapter 1.	Introduction	1
	1.1 Conventional superconductivity	2
	1.2 Unconventional high-temperature superconductors	3
	1.3 Scope of the dissertation	5
Chapter 2.	Iron-based superconductors	8
	2.1 Basic structures	8
	2.1.1 Structures and T_c	10
	2.1.2 Crystal structure, electronic band structure and Fermi surface of the 122 iron-based arsenides	12
	2.1.3 Magnetism	15
	2.2 Phase diagrams	19
	2.2.1 Pressure and doping effects in BaFe_2As_2 system	19
	2.2.2 Pressure and doping effects in CaFe_2As_2 system	21
	2.3 Superconductivity	26
	2.3.1 Pairing symmetry	27
	2.3.2 Pairing mechanism	30
	2.3.3 Energy gaps	32
Chapter 3.	Experimental methods	34
	3.1 Fourier transform infrared (FTIR) spectroscopy	34
	3.1.1 Introduction	34
	3.1.2 Experimental equipment and technique	38
	3.1.3 Data analysis	40
	3.2 Spectroscopic ellipsometry	42
	3.2.1 Introduction	42
	3.2.2 Experimental equipment and techniques	46
	3.2.3 Data analysis	49
Chapter 4.	Rare-earth doped CaFe_2As_2	51
	4.1 Introduction	51

4.2	Samples and experiments	54
4.3	Results and discussion	56
4.3.1	Optical conductivity and spectral weight	56
4.3.2	Free carrier response	60
4.3.3	Interband transitions	71
4.4	Summary	71
Chapter 5.	Strong electron-boson interaction in superconducting BaFe _{1.9} Pt _{0.1} As ₂	73
5.1	Introduction	73
5.2	Sample and measurements	79
5.3	Results and discussions	80
5.3.1	Reflectance, optical conductivity and normalized absorption	81
5.3.2	Modeling with Allen's formalism	85
5.3.3	Modeling with Zimmermann's approach	94
5.3.4	Origin of the two modes in the electron- boson spectral density function	98
5.3.5	Temperature dependent normalized absorption and superconducting gaps	101
5.4	Summary	105
Chapter 6.	Conclusion and outlook	107
	Appendices	111
	Appendix A: Reflectance, ellipsometry, and data analysis to obtain <i>ab</i> - plane optical constants of Ca _{0.8} La _{0.2} Fe ₂ As ₂ and Ca _{0.85} Pr _{0.15} Fe ₂ As ₂	111
	Appendix B: Phonon shift across CT phase transition in Ca _{0.85} Pr _{0.15} Fe ₂ As ₂	117
	Appendix C: Representative fits of rare-earth doped CaFe ₂ As ₂	119
	Appendix D: Validation of the EPW 4.2 software	122
	Bibliography	125

ACKNOWLEDGEMENTS

I would like to thank my advisor Prof. Mumtaz Qazilbash, who gave me a lot of useful advice and constructive criticisms, helped me overcome countless difficulties, and keeps pushing me forward. I would also like to express my gratitude to our collaborators Prof. Johnpierre Paglione and Dr. Shanta Saha from the University of Maryland – College Park, who provided us with a number of high quality samples. I would like to thank Dr. Hao Shi who helped me implement EPW software in Linux system. I would like to thank NASA Virginia Space Grant Consortium and National Science Foundation for providing us research funding. I would like to give special thanks to Prof. Gunter Luepke and Prof. Seth Aubin, who have been on my annual review committees since 2013. I would like to thank all the students I worked with in the lab: Tyler, Peng, David, Patrick, Arlo, Danny, Mitchell, Stephanie, and Ryan. I learned a lot from you guys and you kept me company in the lab during nights and weekends.

I would like to thank all my friends in Williamsburg, Mi, Hao, Du, and all of my “poker friends”. You made my life here colorful and I cannot imagine passing time without you.

Finally, I would like to express my gratitude and love to my family. Thank you, my mom, dad and elder sister, who always believed in me, no matter how hard I fell down. I would like to give special thanks to my beautiful wife, who always encourages me and gets me through the most difficult times. You have made the last year of my PhD research a lot easier than it could ever be.

This Ph.D. is dedicated to my parents.

CHAPTER 1

Introduction

Since its discovery in 1911 by H. Kamerlingh Onnes, superconductivity has been one of most important topics and among the most exciting phenomena in condensed matter physics. The two necessary and extraordinary properties of a superconductor are zero electrical resistance and expulsion of magnetic field below a well-defined transition temperature T_c . From a microscopic view, in the superconducting state, electrons form bound pairs through an attractive interaction. The bound electron pairs are called Cooper pairs. In conventional superconductors, the attractive interaction between electrons is mediated by phonons. However, in unconventional high-temperature superconductors, the pairing mechanism can be different, and phonons alone may not provide the “glue” to form Cooper pairs. Instead, the pairing glue may have a magnetic origin. A thorough understanding of

the charge dynamics as well as the pairing mechanism in iron-based materials (one family of unconventional high temperature superconductors) is a significant intellectual contribution. In this chapter, I will briefly introduce conventional superconductivity and unconventional high temperature superconductors, and then provide the scope of this dissertation.

1.1 Conventional superconductivity

For conventional superconductors, phonons are the key virtual excitations that turn the repulsive Coulomb interaction into a weak attraction that binds the electrons in Cooper pairs. The energy gap has s-wave symmetry without nodes. Based on the coupling strength between the electrons and phonons, conventional superconductors can be divided into weak-coupling and strong-coupling superconductors. In 1957, a detailed microscopic picture was established by Bardeen, Cooper and Schrieffer (BCS) [1], which describes weak-coupling traditional superconductors very well. In BCS theory, the electron-phonon interactions are assumed to be small, instantaneous and nonlocal, which is a good approximation for weak-coupling superconductors. However, when the electron-

phonon interaction becomes large, a more realistic model than BCS theory has to be applied.

Strong electron-phonon interactions have been first studied by Migdal [2] in a normal metal and by Eliashberg [3] in superconductors. In their model, the effective interaction between electrons is retarded in time and local in space, in contrast to the BCS model. The strong coupling Eliashberg function $\alpha^2(\omega)F(\omega)$ (the electron-phonon coupling times the phonon density of states) is introduced in the gap equations (Eliashberg equations). The experimental results on strong-coupling superconductors, like lead (Pb), including the phonon density of states from neutron scattering, tunneling experiments, and infrared absorption, provide consistent evidence for the validity of the Eliashberg theory.

1.2 Unconventional high-temperature superconductors

In 1986 and soon thereafter, a family of copper-oxide materials (cuprates) with high transition temperature (T_c) were discovered with T_c reaching as high as 133 K [4]. Since then, a number of different materials, named unconventional superconductors, have been subsequently discovered, whose superconducting

behavior cannot be solely understood within the electron-phonon interaction pairing mechanism. Other possible mechanisms for electron pairing in high- T_c superconductivity, such as spin fluctuations mediated pairing, have been proposed. However, no consensus has been reached yet.

An important discovery of 26 K superconductivity in fluorine-doped LaFeAsO [5] was made in 2008. Shortly after that, the record T_c of 55 K in bulk iron-based superconductors was attained [6]. Compared to cuprates, key differences have been found in the crystal structure of iron-based superconductors [7]: 1) the tetrahedral FeAs-type layer as opposed to the planar copper-oxygen structure of the cuprates; 2) the ability of doping directly into the active pairing layer; and 3) the metallic (rather than insulating) multiband nature of the parent compounds. The detailed properties of iron arsenides will be discussed in Chapter 2. Several crucial questions need to be stressed: what is the pairing mechanism in iron-based superconductors, and is it similar or different compared to other unconventional superconductor families like the cuprates? What can be deduced about interactions from the charge dynamics of iron arsenides in the normal (metallic) state? These questions will be discussed in the body of the dissertation.

1.3 Scope of the dissertation

In this dissertation, I report temperature-dependent infrared and optical spectroscopy data on three distinct electron-doped 122-type iron arsenide compounds: the rare-earth doped $\text{Ca}_{0.8}\text{La}_{0.2}\text{Fe}_2\text{As}_2$ and $\text{Ca}_{0.85}\text{Pr}_{0.15}\text{Fe}_2\text{As}_2$, and platinum doped $\text{BaFe}_{1.9}\text{Pt}_{0.1}\text{As}_2$. Out of these three materials, only the last one exhibits bulk superconductivity. By carefully analyzing the data, we study the electron-electron and electron-boson interactions in the metallic and superconducting states of the materials.

In Chapter 2, I first introduce the basic properties of iron-based superconductors, especially the 122-type iron arsenides. I give a brief discussion of the possible key factors (As-Fe-As bonds and the anion height from Fe layers) that affect T_c ; the primitive unit cell, electronic band structure and Fermi surface of 122-type iron arsenides; and the magnetism of iron arsenides. Due to the unique collapsed tetragonal phase of CaFe_2As_2 system, I discuss the phase diagrams of BaFe_2As_2 and CaFe_2As_2 separately. By applying pressure and/or doping chemical elements, the structural and magnetic phase transition of the parent compounds, BaFe_2As_2 and CaFe_2As_2 , can be suppressed and superconductivity may occur. In the last section of this chapter, I introduce the superconducting pairing symmetry, possible pairing mechanisms and multi-band nature of the iron arsenides.

Infrared spectroscopy is one of the most important techniques for studying metallic and superconducting properties. I introduce two experimental spectroscopic techniques in Chapter 3, Fourier transform infrared (FTIR) spectroscopy and spectroscopic ellipsometry, which are the main experimental probes used in this dissertation. I discuss the principles of the techniques, the detailed experimental set-up including cryogenic instrumentation, measurement strategies, and data analysis procedures.

In Chapter 4, we report infrared and optical spectroscopy data on two rare-earth doped CaFe_2As_2 materials, $\text{Ca}_{0.8}\text{La}_{0.2}\text{Fe}_2\text{As}_2$ and $\text{Ca}_{0.85}\text{Pr}_{0.15}\text{Fe}_2\text{As}_2$ single crystals. These materials are not bulk superconductors even though the antiferromagnetic phase has been totally suppressed by the rare-earth (La and Pr) dopants. We focus on the temperature-dependent charge dynamics in the metallic phases (uncollapsed and collapsed tetragonal phases). We find that although the resistivity continues to increase above 200 K, the scattering rate saturates above 200 K. The scattering rate in uncollapsed tetragonal phase is dominated by a quadratic temperature dependent and frequency dependent term ascribed to significant electron-electron interactions. We also observe that the scattering rate of free carriers, optical interband transitions, and infrared-active phonons are affected across the collapsed tetragonal phase transition.

In Chapter 5, studies on superconducting $\text{BaFe}_{1.9}\text{Pt}_{0.1}\text{As}_2$ using infrared spectroscopy are reported. We observe strong-coupling electron-boson interaction features in the infrared absorption spectra directly. The infrared data is consistent with multi-band superconductivity with isotropic gaps. By employing two theoretical models based on the Eliashberg theory to quantitatively explain our absorption spectra, we identify a bosonic mode centered at 5.1 ± 0.6 meV (41 ± 5 cm^{-1}) that provides the pairing glue in superconducting $\text{BaFe}_{1.9}\text{Pt}_{0.1}\text{As}_2$. The bosonic mode cannot be due to phonons due to its low frequency, and it is likely to originate from spin fluctuations.

Finally, in Chapter 6, I record the conclusions and discuss possible future work.

CHAPTER 2

Iron-based superconductors

2.1 Basic structures

Since the discovery of $\text{LaFeAsO}_{1-x}\text{F}_x$ [5], so-called ‘1111’ structure, with a superconducting transition temperature (T_c) of 26 K in 2008, a series of different iron-based structures exhibiting superconductivity have been discovered in the past decade. Fig. 2.1, taken from Ref. [8], shows some representative iron-based superconducting structures. Each has a distinct layered arrangement with active Fe_2As_2 -type layers, as shown in the gray areas in Fig. 2.1. The key ingredient is a quasi-two-dimensional layer consisting of a square lattice of four iron atoms with tetrahedral coordinated bonds to the atoms above and below the iron lattice. The atoms could either be pnictogen (phosphorus, arsenic) or chalcogen (selenium or

tellurium) anions. This unique structure can be either simply stacked together or separated by spacer layers formed by alkali metals (such as Na), alkaline-earth metals (such as Ba) or more complicated combinations. It is worth noting that two recently discovered structures, ‘112’ and ‘1144’, also share similar stacking arrangement and have a bulk T_c of 47 K [9] and 36 K [10]. It will not be too surprising if new structures of iron-based superconductors are discovered in the future and thereby further enrich the family of these high-temperature superconductors.

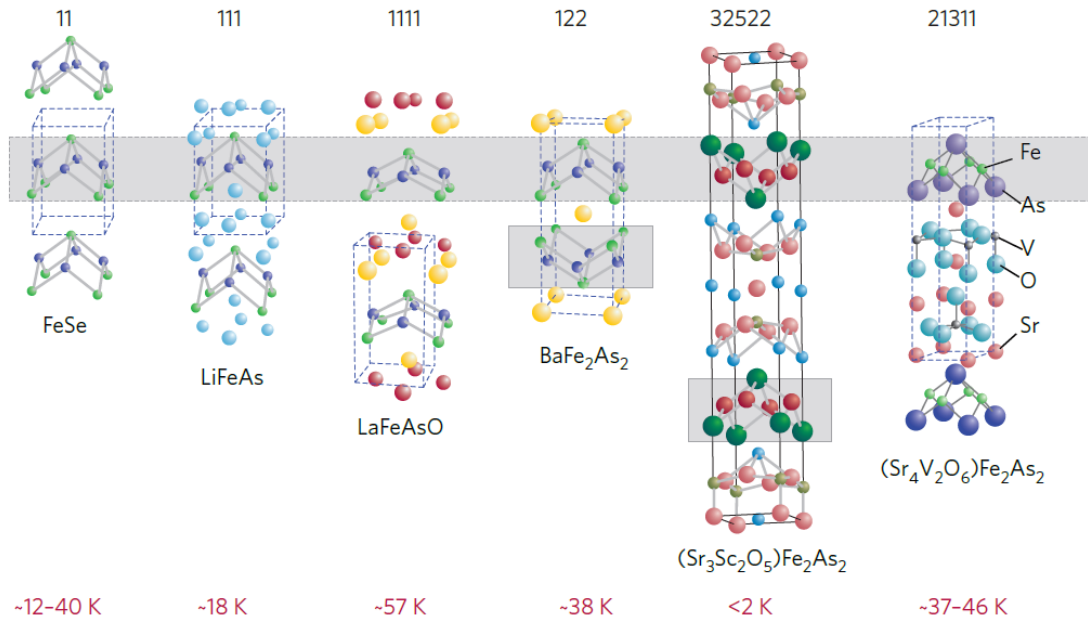


FIG. 2.1. Structures of several types of iron-based superconductors [8]. The temperature below each type is the highest T_c achieved in the structure.

2.1.1 Structures and T_c

To study the connection between transition temperatures and the structural properties, researchers first noticed that T_c is dependent on the angle between As-Fe-As bonds (where two arsenic atoms are located within the same plane), as shown in Fig. 2.2. T_c reaches the highest value at the As-Fe-As bond angle of 109.47° [11], corresponding to an undistorted pnictogen tetrahedron with the iron

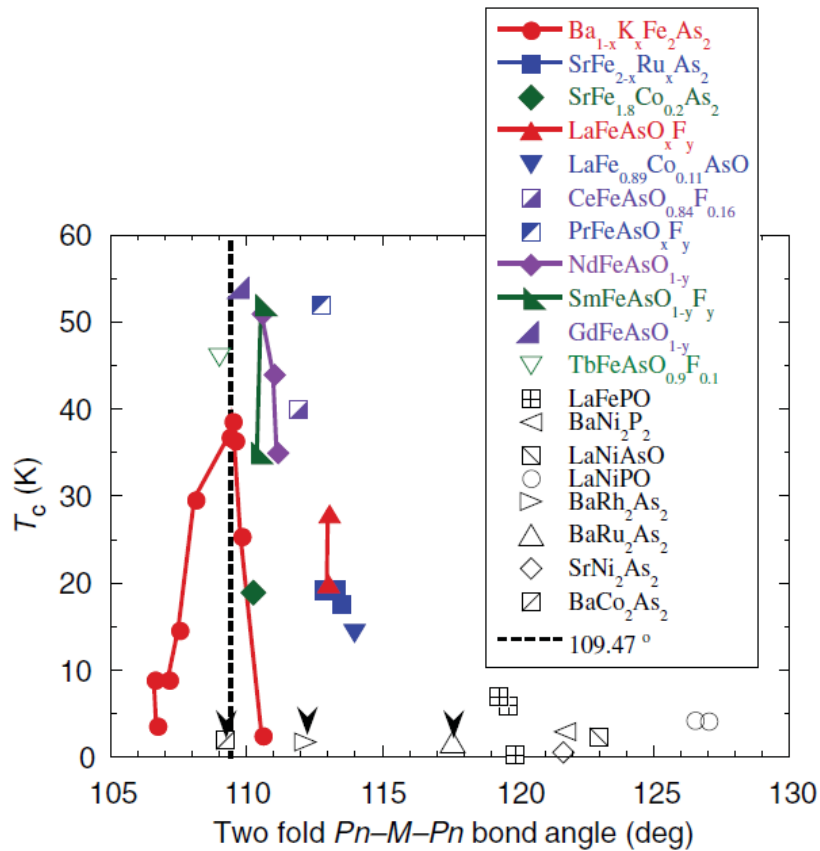


Fig. 2.2. From Ref. [11]. T_c versus $Pn-M-Pn$ type bonding angle at the room temperature among different species of iron-based superconductors, where Pn is P or As, and M is transition metal, such as Fe. T_c is maximum at an angle close to 109.47° .

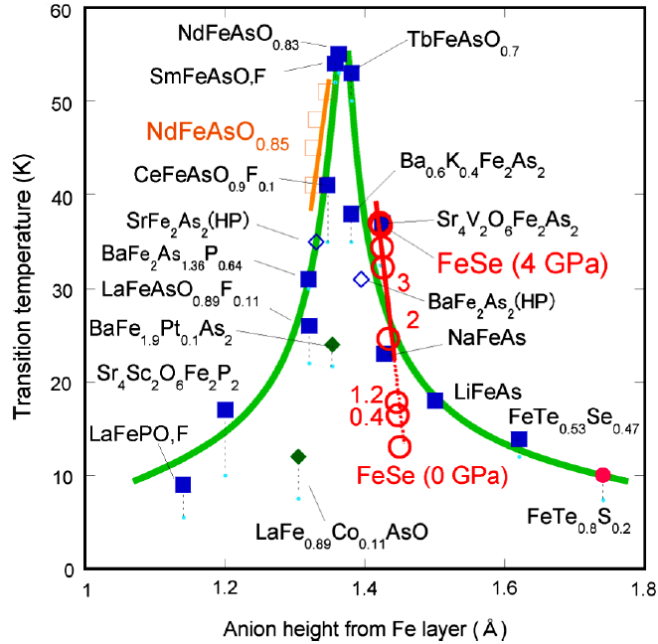


Fig. 2.3. From Ref. [12]. Anion height dependence of T_c for the several typical Fe-based superconductors. Large symbols indicate the onset transition temperature while small light-blue circles represent the zero-resistivity temperatures at ambient pressure.

(Fe) ion in the center. This suggests that the potential for high T_c is greatest for undistorted FeAs_4 tetrahedra (although no universal successful explanation has been developed yet). Although K-doped BaFe_2As_2 shows clear trend, there are some materials that do not follow this trend, like BaCo_2As_2 and LaFePO .

Another correlation between the structure parameter and T_c is the anion height from Fe layers. The dependence of maximum T_c in a given system and anion height are summarized in Fig. 2.3 [12]. The figure shows a symmetric curve with a peak around 1.38 \AA . Both data at ambient pressure and under high pressure obeys this unique curve. However, there are also some unusual cases, like $\text{BaFe}_{1.9}\text{Pt}_{0.1}\text{As}_2$ and $\text{LaFe}_{0.89}\text{Co}_{0.11}\text{AsO}$, that have to be considered separately.

2.1.2 Crystal structure, electronic band structure and Fermi surface of the 122 iron-based arsenides

In this section, we will focus on the iron-based arsenides with the “122” structure. The 122 iron based arsenides are the main topic of this dissertation. For a typical 122 ThCr_2Si_2 -type structure, Fig. 2.4 (a) shows a body-centered tetragonal unit cell with the lattice space group $I4/mmm$. This unit cell is not a primitive unit cell, and it contains two formula units. Due to the simplicity and convenience of this unit cell, it is widely used in experimental studies. The lattice parameters of the parent compound of the 122 structure iron-based arsenides are $a = b \approx 4 \text{ \AA}$ and $c \approx 13 \text{ \AA}$. One primitive unit cell is shown in Fig. 2.4 (b), with lattice height equal to half of the “ c ” parameter of the tetragonal unit cell.

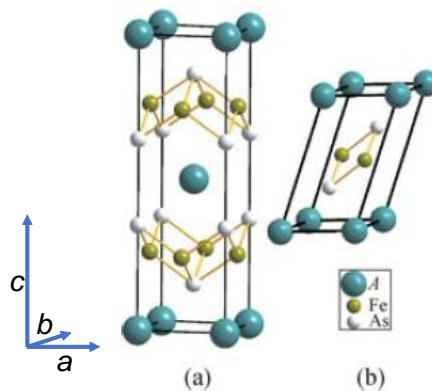


Fig. 2.4. (a) Tetragonal unit cell of 122 type iron-based material [13]. (b) A primitive unit cell containing one formula unit.

The first-principles density functional theory calculated band structure is shown in Fig. 2.5 (a) [13]. There are five Fe-3d bands which are close to each other and at least four cross the Fermi level. This indicates the multi-band nature of iron-based materials. At the Γ and Z points, there are two bands (another one is slightly below the Fermi level) crossing the Fermi level and form hole-like Fermi surface sheets. At the X point, there are also two bands crossing the Fermi level and form electron-like Fermi surface sheets. The corresponding 3D Fermi surfaces are plotted in Fig. 2.5 (b). Both hole and electron Fermi surfaces are formed by d_{xz} , d_{yz} and d_{xy} orbitals [14]. Again, two semi-cylindrical hole Fermi surface pockets are centered at Brillouin zone center (Γ) point and at the Z point), and another two even more cylindrical electron pockets are centered at the X point (zone corner). We can see that a magnetic ordering vector $Q = (\pi, \pi)$ that spans from the center of the Brillouin zone at Γ point to the corner at X point will easily nest a circle of points on each of two different Fermi sheets (for example, purple and yellow sheets), which could possible result in a long-range spin-density wave order that is driven by properties of the band structure. There are other possible origins of the spin-density wave order phase, like antiferromagnetic exchange between localized electrons and Hund's coupling due to multiple orbitals, and this will be discussed in more details in the next section.

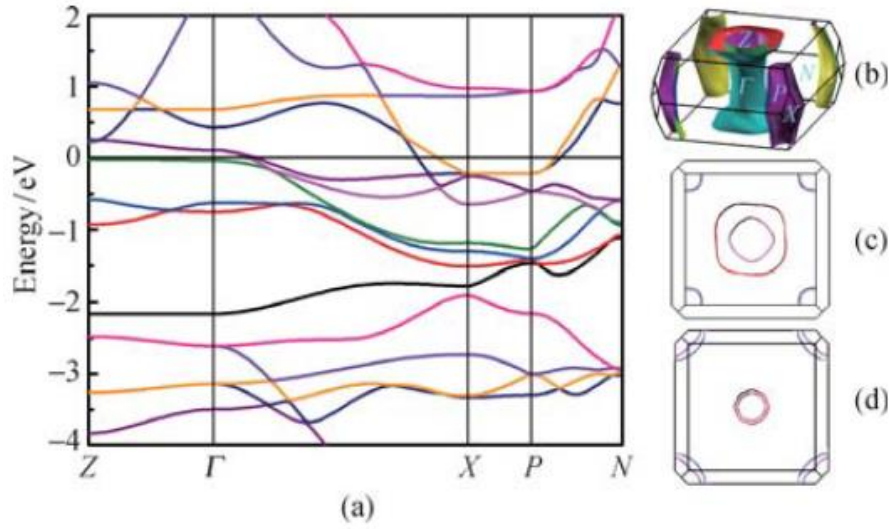


Fig. 2.5. (a) First-principles density functional theory calculated band structure of BaFe_2As_2 [13]. Lines of different colors indicates different bands. (b) The Fermi surfaces and their sectional views through symmetrical k-points (c) Z and (d) Γ parallel to (001) plane.

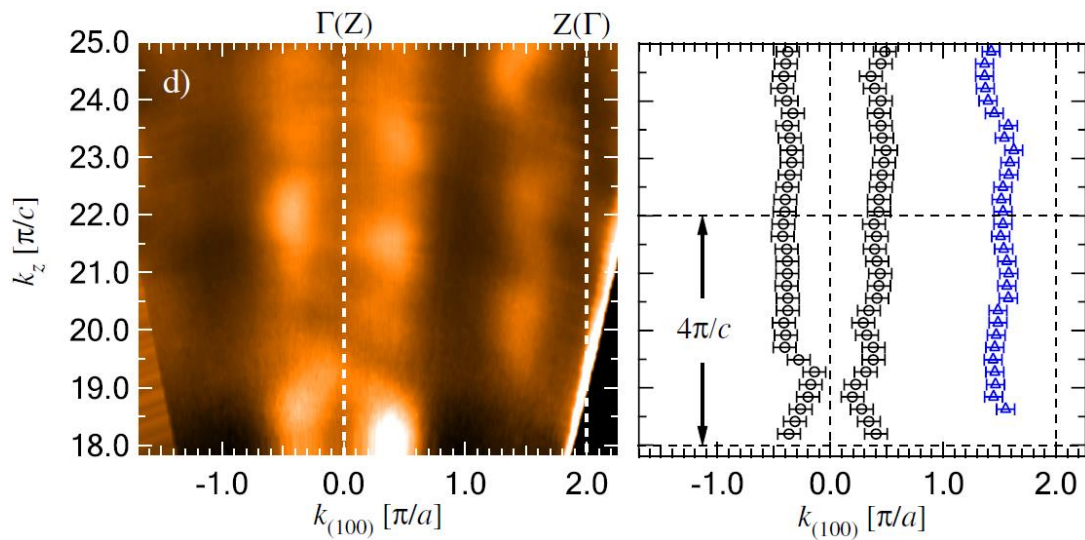


Fig. 2.6. ARPES k_z dispersion data of tetragonal CaFe_2As_2 at $T = 200$ K [15]. The plot is k_z dispersion data parallel to Γ -M. The right panel is the Fermi crossing momenta extracted from the left panel.

Experimental results like angle-resolved photoemission spectroscopy (ARPES) match the theoretical predictions well [15–18]. Fig. 2.6 [15] shows the ARPES result of parent compound tetragonal CaFe_2As_2 . Both the electron and hole pockets are quasi-2D cylindrical with little k_z dependence. The effect of hole or electron doping on the electronic structure is fairly well captured by a rigid-band picture: the basic Fermi surface topology is kept with both electron [19,20] ($\text{BaFe}_{2-x}\text{Co}_x\text{As}_2$) and hole [21] ($\text{Ba}_{1-x}\text{K}_x\text{Fe}_2\text{As}_2$) doping, with the size of Fermi pockets changing accordingly and with reasonable continuity observed when crossing between each case.

2.1.3 Magnetism

At room temperature, the parent compounds of 122 iron-based materials like BaFe_2As_2 and CaFe_2As_2 are in the tetragonal paramagnetic phase. The resistivity is 0.3 - 0.4 $\text{m}\Omega \text{ cm}$ [22,23], which is much higher than conventional metals, so they are relatively poor conductors.

Upon decreasing temperature, the tetragonal paramagnetic metal will undergo a structural (T_S) and magnetic (T_N) phase transition at low temperature. Unlike 1111-type iron-based materials, in which T_S and T_N are usually not the same

temperatures, in 122-type materials, the structural and magnetic phase transition are coupled and occur at the same temperature. The phase transition temperature T_N (T_S) is approximately 173 K for CaFe_2As_2 [24], 140 K for BaFe_2As_2 [25] and 198K for SrFe_2As_2 [26]. Across the phase transition, the lattice structure becomes orthorhombic phase $Fmmm$ face-centered from high temperature body-centered space group $I4/mmm$. The unit cell rotates 45° with respect to the tetragonal basal plane axes and the lattice constant a is slightly larger than b . The transition is first ordered, and appears discontinuous and often hysteretic [24]. At the same temperature, the parent compounds transition from a paramagnetic to an antiferromagnetic phase forming a stripe-type spin-density-wave phase. The magnetic unit cell is the same as the orthorhombic chemical unit cell. Fe moments are oriented along the orthorhombic a axis, arranged antiferromagnetically along a and ferromagnetically along b . Neighboring layers are stacked antiparallel to one another along the c -axis, as shown in Fig. 2.7. Neutron diffraction experiments on the 122 materials find fairly consistent magnetic moments for different members of the 122 family (CaFe_2As_2 , BaFe_2As_2 and SrFe_2As_2) with $0.8 - 1 \mu_B$ [27], comparing to $2.2 \mu_B$ of metallic iron.

There are three broad classes of explanation for antiferromagnetism:

a. In the 'local moment' picture, appropriate for the insulating copper oxides, AFM

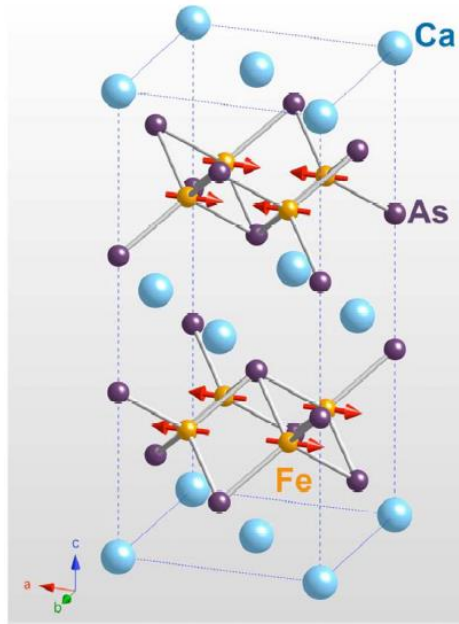


Fig. 2.7. From Ref. [24]. Illustration of the antiferromagnetic structure of CaFe_2As_2 below the magnetic transition temperature. The Fe magnetic moments are aligned antiferromagnetically along the a and c axes and ferromagnetically along the shorter b axis.

interactions are well described by a Heisenberg-like Hamiltonian, which indicates nearest-neighbor interactions and significant next-nearest-neighbor interactions. For the 122 materials, the Hamiltonian is usually written in the form [27,28]: $H = \sum_{\langle jk \rangle} J_{jk} S_j \cdot S_k$, where J_{jk} are exchange constants. The magnetic excitations can be described using two in-plane exchange constants; the near-neighbor interactions J_1 and the next-near-neighbor interaction J_2 . Once $J_2 > J_1/2$ condition is satisfied, stripe AFM order can be constructed [27,28]. And this condition is always satisfied for 122 iron arsenides [27–29].

b. Whereas in the 'itinerant model', suitable for metallic chromium, AFM order arises from quasiparticle excitations of a nested Fermi surface [30,31]. The nesting is intra-orbital, between the inner hole-like sheet at the Γ point and the inner electron-like sheet at the X point that is commensurate with the structure spanned with a wavevector $Q = (\pi, \pi)$, as shown in Fig. 2.5.

As the nature of the magnetic interactions (i.e. local versus itinerant) is still a topic of considerable debate, there is also possibility that magnetism in the parent compounds of iron arsenide superconductors is neither purely local nor purely itinerant, rather it is a complicated mix of the two [32].

c. Due to the multiorbital nature of iron-based materials, it is becoming clear that Hund's coupling plays a key role on the correlations of these materials and may explain the magnetism in the iron-based materials. A different strength of the Hund's rule coupling at different energy scales has been observed. At high energy, Hund's rule coupling is very strong, whereas it fades away at low energy but gives an imprint on the massive and anisotropic low-energy quasiparticles [33]. Ref. [34] and the references therein also conclude that in the strong Hund's coupling metal the local moment fluctuates very fast and the time-average moment is reduced. The screened moment is the one which can be magnetically ordered at low temperatures.

2.2 Phase diagrams

The 122 iron-based arsenides have rich phase diagrams. The parent compounds are not superconductors, but are in the paramagnetic metallic phase at high temperature and undergo a structural and magnetic phase transition at low temperatures. By applying pressure and/or doping chemical elements (electron doping, hole doping and isovalent doping), the structural and magnetic phase transition can be suppressed and the superconductivity may occur. CaFe_2As_2 system also exhibits a unique phase, called the collapsed tetragonal phase (CT phase), in which the c lattice constant shrinks 10%. In this section, we will focus on the diverse phase diagrams of 122 iron-based materials. Since the phase diagrams of BaFe_2As_2 and CaFe_2As_2 systems have some differences, we will discuss them separately.

2.2.1 Pressure and doping effects in BaFe_2As_2 system

The antiferromagnetic order (or spin-density-wave phase) can be suppressed when applying pressure or doping. The phase diagrams are shown in Fig. 2.7 from Ref. [7]. When the applied pressure is large enough, the superconducting phase emerges. However, continually increase the pressure will

suppress the superconducting phase eventually. The phase diagram is similar for chemical doping of appropriate elements. Doping can be either electron doping (like Co, Ni), hole doping (like K, Na), or iso-valent doping (like P). The superconducting transition temperature reaches the highest value at similar doping level for these cases. The highest transition temperature is 38 K with substitution of 40 % of K for Ba, which is also the highest bulk T_c among all the 122 structures. Increasing doping percentage will usually suppress superconductivity, except hole-doping with K, which can be substituted completely, and become superconducting KFe_2As_2 (T_c is 4 K) at ambient pressure [35]. It is obvious that the two phase diagrams (under pressure and chemical doping) are quite similar, which implies the similarity between structural distortions under pressure and chemical doping. In fact, the electronic structure is quite similar in both cases [30].

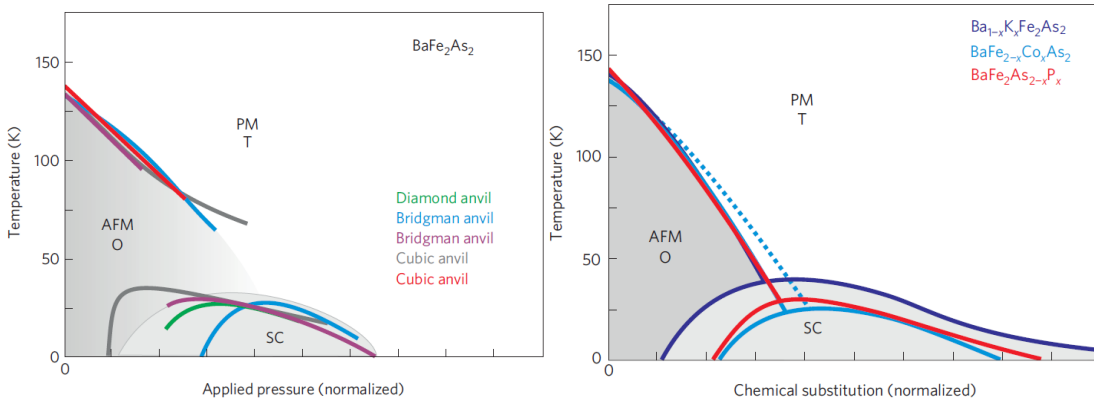


Fig. 2.7. Experimental phase diagrams of the $BaFe_2As_2$ system [7].

2.2.2 Pressure and doping effects in CaFe_2As_2 system

In contrast to the phase diagram of BaFe_2As_2 , the CaFe_2As_2 has an even richer phase diagram, as shown in Fig. 2.8. In CaFe_2As_2 , the antiferromagnetic spin-density-wave phase can be suppressed totally by applying pressure and pressure-induced superconductivity emerges only under non-hydrostatic experimental conditions [36,37]. The unique collapsed tetragonal (CT) non-magnetic phase appears when applying hydrostatic pressure up to 0.35 GPa at low temperature. The unit cell collapses in a way that both the unit-cell volume and the c lattice constant have dramatic decreases of 5 % and 10 %, respectively, and the ab lattice constants undergo an expansion of 2.5 % [38]. In the CT phase, Fe local moments are quenched [38], spin fluctuations are suppressed [39], and electron correlations are reduced [40]. There is also a reconstruction of the Fermi surface in the CT phase, including the complete disappearance of the hole pocket at the zone center [41]. Later on, researchers found that in the BaFe_2As_2 system, the CT phase may occur at much higher pressure compared to CaFe_2As_2 [42].

Doping holes (Na) in Ca site and electrons (Co) in Fe site in CaFe_2As_2 lead to very similar outcomes compared with BaFe_2As_2 system [43,44], as shown in Fig. 2.9. The highest superconducting transition temperature is in the range 20 – 30 K. Note that isovalent P doping at an As site is different compared to the BaFe_2As_2

system. As seen in Fig. 2.10, superconductivity only appears in a small limited range at $x < 0.05$, with T_c at 15 K. Further increase of P doping will suppress superconductivity and induce CT phase [45]. Also, in the CT phase, the system is more like a Fermi liquid, with resistivity proportional to T^2 [45].

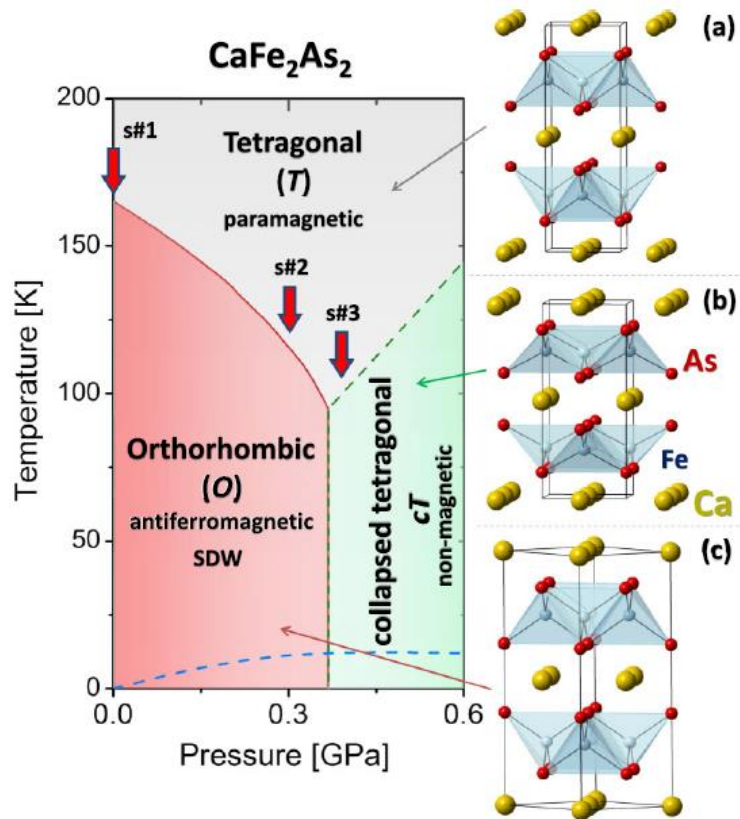


Fig. 2.8. Phase diagram of CaFe_2As_2 parent compound, from Ref. [41]. The blue dashed curve indicates the superconducting phase under a non-hydrostatic pressure condition [36,37].

Aliovalent rare-earth substitution into the alkaline-earth site of CaFe_2As_2 single crystals can be used to fine tune structural, magnetic, and electronic proper-

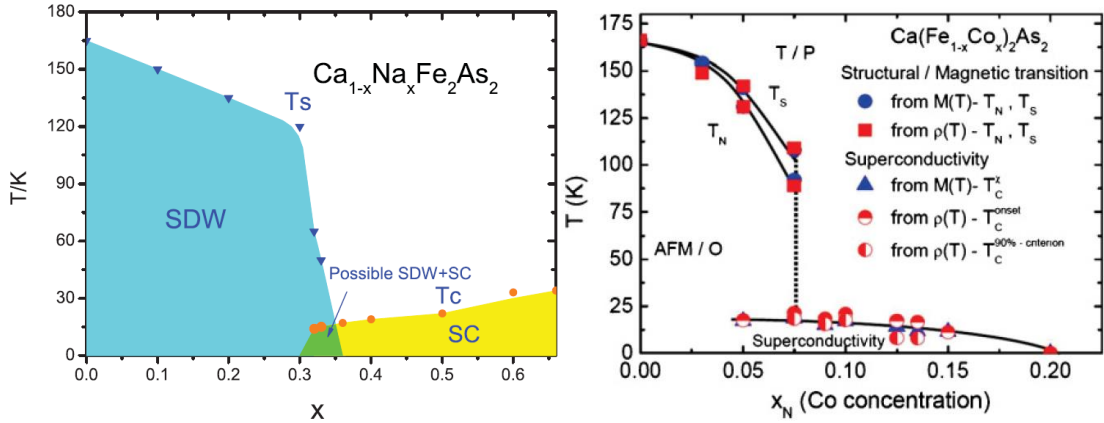


Fig. 2.9. Phase diagram of $\text{Ca}_{1-x}\text{Na}_x\text{Fe}_2\text{As}_2$ (left) [43], and $\text{Ca}(\text{Fe}_{1-x}\text{Co}_x)_2\text{As}_2$ (right) [44].

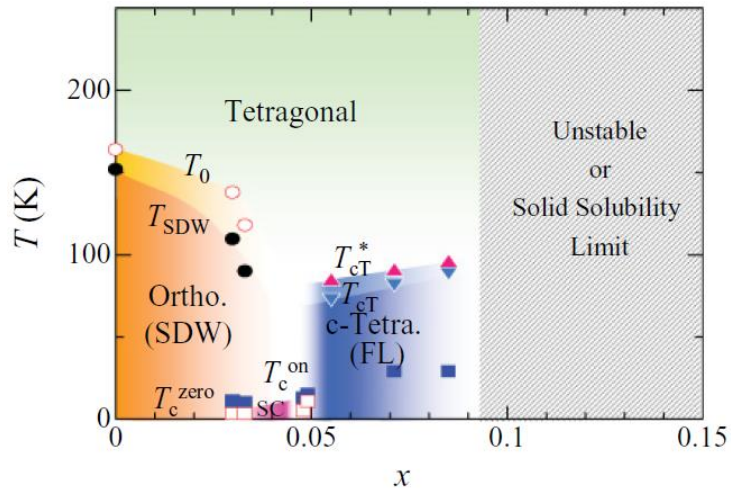


Fig. 2.10. Phase diagram of $\text{CaFe}_2(\text{As}_{1-x}\text{P}_x)_2$ [45].

ties of this iron-based superconducting system. Substitution of trivalent R^{3+} (R represents La, Ce, Pr and Nd) ions for divalent Ca^{2+} tunes the electronic structure by doping extra electrons, which could suppress the antiferromagnetic phase and induce superconductivity. Fig. 2.11 is the phase diagram of $\text{Ca}_{1-x}\text{R}_x\text{Fe}_2\text{As}_2$ (where R^{3+} is the rare-earth substitution) [46]. Surprisingly, the superconducting transition

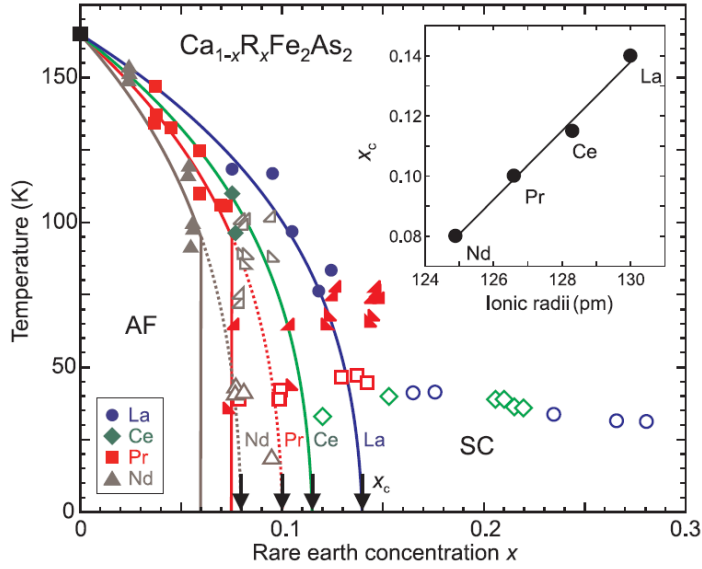


Fig. 2.11. Phase diagram of rare-earth (La, Ce, Pr and Nd) doped CaFe_2As_2 [46]. The symbols' meanings are as following: antiferromagnetic (AF) transitions (solid symbols), structural collapse transitions (half triangles), and small volume fraction superconducting transitions (no bulk superconductivity) (open symbols), CT phase transition on warming (right-pointing half triangles) and cooling (left-pointing half triangles) for Nd (open symbol) and Pr (closed symbol). Inset: scaling of the resultant critical concentration x_c with ionic radii of each rare-earth species.

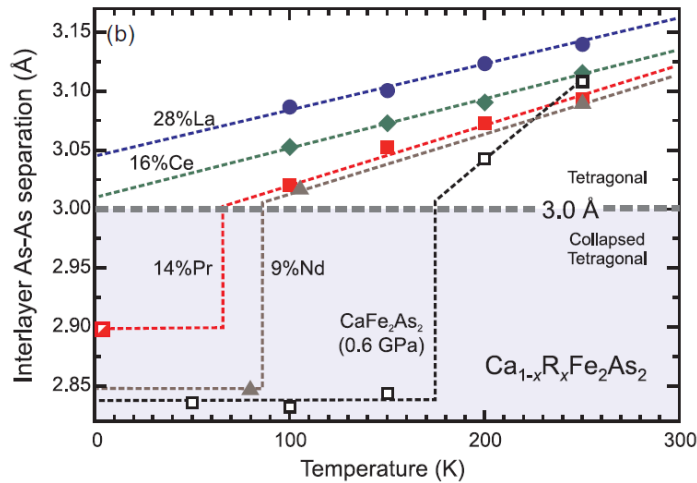


Fig. 2.12. From Ref. [46]. The relationship between CT phase and interlayer As-As anion separation.

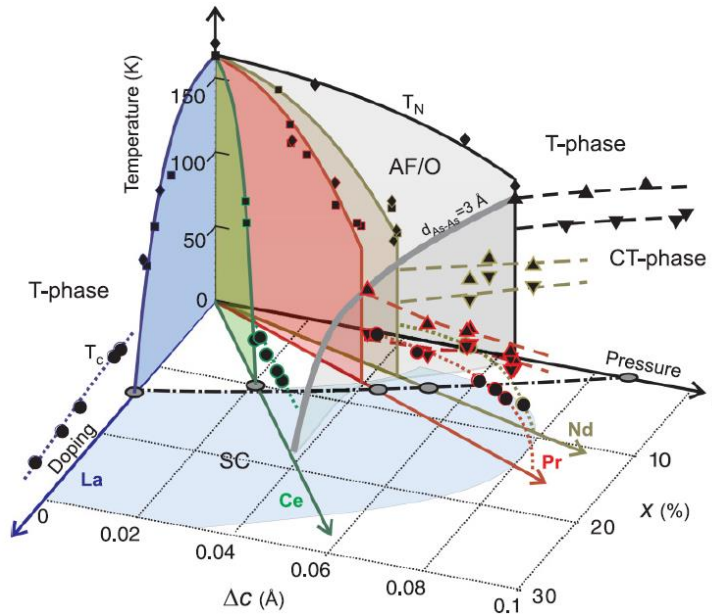


Fig. 2.13. Phase diagram of the $\text{Ca}_{1-x}\text{R}_x\text{Fe}_2\text{As}_2$ series showing the relationship of antiferromagnetic phase (AF), small volume fraction superconducting phase (SC), and collapsed tetragonal phase (CT) with electron doping (x) and effective chemical pressure (Δc) [46].

temperature is very high (as high as 47 K), and actually it is among the highest T_c in all the 122 system. However, the superconducting phase shown in the Fig. 2.11 is not the bulk phase, but only occurs in a small volume fractions (less than 10 %) [46]. The superconductivity has been shown to be intrinsic [47] and not due to impurity phase. Another interesting fact is that the CT phase occurs in the rare-earth doped 122 system at ambient pressure in some of the rare-earth doping (Pr and Nd), but not the others (La and Ce). The key factor is the interlayer As-As anion separation. Both high pressure (0.6 GPa) CaFe_2As_2 and Pr- or Nd-doped CaFe_2As_2 crystals collapse once the interlayer As-As distance reaches a critical

value of $\sim 3.0 \text{ \AA}$. In fact, the strong c -axis collapse is driven by an increasing overlap of interlayer As orbitals [46,48]. Fig. 2.13 [46] shows a universal phase diagram for $\text{Ca}_{1-x}\text{R}_x\text{Fe}_2\text{As}_2$, which extends the charge doping-temperature phase diagram along a third effective chemical pressure axis. Note that the paramagnetic phases that arise upon substitution of the rare-earth dopants do not exhibit bulk superconductivity.

2.3 Superconductivity

Understanding the nature of superconductivity in iron-based superconductors is one of the most important topics in condensed matter physics. It is thought that iron-based superconductors may not be conventional superconductors, such that the electron-phonon pairing mechanism may not be applicable in this family of materials. Hence, alternative microscopic mechanisms for iron-based superconductors have been proposed such as magnetically mediated Cooper-pairs, even though a final consensus still has not been achieved so far. In this section, we will discuss the pairing symmetry, promising pairing mechanism candidates and multi-gap superconductivity of iron-based superconductors.

2.3.1 Pairing symmetry

Understanding the pairing symmetry may help us to understand the pairing mechanism in iron-based superconductors. Although the exact nature of pairing is still under debate, there have been many theoretical and experimental approaches to unveil the pairing symmetry. The gap symmetry was in fact predicted theoretically to have s-wave symmetry, but with a sign change that occurs between different bands in the complex multiband electronic structure. This is the so-called s_{\pm} state, calculated before experiments [49]. Later on, the sign unchanged s_{++} symmetry has been proposed as another promising candidate [50].

On the experimental side, first of all, NMR experiments from Knight shift measurements of Co-doped BaFe_2As_2 [51] shows that ^{75}As Knight shift decreases below T_c both along the crystal c -axis and the ab -plane. This finding is consistent with the singlet pairing of superconducting Cooper pairs (implying an even gap symmetry (that is, s-wave, d-wave and so on)), but in conflict with the p-wave triplet pairing symmetry.

Determining the nature of the orbital order parameter symmetry, however, is much more complex. This is because the s_{\pm} and s_{++} share the same symmetry, and due to the nested multi-orbital nature, both s_{\pm} and d-wave are nearly degenerate [52] making it difficult to distinguish the two different symmetries in

phase-sensitive experiments. To distinguish the above three pairing states: s_{\pm} , s_{++} and d-wave, several experiments on selected samples have been carried out, for example: Scanning tunneling microscopy first on Fe(Se,Te) single crystals [53] and then on Co-doped BaFe_2As_2 122 materials [54] observes that the sign is reversed between the hole and the electron Fermi-surface pockets (s_{\pm} -wave). ARPES measurements on optimal K-doped BaFe_2As_2 clearly shows nearly isotropic energy gaps and no sign of nodes [55], as shown in Fig. 2.14, which provides strong evidence for an s-wave symmetry. The observation of a collective magnetic-resonance mode in various materials [56,57] that appears below the SC transition temperature supports the sign change on different (or different part of) Fermi sheets. Scanning superconducting quantum interference device (SQUID) measurement on 1111 structure material found no evidence of half-integer flux quantum [58], and another experiment found substantial c -axis Josephson tunneling between Pb and $\text{Ba}_{1-x}\text{K}_x\text{Fe}_2\text{As}_2$ [59], which suggests nonzero angular-momentum pairing, such as d-wave, unlikely. Another experiment observed electromagnetic pulse-induced half-flux quantum jumps in a loop formed by Nb and polycrystalline 1111 structure superconducting sample [60]. This suggests that there are “ π junctions” along the current path resulting from Cooper pairs tunneling between opposite-sign superconducting regions. And it could not occur

in d-wave symmetry since there would be many more jumps expected for a d-wave symmetry [7,61]. All of these experiments are consistent with the proposed s_{\pm} -wave pairing.

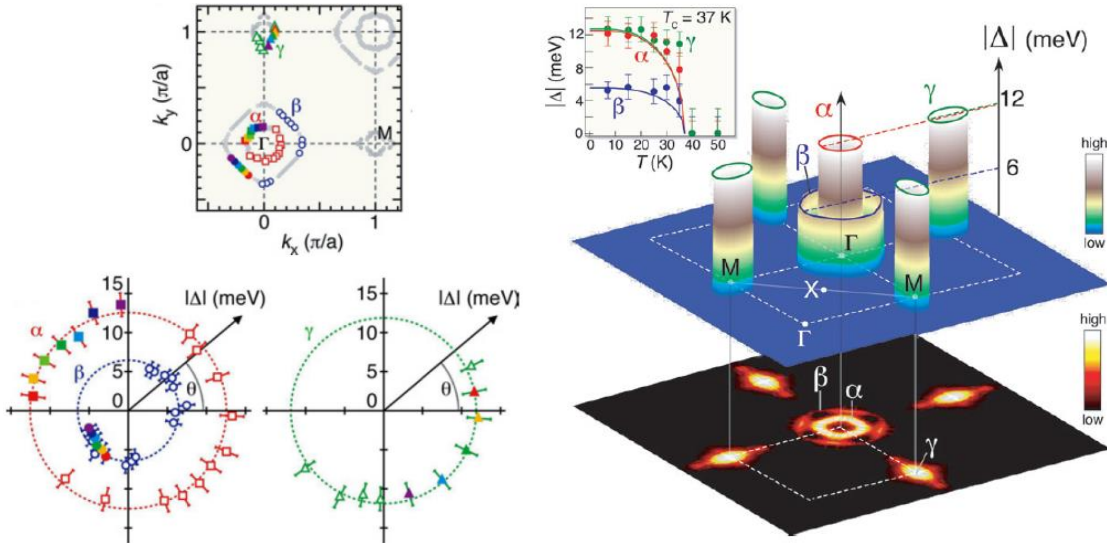


Fig. 2.14. From Ref. [55]. ARPES measurements of superconducting $\text{Ba}_{0.6}\text{K}_{0.4}\text{Fe}_2\text{As}_2$.

Left: superconducting-gap values at 15K shown on polar plot for the three Fermi surfaces as a function the of the Fermi surface angle θ (zero degree is along Γ -M). Right: three-dimensional plot of the superconducting-gap size (Δ) measured at 15 K on the three observed Fermi sheets (shown at the bottom as an intensity plot) and their temperature evolutions (inset).

Even though the s_{\pm} symmetry seems more reasonable, we cannot conclude all the iron-based superconductors share the same pairing symmetry. In fact, there is compelling evidence that superconductor KFe_2As_2 has d-wave symmetry [62,63], and from theoretical predictions, some researchers believe that LiFeAs is possibly a spin-triplet p-wave superconductor [64].

2.3.2 Pairing mechanism

Understanding the formation of Cooper pairs in iron-based superconductors is a hotly debated topic. For conventional superconductors (BCS superconductors), phonons are the key virtual excitations that turn the repulsive Coulomb interaction into a weak attraction to form Cooper pairs. The Cooper pairs then condense in the superconducting state. However, this phonon-mediated mechanism alone has been ruled out at the beginning, since electron-phonon coupling of 1111 [65] and 122 [66] structure $\lambda = 0.2 - 0.3$ cannot explain the transition temperature T_c as high as 55 K and 38 K for the 1111 structure and the 122 structure, respectively. Also the phase competition between long-range antiferromagnetism and superconductivity suggests that magnetic fluctuations play a role in the Cooper pairing in the iron-based superconductors. The promising candidates for mediating Cooper pairing are spin and orbital fluctuations.

Following Ref. [67,68], we summarize the spin and orbital (charge) fluctuation pairing in a general case (considering a single band for simplicity). The gap equation for superconductivity can be written in the form (analogous to BCS gap equation):

$$\Delta(\mathbf{k}) = - \sum_{\mathbf{k}'} V(\mathbf{k} - \mathbf{k}') \frac{\tanh[E(\mathbf{k}')/2k_B T]}{2E(\mathbf{k}')} \Delta(\mathbf{k}') \quad (2.1)$$

where $E(\mathbf{k})$ is the quasiparticle excitation spectrum and $V(\mathbf{q} = \mathbf{k}' - \mathbf{k})$ is the pairing interaction. When the pairing is mediated by phonons, $V(\mathbf{q})$ is negative (attractive) and this requires a constant sign of the gap $\Delta(\mathbf{k})$. When the pairing is mediated by spin or orbital (charge) fluctuations, on the other hand, the pairing interaction can in general take the form,

$$V(\mathbf{q}) = \frac{3}{2}V_{sp}(\mathbf{q}) - \frac{1}{2}V_{ch}(\mathbf{q}) + (\text{first order terms}) \quad (2.2)$$

where V_{sp} and V_{ch} (both positive) are contributions from spin and orbital (or charge) fluctuations, respectively. When $V_{sp} \gg V_{ch}$, which means spin fluctuation strongly dominate over (orbital) charge fluctuations, $V(\mathbf{q})$ is positive, then the gap on the Fermi surface has to change its sign across the wave vector \mathbf{Q} , which means either d-wave or s_{\pm} symmetry. So, in the singlet channel, spin fluctuations exchange always leads to a repulsive interaction, and therefore can only realize sign-changing superconducting states [49,69]. If this interaction is sufficiently strong at some particular momentum it will necessarily result in superconductivity. In the case of a single Fermi surface this superconductivity will necessarily be nodal, usually of a d-wave symmetry, like high- T_c cuprates [61,70,71]. On the other hand, in a multiband system there may be a possibility to avoid nodes, while still preserving a sign-changing structure [67].

Another approach as described in Ref. [50] using a five-orbital Hubbard-Holstein model, moderate electron-phonon interaction, which is found in iron pnictides due to the relatively small Fe-ion oscillation (electron-phonon interaction), can induce the critical d-orbital fluctuations, without being prohibited by the Coulomb interaction. And the orbital fluctuations are enhanced by Coulomb interaction. These fluctuations give rise to the strong pairing interaction for the s-wave superconducting state without sign reversal (s_{++} wave state), which is consistent with experimentally observed robustness of superconductivity against impurities [72].

2.3.3 Energy gaps

Since multiple $3d$ bands cross the Fermi level and form multiple Fermi sheets in iron-based materials, one could expect more than one superconducting gap in the superconducting state. And indeed, there are many electron- and hole-doped 122 iron-based superconductors in which multiple superconducting gaps have been observed in experiments, for example, infrared spectroscopy [73–75], ARPES [55,76], point-contact Andreev-reflection spectroscopy [77,78] and scanning tunneling spectroscopy [79,80]. The ratio of $2\Delta/k_B T_c$ is usually about 1 –

3 for the smaller gap(s) and 4 – 9 for the largest ones for a number of iron-based superconductors, as summarized in Ref. [81] (shown in Fig. 2.15), compared to the weak-coupling limit of 3.53 predicted by the BCS theory.

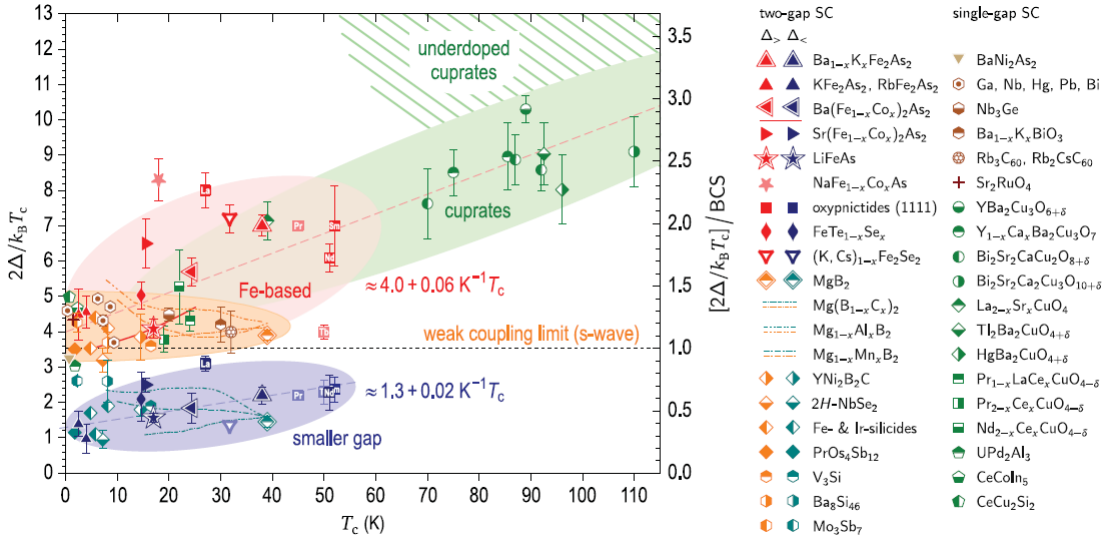


Fig. 2.15. From Ref. [81]. The gap ratios, $2\Delta/k_B T_c$, for different families of single- and two-gap superconductors vs their superconducting transition temperatures (T_c) at ambient pressure. The ratio $2\Delta/k_B T_c$ of iron-based superconductors (122, 1111, 111 and 11 structures) is usually about 1 – 3 for the smaller gaps and 4 – 9 for the larger ones.

CHAPTER 3

Experimental methods

3.1 Fourier transform infrared (FTIR) spectroscopy

3.1.1 Introduction

Fourier transform infrared (FTIR) spectroscopy is a powerful technique and one of the most widely applied analysis methods for studying the interaction of infrared light with matter. The infrared region generally covers frequencies from 10 cm^{-1} to 13000 cm^{-1} . Based on the energy (or frequency), the infrared region is approximately divided into near-infrared ($7000\text{ cm}^{-1} - 13000\text{ cm}^{-1}$), mid-infrared ($600\text{ cm}^{-1} - 7000\text{ cm}^{-1}$) and far-infrared ($10\text{ cm}^{-1} - 600\text{ cm}^{-1}$) regions. For superconductivity, magnetic and structural transitions in iron-based materials, the far-infrared and mid-infrared region are more important. FTIR spectroscopy can be

used to measure infrared properties of samples in the reflectance or transmission geometry. Clearly, for opaque bulk crystals, we obtain FTIR spectroscopy data in the reflectance geometry.

The basic concept of a symmetric Fourier transform infrared spectrometer is based on Michelson's design of an interferometer. The Michelson interferometer is a device that divides a beam of radiation into two paths and then recombines the two beams after a path difference has been introduced. So that interference between the two beams occurs. The variation of intensity of the beam emerging from the interferometer is measured as a function of path difference by a detector. Figure 3.1 shows a common form of Michelson interferometer. It consists of a light source, a beamsplitter, a detector and two mutually perpendicular plane mirrors, one of which is fixed and the other can move along an axis that is perpendicular to its plane. When a collimated beam is incident on the beamsplitter, the beam can be partially reflected to the fixed mirror and partially transmitted to the movable mirror. Ideally, the portion of both transmission and reflectance is 50%. When the beams return to the beamsplitter, they interfere and are again partially reflected and partially transmitted. Because of the effect of interference, the intensity of the beam passing to the detector depends on the difference in path of the beams (δ) in the two arms of the interferometer. The variation in the intensity of the beams

into the detector as a function of the path difference ultimately yields the spectral information in the Fourier Transform spectrometer.

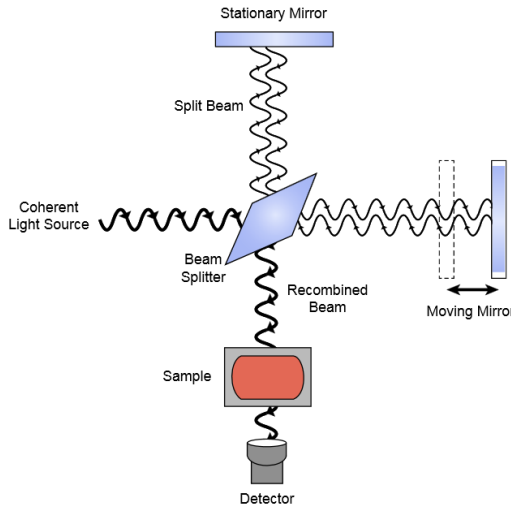


FIG. 3.1. Basic outline of a Michelson interferometer [82].

For monochromatic radiation, the interferogram can be expressed as [83]:

$$S(\delta) = B(\tilde{\nu}_0) \cos 2\pi\tilde{\nu}_0\delta \quad (3.1)$$

The $S(\delta)$ represents the ac signal measured by the detector, $B(\tilde{\nu}_0)$ is the single beam spectral intensity, and $\tilde{\nu}_0$ (cm^{-1}) is the wavenumber (or inverse wavelength) of the monochromatic radiation, $\tilde{\nu}_0 = 1/\lambda_0$. Mathematically, $S(\delta)$ is the cosine Fourier transform of $B(\tilde{\nu}_0)$.

In common rapid-scanning Michelson interferometers, the movable mirror is moved at a constant velocity V' ($\text{cm} \cdot \text{s}^{-1}$) (a continuous-scan interferometer). So,

$\delta = 2V't$, the actual interferogram is measured as a function of time $S(t)$, rather than a function of retardation $S(\delta)$.

For broadband spectral sources, the interferogram can be represented by the integral [83]:

$$S(\delta) = \int_{-\infty}^{\infty} B(\tilde{\nu}) \cos 2\pi\tilde{\nu}\delta d\tilde{\nu} \quad (3.2)$$

So that the other Fourier transform pair is

$$B(\tilde{\nu}) = \int_{-\infty}^{\infty} S(\delta) \cos 2\pi\tilde{\nu}\delta d\delta \quad (3.3)$$

Where $S(\delta)$ is an even function, so Eq. (3.3) can be rewritten as

$$B(\tilde{\nu}) = 2 \int_0^{\infty} S(\delta) \cos 2\pi\tilde{\nu}\delta d\delta \quad (3.4)$$

The integral in Eq. (3.4) is infinite, but obviously, the interferogram is measured only over a finite mirror displacement $\delta/2 \leq \delta_{max}/2$. So that the maximum resolution will be $\Delta\nu = 1/\delta_{max}$ [84]. Instead of truncating the interferogram directly, the problem is solved using an appropriate apodization, an extrapolation applied to $S(\delta)$. In the real measurement, several steps are usually taken from interferogram to spectrum: apodization, phase computation, zerofilling, Fourier transformation of the interferogram, and phase correction. The parameters in these steps should be well chosen and these steps are usually implemented by FTIR spectrometer software like OPUS.

3.1.2 Experimental equipment and technique

A Bruker Vertex 80v vacuum spectrometer is a symmetric FTIR spectrometer as described in the previous section. This commercial instrument is designed for transmission measurements. An ultra-high vacuum chamber attached to the Bruker spectrometer and a reflectance unit (Fig. 3.2), both designed and constructed in-house, allow near-normal incidence reflectance measurements. A vertical translator was used to move the sample and a reference gold mirror into the beam path. A cryostat was used for low temperature measurements, and the sample and reference mirror were mounted on the cold finger. The vacuum obtained at room temperature is 2.8×10^{-8} mbar. The temperature range can be measured is 4.2 K – 400 K. An *in situ* gold evaporator is equipped for evaporating a thin gold layer (about 150 nm thickness) on the sample surface to eliminate systematic uncertainties due to the effect of beam path difference of sample and reference mirror, slow drifts in the intensity of the light source, and the geometry and roughness effect of the sample.

The experimental steps include:

1. Mount a sample on to a sample holder.
2. Mount sample and reference mirror on the cold finger of the cryostat, and align sample and reference so that they have same tilt and same height.

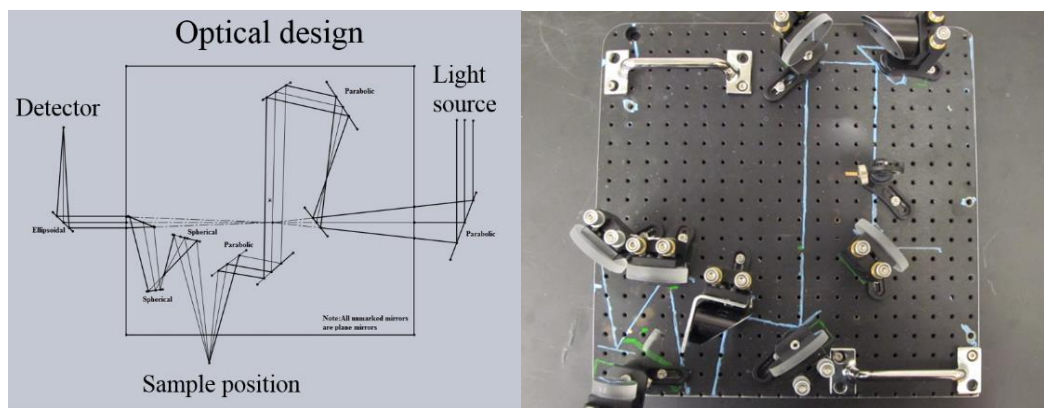


FIG. 3.2. Optical design of reflectance unit (left) and arrangement of mirrors (right).

3. Attach cryostat to the vacuum chamber and align the reflectance beam path on the center of the sample.
4. Attach gold evaporator (with gold on tungsten wire) to the vacuum chamber.
5. Pump the chamber to ultra-high vacuum.
6. Measure the spectrum of the sample with respect to the gold reference from room temperature to lowest temperature 4.2 K. Then heat up back to room temperature.
7. Evaporate gold on the surface of sample. Then measure spectrum from gold-coated sample with respect to the reference from room temperature to 4.2 K.

By dividing the ratios of the two reflectance spectra obtained in steps 6 and 7, we can get very accurate reflectance spectrum over the measured frequencies. With a combination of different light sources, beamsplitters, and infrared detectors, we measured spectra in a wide frequency range of 20 – 8000 cm^{-1} .

3.1.3 Data analysis

Reflectance itself is very useful information to study the optical phonons, superconducting gap energies, and electron-bosonic interactions. However, the optical constants cannot be read directly from reflectance spectrum. We usually need to perform Kramers-Kronig transformation to obtain the phase $\theta(\omega)$ (imaginary part of the complex reflectance), then we can calculate the optical constants, e.g. complex optical conductivity and complex dielectric functions.

The complex reflectance is defined by

$$\tilde{r}(\omega) = r(\omega)e^{i\theta(\omega)} \quad (3.5)$$

The measured reflectance amplitude is $R(\omega) = r(\omega)^2$. The dispersion relation for the reflectance and the phase is [85]:

$$\theta(\omega) = \frac{\omega}{\pi} P \int_0^{\infty} \frac{\ln R(\omega') d\omega'}{\omega^2 - \omega'^2} \quad (3.6)$$

Clearly, we don't have spectrum of all the frequencies needed in the Kramers-Kronig transformation to calculate the phase $\theta(\omega)$, and we need to do reasonable extrapolations.

For a typical metal, at low frequencies, Hagen-Rubens extrapolations can be applied. Hagen-Rubens regime is defined by the condition $\omega\tau \ll 1$ (τ is the relaxation time), which means the optical properties are mainly determined by the dc conductivity, and the real part of conductivity σ_1 is frequency independent: $\sigma_{dc} \approx$

$\sigma_1 \gg \sigma_2$. Then reflectance R can be written as $R(\omega) \approx 1 - \left(\frac{2\omega}{\pi\sigma_{dc}}\right)^{1/2}$. Since temperature dependent dc conductivity can be measured from resistivity data, this extrapolation can be done very accurately. For a full-gap superconductor, at zero temperature, the reflectance is 1 below the energy gap. At finite temperature below T_c , the low frequency extrapolation $R(\omega) \approx 1 - A(\omega)^4$ [86] or $R(\omega) \approx 1 - A(\omega)^2$ [87] can be used. Since the data is obtained down to very low frequencies, the extrapolation towards zero frequency doesn't play an important role and hardly changes the optical conductivity. This is not the case for the high frequency end. Typically, beyond the measurement range, the extrapolation of $R(\omega)$ usually has a transparent regime $R(\omega) \propto \omega^{-2}$, then followed by free electron behavior $R(\omega) \propto \omega^{-4}$ [84,88]. However, depending on the exact details of the how high frequency extrapolation is applied, the infrared conductivity could change by about 10%. In order to get more accurate infrared reflectance phase, we combine the results of higher frequency ellipsometry data (see section 3.2) and the infrared reflectance measurements. We use ellipsometry results as wide-range anchor points, and thus do not rely on the details of high frequency extrapolation of measured reflectance. By combining reflectance and ellipsometry data we obtain very accurate infrared optical conductivity [89,90]. The numerical calculation was implemented in MATLAB.

After calculating the phase $\theta(\omega)$, optical constants can be obtained. The complex refractive index $\tilde{N}(\omega) = n(\omega) + i\kappa(\omega)$ can be expressed in terms of $r(\omega)$ and $\theta(\omega)$:

$$n(\omega) = \frac{1-r(\omega)^2}{1-2r(\omega)\cos\theta(\omega)+r(\omega)^2} \quad (3.7)$$

$$\kappa(\omega) = \frac{2r(\omega)\sin\theta(\omega)}{1-2r(\omega)\cos\theta(\omega)+r(\omega)^2} \quad (3.8)$$

And the complex optical conductivity $\tilde{\sigma}(\omega) = \sigma_1(\omega) + i\sigma_2(\omega)$ is:

$$\sigma_1(\omega) = \frac{n(\omega)\kappa(\omega)\omega}{2\pi\mu_1} \quad (3.9)$$

$$\sigma_2(\omega) = \left(1 - \frac{n(\omega)^2 - \kappa(\omega)^2}{\mu_1}\right) \frac{\omega}{4\pi} \quad (3.10)$$

the complex dielectric function $\tilde{\epsilon}(\omega) = \epsilon_1(\omega) + i\epsilon_2(\omega)$ is:

$$\epsilon_1(\omega) = \frac{n(\omega)^2 - \kappa(\omega)^2}{\mu_1} \quad (3.11)$$

$$\epsilon_2(\omega) = \frac{2n(\omega)\kappa(\omega)}{\mu_1} \quad (3.12)$$

3.2 Spectroscopic ellipsometry

3.2.1 Introduction

Ellipsometry is a very sensitive measurement technique that uses polarized light to characterize bulk materials, thin films, surfaces, and material microstructure. Ellipsometry measures the change in polarization state of an electromagnetic wave reflected from (or transmitted through) the surface of a sample. In contrast to

standard reflectivity studies which only record the power reflectance, two independent parameters (usually expressed as Ψ and Δ) are measured, thus allowing a direct evaluation of the complex optical constants. Furthermore, as the magnitude of the reflected light does not enter the analysis, ellipsometric studies do not require reference measurements and thus have higher accuracy.

The wavelengths used in ellipsometry measurements usually cover the near-infrared, visible and ultra-violet spectral ranges. During a measurement, a single wavelength is selected by a monochromator. Other wavelengths are selected as the measurement proceeds in time.

Fig. 3.3 shows the geometry of an ellipsometric reflectance experiment. A linearly polarized light beam reflects from a sample surface, and produces an ellip-

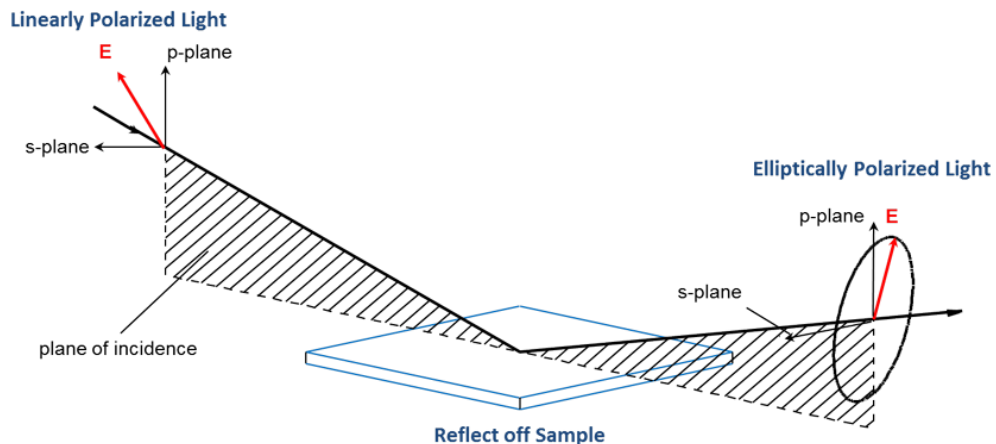


FIG. 3.3. Geometry of an ellipsometric reflectance experiment [91].

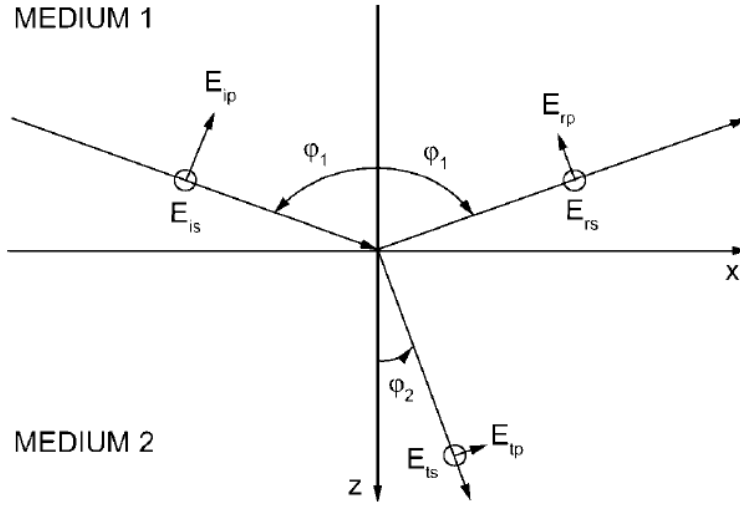


FIG. 3.4. Reflection and transmission of a plane wave at the planar interface [92].

tically polarized light. Electric fields parallel and perpendicular to the plane of incidence are considered p- and s- polarized, respectively. The measured ellipsometric coefficients are expressed as Ψ and Δ . They are related to the ratio of Fresnel reflectance coefficients for p- and s- polarized light \tilde{R}_p and \tilde{R}_s :

$$\tilde{\rho} = \frac{\tilde{R}_p}{\tilde{R}_s} = \tan \Psi e^{i\Delta} \quad (3.13)$$

where \tilde{R}_p and \tilde{R}_s are expressed:

$$\tilde{R}_p = \frac{\tilde{N}_1 \cos \varphi_2 - \tilde{N}_2 \cos \varphi_1}{\tilde{N}_1 \cos \varphi_2 + \tilde{N}_2 \cos \varphi_1} \quad (3.14)$$

$$\tilde{R}_s = \frac{\tilde{N}_1 \cos \varphi_1 - \tilde{N}_2 \cos \varphi_2}{\tilde{N}_1 \cos \varphi_1 + \tilde{N}_2 \cos \varphi_2} \quad (3.15)$$

As indicated in Fig. 3.4, for an optical plane wave incident on the planar interface between two media ($\tilde{N} = n + ik$), Snell's law gives:

$$\tilde{N}_1 \sin \varphi_1 = \tilde{N}_2 \sin \varphi_2 \quad (3.16)$$

For a typical measurement, medium 1 is air, medium 2 is a sample. The information of optical constants of the sample are related to Ψ and Δ in this way.

Fig. 3.5 shows a ellipsometer configuration with a rotating analyzer. Unpolarized light is produced by a light source and then sent through a polarizer. The polarizer chooses a preferred electric field orientation to pass through. The polarizer axis is oriented between the p- and s- planes. The linearly polarized light reflects from the sample surface and becomes elliptically polarized, then travels through a continuously rotating analyzer. Depending on the analyzer orientation relative to the elliptical polarized state coming from the sample, the transmitted light goes into the detector. The detector then converts light to electronic voltage, and determines the reflected polarization. This information is compared to the known input polarization to determine the polarization change caused by the sample reflection. Then the two important parameters Ψ and Δ will be obtained. This is typically how the ellipsometry measures Ψ and Δ .

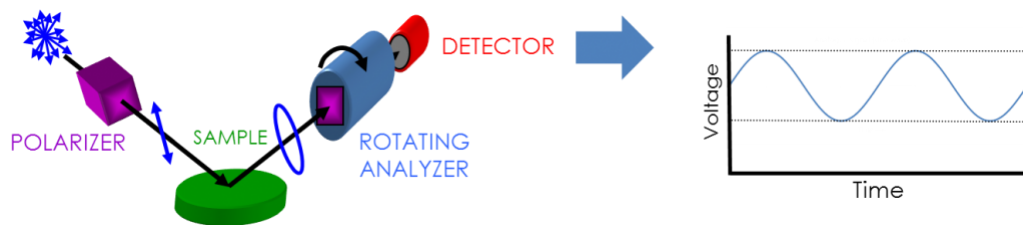


FIG. 3.5. Common ellipsometer configuration with rotating analyzer and the signal received from the detector [91].

To determine the sample material's properties of interest, such as film thickness and optical constants, a model is usually needed. The model is used to calculate the predicted response from Fresnel's equations which describe each material with thickness and optical constants. Through the fitting procedure, the unknown optical constants are determined from experimental data sets.

3.2.2 Experimental equipment and techniques

A Woollam variable-angle spectroscopic ellipsometer (VASE) was used for the ellipsometry measurements. The ellipsometer consists of a light source (with a monochromator), input unit (including a polarizer stage and an AutoRetarder), sample stage (on the top of goniometer), and a detector (mounted on a rotational arm). The measured photon energies are in the range 0.6 eV – 6 eV.

For cryogenic measurements, an ultra-high vacuum chamber is needed to prevent ice formation on the surface of a sample. We built an ultra-high vacuum chamber to enable cryogenic ellipsometry measurements. The experimental setup is shown in Fig. 3.6. We used a custom-made UV quartz tube, which has high UV and visible transmission, that is fused to a stainless steel conflat flange. The cylindrical symmetry of the quartz tube allows us to choose a wide range of angles

of incidence for ellipsometry measurement. The quartz tube is attached to the bottom of the stainless-steel vacuum chamber. We use a vertical translation stage to select the vertical height of the sample on the cryostat. This setup sits on top of a horizontal translation and tilt stage, so that the sample can be tilted and translated horizontally, and in the end the sample surface is aligned with the rotational axis of the goniometer (rotation stage).

The quartz tube has anisotropic strain on the surface when the tube is in vacuum. The retardance effect of the quartz tube is significant. In order to quantify the retardance effect of the quartz tube, we measure a known SiO_2/Si reference sample inside the tube to account for the change of polarization state due to the quartz tube.

This experiment needs accurate optical alignment:

- a. The rotation axis of manual goniometer has to be perfectly aligned with the rotation axis of auto goniometer of the ellipsometer.
- b. The surface plane of a sample needs to be perfectly aligned with the surface of known reference SiO_2/Si wafer in 3-D space (the surface planes needs to be parallel and have same height on cryostat).
- c. The sample surface should be aligned with rotation axis of goniometer.

With this setup, we achieved a vacuum of 1.2×10^{-8} mbar at room temperature and the temperature range that can be measured is 4.2 K – 400 K.

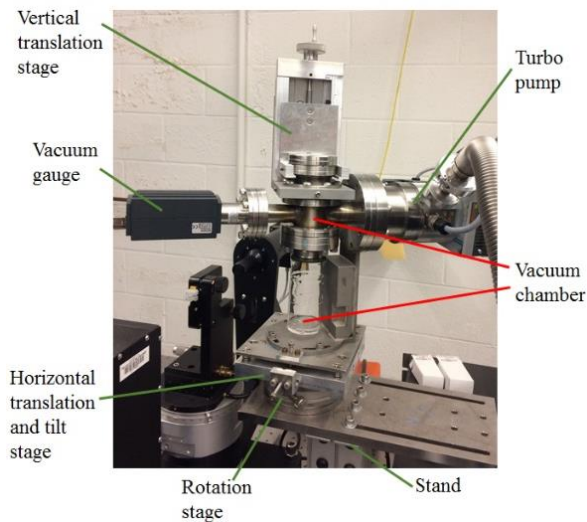
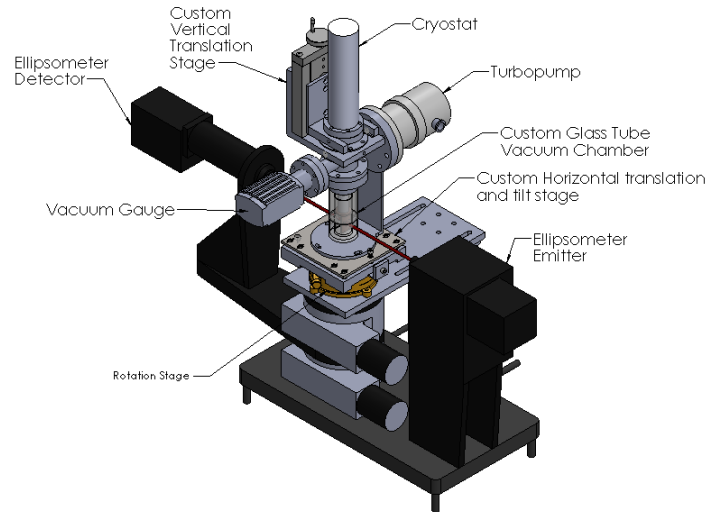


FIG. 3.6. Up: cryogenic ellipsometry setup 3-D model [93]. Down: the lab built setup. The rotation stage, horizontal translation and tilt stage, vacuum chamber and the vertical translation stage (vacuum gauge, turbo pump, cryostat) are designed and built for cryogenic measurements.

3.2.3 Data analysis

We use WVASE32 software to analyze the ellipsometry data and obtain optical constants. For a typical real material, an exact equation of optical constants cannot be written and the answer is over-determined with hundreds of experimental data points for a few unknowns.

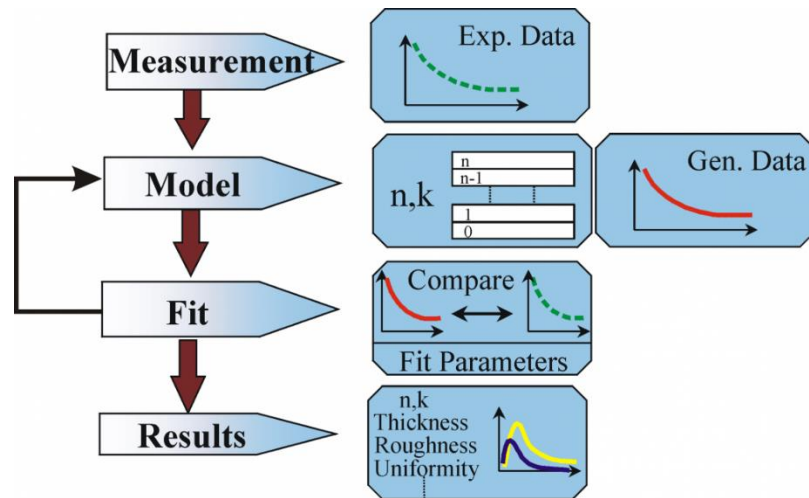


FIG. 3.7. Flow chart of ellipsometry data analysis using WVASE32 [91].

Fig. 3.7 shows the flow chart of data analysis using WVASE32. The procedure is as follows: After the spectroscopic ellipsometry data is acquired, a layered model is constructed to describe the sample. The model is used to calculate the predicted response from Fresnel's equations which describe each layer of material with thickness and optical constants. Unknown quantities will be given an initial

estimate for calculation. Then the calculated values are compared to experimental data set. Any unknown material properties can then be varied to improve the match between experimental data and calculation. Through multiple iterations, one can find the best match between the model and the experiment. Usually, the mean squared error will be used as an indicator to quantify the difference between experimental data and the model. In the end, the best fit is achieved with least mean squared error.

For a special case like a bulk isotropic material, the pseudo-dielectric function has an exact solution [92]:

$$\langle \tilde{\epsilon} \rangle = \langle \epsilon_1 \rangle + i \langle \epsilon_2 \rangle = \sin^2 \varphi \left\{ 1 + \left[\frac{1-\tilde{\rho}}{1+\tilde{\rho}} \right]^2 \right\} \tan^2 \varphi \quad (3.17)$$

For a uniaxial crystal (for example 122 iron-based materials in the tetragonal crystal structure) the formulas relating the complex dielectric function to the measured ellipsometric coefficients are more complicated. The detailed discussion of these formulas is deferred to appendix A.

CHAPTER 4

Rare-earth doped CaFe_2As_2

4.1 Introduction

The investigation of magnetic, structural, transport, and superconducting properties of pure and doped crystals of the 122 family of iron arsenides AFe_2As_2 ($\text{A} = \text{Ba}, \text{Ca}, \text{Sr}$) has played a pivotal role in furthering our understanding of the fascinating many-body interactions and phase transitions observed in the iron pnictides and iron chalcogenides [94–96]. The parent compounds in the 122 family go through a tetragonal-to-orthorhombic structural transition coupled with antiferromagnetic spin-density-wave (SDW) order at low temperatures [94–96]. In CaFe_2As_2 , pressure-induced superconductivity only emerges under non-hydrostatic experimental conditions [36,37,97]. Under hydrostatic pressure,

instead of superconductivity, a so-called collapsed tetragonal (CT) phase occurs resulting in a dramatic *c*-axis reduction (about 10%) without breaking symmetry [38,98]. CaFe_2As_2 is much more sensitive to stress anisotropy compared to BaFe_2As_2 and SrFe_2As_2 which also show pressure-induced superconductivity and CT phase but at much higher pressure [42,99–101].

The CT phase, which is driven by interlayer As-As separation [46,48], can also be stabilized by chemical substitution in CaFe_2As_2 at ambient pressure. The antiferromagnetism in CaFe_2As_2 is suppressed by appropriate doping, for example, by substituting rare-earth Pr and Nd on the Ca site [46], Rh on the iron site [102] or phosphorus on the As site, [103] leading to the emergence of the CT phase. Depending upon the trivalent rare-earth ion substitution in the system [46], CaFe_2As_2 can maintain either the uncollapsed tetragonal (UT) structure with La substituent, or undergoes a phase transition at low temperature from the UT structure to the CT structure with Nd or Pr substituents. Hence, rare-earth doped CaFe_2As_2 crystals provide us the chance to study (in a controlled manner) the UT and CT phases at ambient pressure [104–108]. The rare-earth substituents are believed to dope electrons into the system in addition to varying the chemical pressure due to their different ionic radii compared to the calcium ion. In the CT phase, Fe local moments are quenched [38,105], spin fluctuations are

suppressed [39], and electron correlations are believed to be reduced [40]. Angle-resolved photoemission spectroscopy (ARPES) results show that there is reconstruction of the Fermi surface in the CT structure in strained crystals of CaFe_2As_2 , including the complete disappearance of the hole pocket at the zone center (Γ point) [41,109], consistent with theoretical expectation [48,110]. However, very recent ARPES experiments on Pr-doped CaFe_2As_2 show that across the CT phase transition, the hole pocket at Γ point does not disappear completely [111], which is different from the CT phase in the parent compound under internal strain [41,109]. The added diversity in the rare-earth doped CaFe_2As_2 system provides us the opportunity to study with optical spectroscopy the nature of many-body interactions. Unlike previous infrared work [112], we investigate both $\text{Ca}_{0.8}\text{La}_{0.2}\text{Fe}_2\text{As}_2$ and $\text{Ca}_{0.85}\text{Pr}_{0.15}\text{Fe}_2\text{As}_2$ crystals to compare the properties of the UT phase of the former material with the UT and CT phases of the latter material.

In this chapter [90], the frequency and temperature dependent *ab*-plane optical constants of $\text{Ca}_{0.8}\text{La}_{0.2}\text{Fe}_2\text{As}_2$ and $\text{Ca}_{0.85}\text{Pr}_{0.15}\text{Fe}_2\text{As}_2$ crystals are obtained through optical spectroscopy. An interesting finding is that the scattering rate saturates above ~ 200 K in the UT structure in La-doped and Pr-doped CaFe_2As_2 . However, the resistivity continues to increase above 200 K which we find to be a consequence of the loss of mobile carriers. The loss of Drude spectral weight of

mobile carriers with increasing temperature is seen in a wide temperature range in the uncollapsed tetragonal phase, and this spectral weight is recovered about 0.5 eV, much larger than the Fermi energy scale in these semi-metals. The scattering rate in La-doped CaFe_2As_2 between 5 K and 150 K is dominated by a quadratic temperature dependent term ascribed to significant electron-electron interactions. The frequency dependence of the scattering rate obtained from the extended Drude analysis is in accord with its temperature dependence. We document the impact of the structure collapse transition on the infrared properties of the Pr doped system, and also compare these properties with those of the UT phase of La doped CaFe_2As_2 . We find that the plasma frequency and scattering rate of free carriers decrease across the CT phase transition. Optical interband transitions are also affected by electronic structure reconstruction across CT phase transition.

4.2 Samples and experiments

Single crystals of $\text{Ca}_{0.8}\text{La}_{0.2}\text{Fe}_2\text{As}_2$ and $\text{Ca}_{0.85}\text{Pr}_{0.15}\text{Fe}_2\text{As}_2$ were grown using the FeAs self-flux method [46]. At these rare-earth doping levels, the spin density wave transition is suppressed. The temperature-dependent resistivity data for $\text{Ca}_{0.8}\text{La}_{0.2}\text{Fe}_2\text{As}_2$ shows metallic behavior with no signs of a magnetic or structural

phase transition. In Pr-doped sample, the CT phase occurs below 70 K with a subtle kink in the resistivity curve and a dramatic change in the Hall coefficient [46]. The size of $\text{Ca}_{0.8}\text{La}_{0.2}\text{Fe}_2\text{As}_2$ crystals is as large as $10\times 10\times 2\text{ mm}^3$, and the size of $\text{Ca}_{0.85}\text{Pr}_{0.15}\text{Fe}_2\text{As}_2$ crystals is as large as $5\times 5\times 1\text{ mm}^3$. It is easy to obtain relatively flat and shiny *ab*-plane surfaces by cleaving.

Near-normal incidence reflectance measurements on the *ab*-plane surfaces were performed with the Bruker Vertex 80v Fourier Transform Infrared (FTIR) spectrometer in the frequency range 60 cm^{-1} - 8000 cm^{-1} and temperature range 5 K – 300 K (Appendix A). An *in situ* gold evaporation method similar to that described in Ref. [113] was used to obtain absolute reflectance. Ellipsometry measurements were performed with a Woollam variable-angle spectroscopic ellipsometer (VASE) in the frequency range 4800 cm^{-1} - 40000 cm^{-1} and temperature range 5 K – 300 K (Appendix A). In this frequency range, the complex optical conductivity was obtained directly from the measured ellipsometric coefficients. The infrared conductivity at lower frequencies is obtained by Kramers-Kronig (KK) transformation on reflectance constrained by ellipsometry results [89]. Both Hagen-Rubens and Drude extrapolations [84] constrained by *dc* conductivity of the crystals were employed at very low frequencies in order to perform KK

transformations. The optical constants obtained in the frequency range of interest are hardly affected by the choice of the very low frequency extrapolation function.

4.3 Results and discussion

4.3.1 Optical conductivity and spectral weight

The real part (σ_1) of the optical conductivity is shown in Fig. 4.1. The $\text{Ca}_{0.8}\text{La}_{0.2}\text{Fe}_2\text{As}_2$ crystal shows metallic behavior at low temperatures with a clear Drude-like feature at low frequencies. However, at higher temperatures, there is a non-monotonic frequency dependence that appears to depart from Drude-like conductivity. For the Pr-doped CaFe_2As_2 crystal, spectra have been measured between 300 K and 100 K in the UT phase, and at 40 K and 5 K in the CT phase. The optical conductivity in both phases is consistent with metallic behavior. The occurrence of the CT phase transition is apparent in the shift of the infrared-active, Fe-As phonon center frequency (Appendix B).

We calculate the spectral weight (SW) as a function of frequency via the integral of σ_1 for both materials:

$$\text{SW}(\omega) = \int_0^\omega \sigma_1(\omega') d\omega' \quad (4.1)$$

This integral is calculated for optical conductivities at different temperatures. For conducting materials at low frequencies, the spectral weight is proportional to the square of the plasma frequency, and hence the number of charge carriers in the material [84]. If we assume the charge carriers have masses equal to the free electron mass, we may rewrite the spectral weight in terms of an effective number of carriers N_{eff} per formula unit in a primitive cell V_0 :

$$N_{eff}(\omega) = \frac{2m_e V_0}{\pi e^2} \int_0^\omega \sigma_1(\omega') d\omega' \quad (4.2)$$

The effective number of carriers are shown in Fig. 4.2. It is clear that at lower frequencies, the spectral weight decreases with increasing temperature. Phase space restrictions for the hole-like bands in these semi-metals due to the Pauli exclusion principle may contribute to spectral weight redistribution on the order of the Fermi energy (~ 0.05 eV or 400 cm^{-1}). However, we note that the total spectral weight is conserved about 4000 cm^{-1} (~ 0.5 eV) for the data in the UT phase. This spectral weight recovery energy scale is about one order of magnitude larger than the Fermi energy scales (~ 0.02 eV to 0.07 eV) of the electron and hole carriers in the rare-earth doped CaFe_2As_2 . Interactions between charge carriers redistribute the spectral weight to energies much higher than the Fermi energies. We also note that the energy scale over which the spectral weight is recovered is not too different from that seen in the cuprates (~ 2 eV) [114]. In our work, the Fermi energy is

defined from the Fermi level to the bottom of the electron-like bands (for electron pockets) or the top of the hole-like bands (for hole pockets). In other words, the Fermi energy is either the occupied bandwidth of the electron-like bands or the unoccupied bandwidth of the hole-like bands.

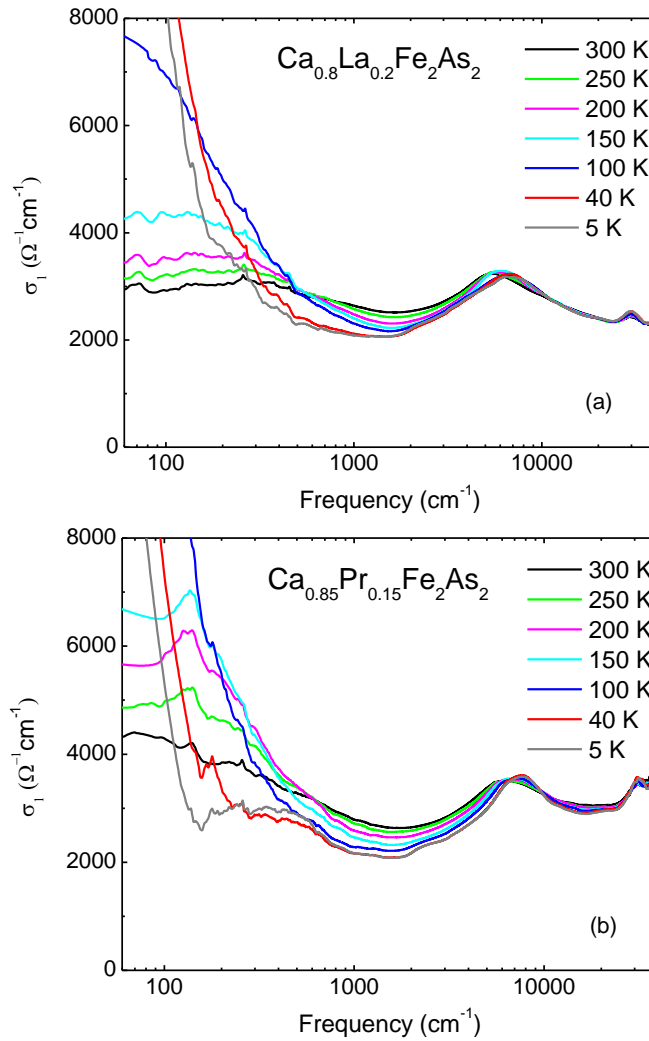


FIG. 4.1. The real part of the ab -plane optical conductivity σ_1 is plotted as a function of frequency at different temperatures for (a) $\text{Ca}_{0.8}\text{La}_{0.2}\text{Fe}_2\text{As}_2$ and (b) $\text{Ca}_{0.85}\text{Pr}_{0.15}\text{Fe}_2\text{As}_2$.

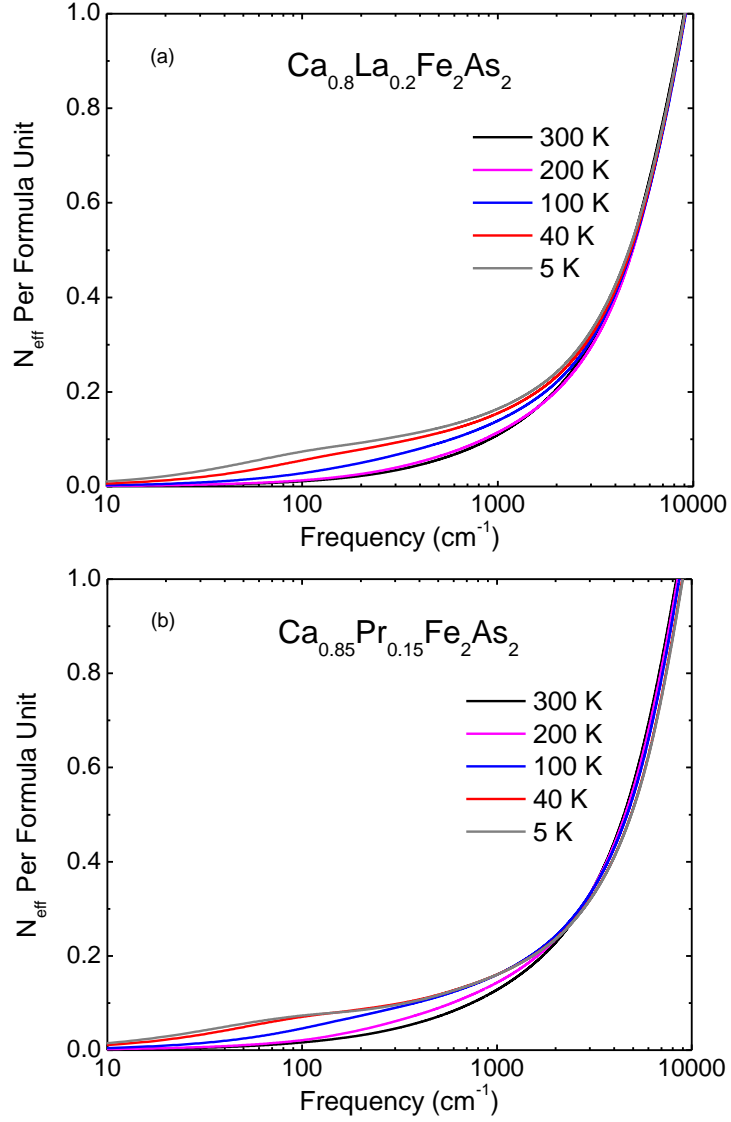


FIG. 4.2. Effective number of carriers N_{eff} at different temperatures for (a) $\text{Ca}_{0.8}\text{La}_{0.2}\text{Fe}_2\text{As}_2$ and (b) $\text{Ca}_{0.85}\text{Pr}_{0.15}\text{Fe}_2\text{As}_2$.

We fit the complex conductivity with the Drude-Lorentz model: [84]

$$\sigma(\omega) = \frac{\omega_p^2}{4\pi} \frac{1}{1/\tau - i\omega} + \sum_j \frac{\Omega_j^2}{4\pi} \frac{\omega}{i(\omega_j^2 - \omega^2) + \omega/\tau_j} \quad (4.3)$$

where the first term is the Drude component which represents free-carrier response, and latter terms are Lorentz components, which represent the response

associated with localized charges and/or optical interband transitions. In the UT structures of both samples, we find that only one Drude term and one overdamped, mid-infrared Lorentz oscillator is sufficient for a very good low-frequency fit (Appendix C). This fitting procedure for the infrared conductivity has been used previously in the literature [115,116]. Due to the multiband nature of iron-based materials [95,96], it is usually more difficult to interpret the infrared conductivity. Other researchers have fit their data with two Drude terms in which one is narrow and the other is very broad [117–119]. However, the two Drude model does not provide satisfactory fits to our infrared data at higher temperatures as we show in Appendix C. Moreover, the scattering rate parameter of the broad Drude appears to be unphysical [116] because it is several times the value of the Fermi energies of the electron and hole carriers.

4.3.2 Free carrier response

We first focus on the Drude component which represents the free-carrier response. The square of the plasma frequency ω_p^2 and scattering rate $1/(2\pi c\tau)$ normalized to the respective values at 300 K are shown in Figs. 4.3(a) and (b) as a function of temperature. A discontinuity in the magnitude of the plasma frequency occurs below CT transition temperature of Pr-doped CaFe_2As_2 , which implies a

discontinuous reduction of carrier density. This is consistent with the ARPES results on $\text{Ca}_{0.85}\text{Pr}_{0.15}\text{Fe}_2\text{As}_2$ which show a significant reduction of a large hole pocket and the disappearance of the small hole pocket after structure collapse [111]. Recently, another structure collapse material $\text{CaFe}_2(\text{As}_{0.935}\text{P}_{0.065})_2$ has been studied, as described in Ref. [120]. In $\text{CaFe}_2(\text{As}_{0.935}\text{P}_{0.065})_2$, a noticeable suppression of reflectance occurs between 1000 cm^{-1} and 3500 cm^{-1} , resulting in a deeper valley about 1500 cm^{-1} in σ_1 in the CT phase. This behavior is nominally different from that observed in $\text{Ca}_{0.85}\text{Pr}_{0.15}\text{Fe}_2\text{As}_2$ in our work, probably due to differences in details of the electronic structure. However, similar to $\text{Ca}_{0.85}\text{Pr}_{0.15}\text{Fe}_2\text{As}_2$, in $\text{CaFe}_2(\text{As}_{0.935}\text{P}_{0.065})_2$ the (total) plasma frequency of Drude contribution decreases across CT phase transition.

Remarkably, scattering rate of both La- and Pr-doped CaFe_2As_2 shows saturation above 200 K clearly indicating the attainment of the Mott-Ioffe-Regel limit of metallic transport. However, the resistivity continues to increase above 200 K as shown in Ref. [46]. We find this to be a consequence of the decrease in number density of mobile carriers and is directly seen in the decrease of the Drude spectral weight (square of the plasma frequency) in Fig. 4.3(a). The decrease of the Drude spectral weight with increasing temperature is consistent with the model

independent analysis shown in Figs. 4.2(a), (b) and discussed in the preceding section.

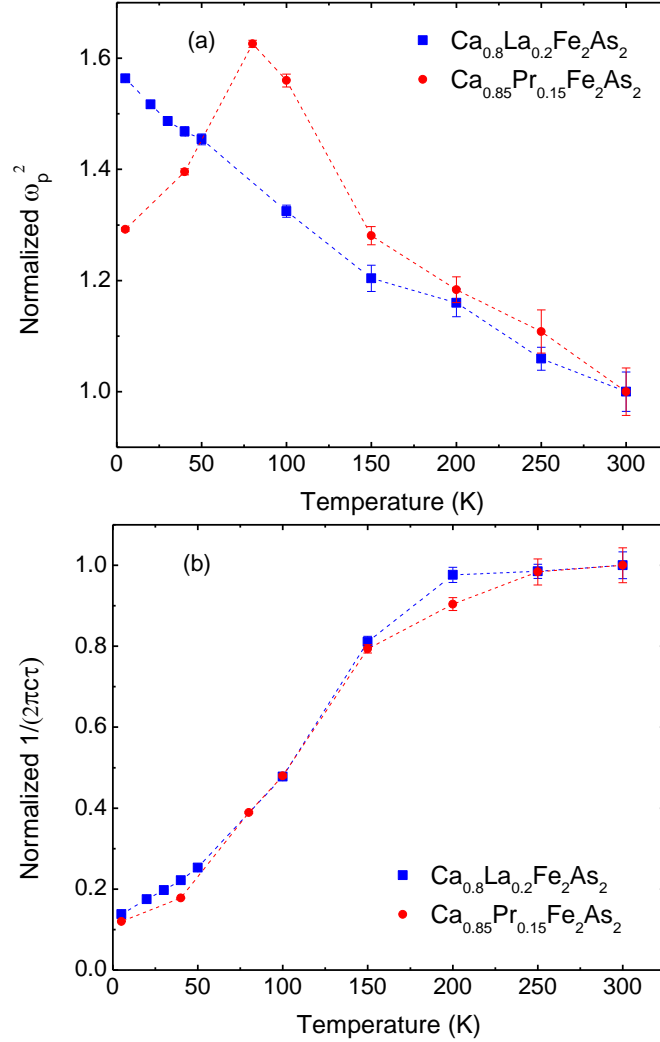


FIG. 4.3. Temperature dependence of the parameters of the Drude term (a) ω_p^2 and (b) $1/(2\pi\tau)$ normalized to the respective values at 300 K for $\text{Ca}_{0.8}\text{La}_{0.2}\text{Fe}_2\text{As}_2$ (blue squares) and $\text{Ca}_{0.85}\text{Pr}_{0.15}\text{Fe}_2\text{As}_2$ (red circles). Dashed lines are guides to the eye.

Another criterion for the Mott-Ioffe-Regel limit is that the quantity $k\ell$ is of order unity. This quantity can be estimated by the resistivity formula for two dimensional

systems: [121]

$$\rho_{2D} = \frac{2\pi\hbar c_0}{e^2 k_F l} \frac{1}{M} \quad (4.4)$$

We find that $k_F l \sim 1$ for $\text{Ca}_{0.8}\text{La}_{0.2}\text{Fe}_2\text{As}_2$ at 300 K, given $\rho_{2D} = 330\mu\Omega \text{ cm}$ obtained from the *dc* limit of σ_1 , $c_0 \sim 5.8 \text{ \AA}$ is the separation of Fe-As layers, and M is the number of Fermi surface sheets (which is 4 here). These materials can be considered quasi-two dimensional systems with nearly cylindrical Fermi surfaces based on the photoemission data of Ref. [111] and Ref. [122]. Hence eq. (4.4) can be used to analyze charge transport in these materials. Yet another criterion for the Mott-Ioffe-Regel limit is that the mean free path becomes comparable to the lattice constant. One can estimate the mean free path (l) of the charge carriers from $l = v_F \tau$. The average Fermi velocity estimated from ARPES in La-doped CaFe_2As_2 is $\sim 2 \times 10^6 \text{ cm/s}$ which translates to a mean free path of 2.7 \AA . This mean free path is smaller than the *a*-axis lattice constant of 3.92 \AA . For the Pr-doped sample, similar calculations to those given above yield $k_F l \sim 2$, and a mean free path of 3.5 \AA which is comparable to the lattice constant of 3.91 \AA [46]. From ARPES results [111,122], the Fermi energy of the mobile carriers i.e. occupied (unoccupied) bandwidths for electrons (holes) are between 0.02 eV and 0.07 eV in UT La- and Pr- doped CaFe_2As_2 which are comparable to the saturated scattering rate \hbar/τ of 0.05 eV for the former and 0.035 eV for the latter material. It

is generally understood that for the quasiparticle picture in Fermi liquid theory to be applicable, \hbar/τ should be much smaller than the Fermi energy. Since \hbar/τ is similar to the Fermi energy of the carriers in the various bands, the quasiparticle picture is hardly valid for transport above 200 K.

Our observations of scattering rate saturation near the Mott-Ioffe-Regel limit that is not directly apparent in the *dc* resistivity in rare-earth doped CaFe_2As_2 are reminiscent of the findings of Hussey *et al* in the cuprate $\text{La}_{2-x}\text{Sr}_x\text{CuO}_4$ [123]. These authors suggest that resistivity continues to increase with increasing temperature beyond the Mott-Ioffe-Regel limit because of the loss of Drude spectral weight due to dominance of electronic correlations in charge transport. It therefore follows that the iron arsenides may be considered as “bad metals”. This does not contradict the observation of resistivity saturation about 600 K in the SrFe_2As_2 system because this phenomenon occurs at resistivities that are beyond the Mott-Ioffe-Regel limit of metallic transport [124].

The temperature dependence of the scattering rate of $\text{Ca}_{0.8}\text{La}_{0.2}\text{Fe}_2\text{As}_2$ and $\text{Ca}_{0.85}\text{Pr}_{0.15}\text{Fe}_2\text{As}_2$ is shown in Fig. 4.4. We fit the UT $\text{Ca}_{0.8}\text{La}_{0.2}\text{Fe}_2\text{As}_2$ scattering rate to the form $a+bT+dT^2$. Even though the quadratic term dominates, the fit can be improved with the addition of a linear temperature dependent term. The coefficient of the linear term “*b*” is $0.56 \text{ K}^{-1}\text{cm}^{-1}$. If we assume that the linear term

arises from electron-phonon scattering, then the dimensionless electron-phonon coupling constant λ can be calculated from the equation [125]:

$$\frac{\hbar}{\tau} = 2\pi\lambda k_B T \quad (4.5)$$

This gives $\lambda = 0.13$ remarkably consistent with previous results that show weak electron-phonon coupling for *ab*-plane transport in the 122-iron arsenides [124].

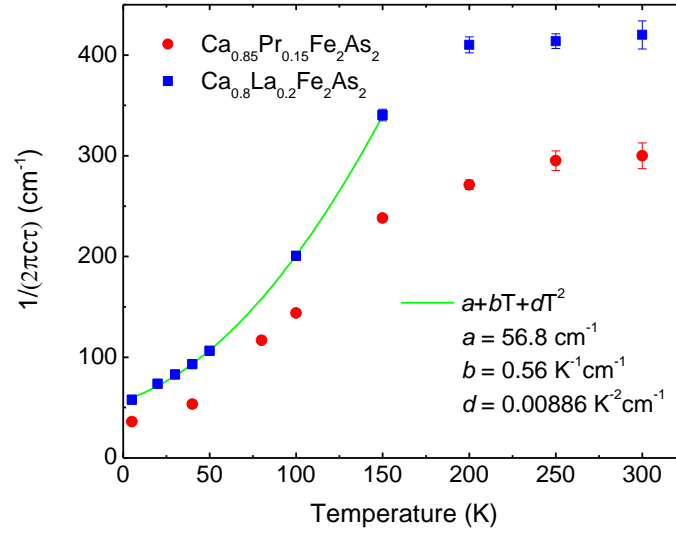


FIG. 4.4. Temperature dependence of the scattering rate $1/(2\pi c\tau)$ of the Drude term of $\text{Ca}_{0.8}\text{La}_{0.2}\text{Fe}_2\text{As}_2$ (blue squares) and $\text{Ca}_{0.85}\text{Pr}_{0.15}\text{Fe}_2\text{As}_2$ (red circles), and fit $\text{Ca}_{0.8}\text{La}_{0.2}\text{Fe}_2\text{As}_2$ scattering rate to the form $a+bT+dT^2$ (green line).

The coefficient of the quadratic term $d = 0.00886 \text{ K}^{-2}\text{cm}^{-1} = 1.67 \times 10^9 \text{ K}^{-2}\text{s}^{-1}$ is much larger than that of a good metal like gold ($\sim 10^7 \text{ K}^{-2}\text{s}^{-1}$) [126,127]. The temperature dependent quadratic term is likely electronic in origin and is similar to that seen in other Mott-correlated and Hund-correlated systems like V_2O_3 , NdNiO_3 ,

La_{0.67}Sr_{0.33}MnO₃, and CaRuO₃ [127,128]. The CT phase transition in Pr-doped CaFe₂As₂ at ~ 70 K with a hysteresis of ~ 30 K [46] precludes the preceding quantitative analysis, but we note that the temperature dependence of the scattering rate above 70 K closely resembles the data for La-doped CaFe₂As₂. However, below the CT phase transition, the normalized scattering rate of Pr-doped CaFe₂As₂ is relatively lower compared to that of the UT La-doped CaFe₂As₂. We attribute this to decreased electronic scattering upon reduction of the Fe magnetic moment in the CT phase [105].

We analyze the quadratic temperature dependence of the scattering rate with the Umklapp electron-electron scattering model of Fermi liquid theory [129]:

$$\frac{\hbar}{\tau} = A \frac{(k_B T)^2}{E_F} \quad (4.6)$$

We estimate the dimensionless constant $A \sim 4$ assuming an average Fermi energy $E_F \sim 30$ meV in La-doped CaFe₂As₂. This value of A is somewhat larger than that obtained for Co-doped BaFe₂As₂ in Ref. [129] indicating comparatively enhanced effective Umklapp scattering in rare-earth doped CaFe₂As₂. A quadratic temperature dependence of the scattering rate has been seen before in Co-doped BaFe₂As₂ up to room temperature without saturation [129,130] and this is likely due to its larger Fermi energy. We expect the scattering rate to saturate in Co-doped BaFe₂As₂ if heated above room temperature. Clearly, even higher

temperatures are required for attaining the Mott-Ioffe-Regel limit in conventional metals that possess larger Fermi energy [121]. Saturation of scattering rate has been observed by infrared spectroscopy in the iron chalcogenide $\text{FeTe}_{0.55}\text{Se}_{0.45}$, a system with a low Fermi energy and strong electronic correlations [131]. In the La-doped CaFe_2As_2 we see a crossover from a predominantly quadratic temperature dependent scattering rate below 150 K indicating the presence of coherent, mobile charges to saturation of the scattering rate above 200 K associated with incoherent transport. It appears that the main reason for the saturation of the scattering rate in the rare-earth doped CaFe_2As_2 systems is enhanced electron-electron scattering that increases with temperature leading to a breakdown of the quasiparticle picture. The large scattering rate is due to a combination of reasons: low Fermi energy of charge carriers; both normal and Umklapp scattering events between electrons and holes contributing to enhanced dissipation; and coherent carriers scattering off incoherent charges. At low temperatures, where the quasiparticle concept may be valid as exemplified by eq. (4.6), there is significant spectral weight in the over-damped Lorentz oscillator (see the oscillators labeled Lorentzian 1 in Appendix C). Some of this spectral weight is due to incoherent and localized charges that coexist with mobile charges. Moreover, an increasing number of mobile charges become incoherent with increasing temperature as seen

by the decrease of Drude spectral weight with increasing temperature, and that this spectral weight is recovered at an energy scale of ~ 0.5 eV which is much larger than the Fermi energies of the electrons and holes. Taken together, the observations in our work make it difficult to classify the rare-earth CaFe_2As_2 system as a conventional Fermi liquid.

In order to confirm the results of the preceding analysis based on fits to the Drude-Lorentz model, we perform the extended Drude model analysis to examine the frequency dependence of scattering rate. Here we use the form [132]:

$$\frac{1}{\tau(\omega)} = -\frac{\omega_p^2}{\omega} \text{Im} \left(\frac{1}{\tilde{\epsilon}(\omega) - \epsilon_H} \right) \quad (4.7)$$

where ω_p^2 is calculated from the integral of σ_1 up to 500 cm^{-1} , $\tilde{\epsilon}(\omega)$ is the complex dielectric function and ϵ_H represents the contribution of higher energy interband transitions. Note that the choice of upper frequency cutoff in the integral used for calculating ω_p^2 does not affect the frequency dependence of the scattering rate. Fig. 4.5(a) and (b) show frequency dependent scattering rate of La- and Pr-doped CaFe_2As_2 respectively for representative temperatures. At high temperatures (like 200 K for $\text{Ca}_{0.8}\text{La}_{0.2}\text{Fe}_2\text{As}_2$ shown in Fig. 4.5(a)), the scattering rate hardly shows frequency dependence, which is consistent with saturation of scattering rate as a function of temperature that is extracted from fits of the conductivity to a one Drude-one Lorentz model. Low temperature scattering rate follows a quadratic form

$C+B\omega^2$ [133], which gives similar coefficient B for both samples. A linear frequency dependent term is not included because it does not improve the fits. Such a term may be relevant at frequencies below the 60 cm^{-1} lower cutoff of our data. According to Ref. [133], the upper cutoff frequency for the quadratic fit at each temperature is determined by noting that $\hbar\omega$ should be smaller or comparable to $2\pi k_B T$. We also note that the temperature dependence of the low frequency limit for $1/\tau(\omega, T)$ based on the extended Drude model is essentially the same as the temperature dependence of the scattering rate obtained from the Drude-Lorentz model and plotted in Fig. 4.4. If we compare the coefficients of the temperature dependent quadratic term (from Drude-Lorentz analysis and extended Drude analysis) and the frequency dependent quadratic term (from extended Drude analysis) of the scattering rate in La-doped CaFe_2As_2 , and use the scattering rate form [133,134]:

$$\frac{1}{\tau}(\omega, T) \propto A_0 [(\hbar\omega)^2 + (p\pi k_B T)^2] \quad (4.8)$$

we get $p = 1.53$. This value of p is very close to the value obtained in $\text{BaFe}_{1.8}\text{Co}_{0.2}\text{As}_2$ and underdoped cuprates [134,135]. The value of p should be 2 for a conventional Fermi liquid.

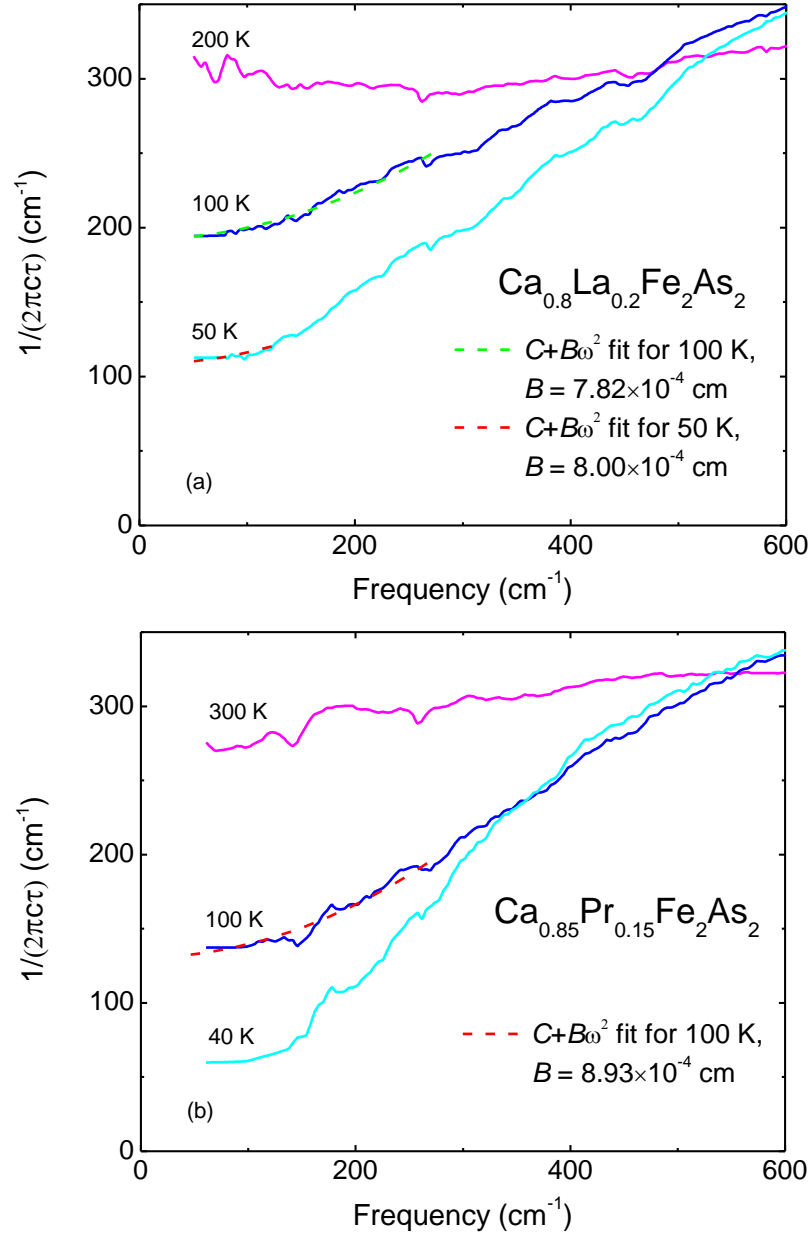


FIG. 4.5. Frequency dependent scattering rate of (a) La- and (b) Pr-doped CaFe_2As_2 . Scattering rate of both samples shows saturation at high temperatures (scattering rate is flat and frequency independent). For temperatures $\leq 100 \text{ K}$, the quadratic term coefficient B is temperature independent in La-doped CaFe_2As_2 , and is similar in magnitude to that in the Pr-doped sample in the UT phase at 100 K. However, in the Pr-doped sample in the CT phase (40 K), the scattering rate curve is clearly different from that in the UT phase (100 K), which indicates reconstruction of the Fermi surface.

4.3.3 Interband transitions

Next we discuss the physical interpretation of the Lorentz oscillators that represent interband transitions. Unlike the UT phase, a Lorentz oscillator is required to fit the hump in σ_1 about 400 cm^{-1} in the CT phase in $\text{Ca}_{0.85}\text{Pr}_{0.15}\text{Fe}_2\text{As}_2$ as shown in Fig. A5 in Appendix C. According to Ref. [111], at zone center, the β band shifts down below Fermi energy across CT phase transition, leaving the α band still above the Fermi energy. The gap between the top of the two bands is about 30 meV (240 cm^{-1}) at the Γ point and the gap increases at larger wavevectors. So we may conclude that the hump in conductivity 400 cm^{-1} is from the interband transition between α and β band in the CT phase. The optical transition between the weakly hybridized Fe-d and As-p band to an unoccupied Fe-d band [136] is centered about 7000 cm^{-1} for Pr-doped CaFe_2As_2 (see Fig. 4.1(b)). The center frequency of this interband transition after structure collapse increases by about 500 cm^{-1} which we also attribute primarily to the downward shift of the β band.

4.4 Summary

In summary, we have obtained the frequency and temperature dependent *ab*-plane optical conductivity of crystals of rare-earth-doped CaFe_2As_2 . For UT La-doped and Pr-doped CaFe_2As_2 , the scattering rate reveals a dominant scattering

channel quadratic in temperature and frequency. We also find saturation of the scattering rate above 200 K near the Mott-Ioffe-Regel limit in UT La-doped and Pr-doped CaFe_2As_2 . The spectral weight of free charge carriers in the UT phase decreases with increasing temperature in a broad temperature range and is recovered at an energy scale of ~ 0.5 eV which is much larger than the Fermi energy scale. Given that the phenomena we observe in rare-earth doped CaFe_2As_2 are similar to that seen in other correlated metals, we are forced to conclude that the dominant scattering mechanism is of electronic origin, and these materials are not canonical Fermi liquids. Below the CT phase transition in Pr-doped CaFe_2As_2 , we observe a decrease of the scattering rate due to weakening of electronic correlations, and a decrease in mobile carrier density which is consistent with the partial loss of the hole Fermi surfaces.

CHAPTER 5

Strong electron-boson interaction in superconducting $\text{BaFe}_{1.9}\text{Pt}_{0.1}\text{As}_2$

5.1 Introduction

Nearly half-a-century after the experimental discovery of superconductivity, Bardeen, Cooper and Schrieffer (BCS) developed a model to explain this phenomenon [1]. Their model consisted of an electron gas with attractive interactions (mediated by phonons) that lead to the formation of electron pairs (or Cooper pairs) whose overlapping wavefunctions underlie the superconducting condensate. The BCS mechanism provides a microscopic description of weak-coupling superconductivity in conventional phonon-mediated superconductors. In the BCS theory, the ratio of the energy gap to T_c , $\Delta(T=0)/k_B T_c = 1.764$ and this has

been observed in a number of conventional phonon-mediated superconductors in the weak-coupling limit. For strong-coupling superconductors like lead (Pb) and mercury (Hg) in which the gap to T_c ratio is more than 2, Eliashberg [3] provided a more realistic model of the superconducting state that includes the retarded nature of the phonon induced interaction. Apart from the energy gap which is a complex quantity in the Eliashberg equations, a central parameter is the electron-phonon spectral density function (or Eliashberg function) $\alpha^2F(\omega)$, a quantitative measure of the electron-phonon coupling and the phonon density of states [137]. The agreement of the parameters in the self-consistent solutions of the Eliashberg equations, for example in Pb, with experimental results like phonon density of states from inelastic neutron scattering [138], electronic density of states from tunneling experiments [137], electronic heat capacity enhancement [137], and infrared absorption [139], provide strong evidence for the electron-phonon mechanism of superconductivity in conventional superconductors.

For the high-temperature iron-based superconductors, the mechanism of superconductivity has been debated for the past decade since their experimental discovery [67,140]. It has been argued that phonons alone cannot explain the high transition temperatures [67,140]. Spin and orbital fluctuations are currently the promising candidates for mediating the formation of Cooper pairs. Spin fluctuations

(corresponding to s_{\pm} pairing state) are the leading candidate [140]. An alternative theory suggests that moderate electron-phonon interaction due to Fe-ion oscillation (E_g phonon) can induce critical orbital fluctuations (corresponding to s_{++} pairing state), making orbital-fluctuation mediated high temperature superconductivity possible [141]. Regardless of the origin of the bosonic mode(s) that could induce superconductivity, the characteristic strong-coupling electron-boson interaction features should be detectable by spectroscopy methods in fully gapped iron pnictide superconductors.

Different experimental techniques have been used to study the pairing mechanism in the iron pnictide superconductors and have provided some evidence that collective spin fluctuations may be the bosons that mediate the formation of Cooper pairs. Inelastic neutron scattering studies on both electron- and hole-doped iron pnictides observe a spin resonance mode [57,142–144], which is similar to that seen in cuprates [145], indicating the importance of spin correlations. Scanning tunneling spectroscopy of hole (K) -doped BaFe_2As_2 [146] also observes a bosonic mode which is consistent with the spin resonance mode from inelastic neutron scattering experiments. Specific heat experiments on $\text{Ba}_{0.68}\text{K}_{0.32}\text{Fe}_2\text{As}_2$ single crystals [147] can be modeled within a framework of four-band Eliashberg approach using a spin-fluctuation coupling function whose center frequency also

matches the spin excitation resonance from inelastic neutron scattering experiments. Quasiparticle interference imaging techniques have identified antiferromagnetic spin fluctuations as the predominant electron-boson interactions in the LiFeAs superconductor [148].

Infrared spectroscopy is a powerful tool to study the energy gaps below T_c , the strong-coupling electron-boson features of superconductivity, and the interplay between energy gaps and the strong-coupling features. Previous infrared studies on iron-based superconductors focus on the occurrence of multiple gaps and fit the optical conductivity and/or reflectance with the Mattis-Bardeen framework within the weak-coupling BCS theory [73,74,149–153]. Since the larger gap(s) in the iron-based superconductors are in the strong-coupling limit, some researchers have turned towards the strong-coupling Eliashberg formalism. The strong-coupling methods were originally developed for strong electron-phonon interactions but they are widely used to describe the coupling of electrons to any bosonic spectrum. Unlike the cuprates [154,155], the multiple-gap nature of the iron-based superconductors is an obstacle for using inversion techniques to extract the electron-boson spectral density. In a few studies, researchers have tried to obtain the electron-boson spectral density from the scattering rate in the normal state [156–159]. This presents a problem in that one cannot check self-consistency

of the Eliashberg equations in the superconducting state. One recent approach [160] provides a method to find the electron-boson interaction both in the normal and superconducting states from the infrared scattering rate (or self-energy). However, this work does not check if the electron-boson spectral density function is self-consistent with the energy gap by solving the full Eliashberg equations. Charnukha *et al* [75] pointed out the limitation of the Mattis-Bardeen theory and have used a multiband Eliashberg theory to fit the optical conductivity to support the spin-fluctuation mechanism. The fits only qualitatively describe the real part of the optical conductivity in the superconducting state. To summarize, previous infrared experiments have not directly observed the electron-boson coupling features expected in the absorption spectra of strong-coupling, fully-gapped iron based superconductors. Such features are expected to occur because they have been seen in the infrared absorption data in lead (Pb), a fully-gapped, phonon-mediated strong-coupling superconductor [139].

Previous spectroscopy and thermal transport experiments on high quality single crystals of superconducting $\text{BaFe}_{1.9}\text{Pt}_{0.1}\text{As}_2$ reveal two isotropic gaps, one 2-3 meV and the other 5-7 meV [161]. Here we report infrared spectroscopy data on superconducting $\text{BaFe}_{1.9}\text{Pt}_{0.1}\text{As}_2$ that is consistent with multi-band superconductivity with isotropic gaps. The important new finding is that we observe

strong-coupling electron-boson interaction features in the infrared absorption spectra. The frequency dependent infrared absorption (A) is simply $A = 1 - R$ where the frequency dependent infrared reflectance (R) is directly measured in the experiments. We identify a bosonic mode centered at 5.1 ± 0.6 meV (41 ± 5 cm⁻¹) that provides the pairing glue in superconducting BaFe_{1.9}Pt_{0.1}As₂. We employ two theoretical models to quantitatively describe our absorption spectra. The first model is the Allen formalism based on the scattering rate (or optical self-energy) method which includes the contribution of the electron-boson spectral density function [160,162]. After obtaining the electron-boson spectral density function from the Allen formalism, we solve the full isotropic Eliashberg equations to check the self-consistency of the electron-boson coupling spectrum with the largest energy gap and T_c . The second model starts from solving the full isotropic Eliashberg equations by assuming a reasonable electron-boson spectral density function (Eliashberg function). Then complex far-infrared optical conductivity in both the normal and superconducting states can be calculated which includes the Holstein mechanism induced by strong electron-boson coupling [163]. Absorption spectra can then be obtained and compared to the experimental data. The second formalism for modeling the spectra of strong-coupling superconductors is derived by Zimmermann *et al.*, and we call it Zimmermann formalism.

5.2 Sample and measurements

Single crystals of $\text{BaFe}_{1.9}\text{Pt}_{0.1}\text{As}_2$ were grown using FeAs self-flux method, which is described in Ref. [161,164] along with x-ray, transport, magnetic and thermodynamic measurements. The *dc* resistivity data shows the onset of superconductivity at $T_c = 23$ K [161,164]. The resistivity data of $\text{BaFe}_{1.9}\text{Pt}_{0.1}\text{As}_2$ is shown in Fig. 5.1. The sample is metallic at higher temperature and becomes superconducting with the onset of the transition at $T_c = 23$ K. Magnetic susceptibility measurements show bulk superconductivity with full volume fraction [161,164]. BaFe_2As_2 doped with 5-d transition metal element Pt^{2+} , is believed to be electron-doped, since Pt^{2+} doping shares similarity to Ni^{2+} doping, which introduces more d- electrons than Fe^{2+} [164–166]. Besides, negative Hall coefficients provide evidence of charge transport dominated by electron carriers [167].

A high quality large single crystal with a freshly cleaved shiny flat surface of 5×4 mm² is measured in this work. The large shiny surface is important for specular reflectance and ensures good signal-to-noise ratio in our measurements.

The *ab*-plane reflectance at various temperatures from 300 K to 5 K was obtained in a cryogenic setup with a Bruker Vertex 80v Fourier transform infrared (FTIR) spectrometer in the frequency range $20 \text{ cm}^{-1} - 8000 \text{ cm}^{-1}$ using the

technique of *in situ* gold evaporation. Cryogenic ellipsometry was performed in a homebuilt quartz-tube vacuum chamber with a Woollam variable-angle spectroscopic ellipsometer in the energy range 0.6 eV – 6 eV. Further details of the cryogenic infrared reflectance and cryogenic ellipsometry set-ups are discussed in Chapter 3 and Ref. [90].

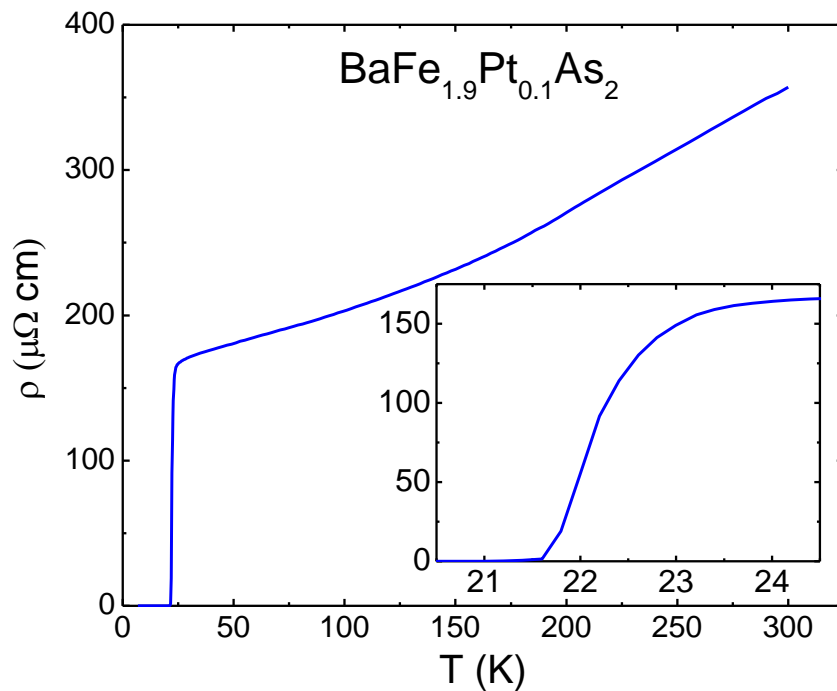


FIG. 5.1. The resistivity of $\text{BaFe}_{1.9}\text{Pt}_{0.1}\text{As}_2$, with on-set $T_c \sim 23$ K. Inset: zoom in at temperatures near T_c .

5.3 Results and discussions

5.3.1 Reflectance, optical conductivity and normalized absorption

The *ab*-plane infrared reflectance of a $\text{BaFe}_{1.9}\text{Pt}_{0.1}\text{As}_2$ crystal is shown in Fig. 5.2. In the normal state at $T = 25$ K, $\text{BaFe}_{1.9}\text{Pt}_{0.1}\text{As}_2$ shows metallic behavior like many other iron-based materials [75,90,151]. At $T = 5$ K, well below T_c , superconductivity is observed directly from perfect reflectance at frequencies below 31.5 cm^{-1} . The data are consistent with a fully gapped (nodeless) superconductor close to the dirty limit [73,74,151,168,169].

Fig. 5.3 is the real part optical conductivity σ_1 with temperature dependence

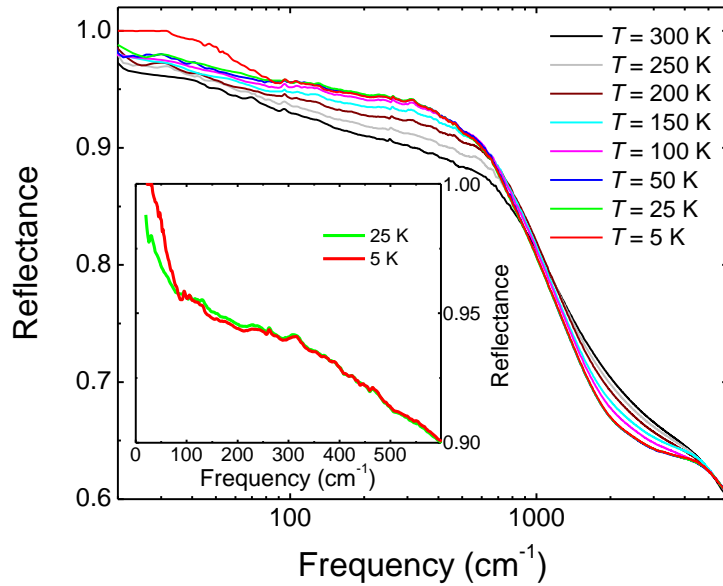


FIG. 5.2. Infrared reflectance of $\text{BaFe}_{1.9}\text{Pt}_{0.1}\text{As}_2$ at various temperatures. Inset: comparison of far infrared reflectance far below T_c and just above T_c ($T_c = 23$ K).

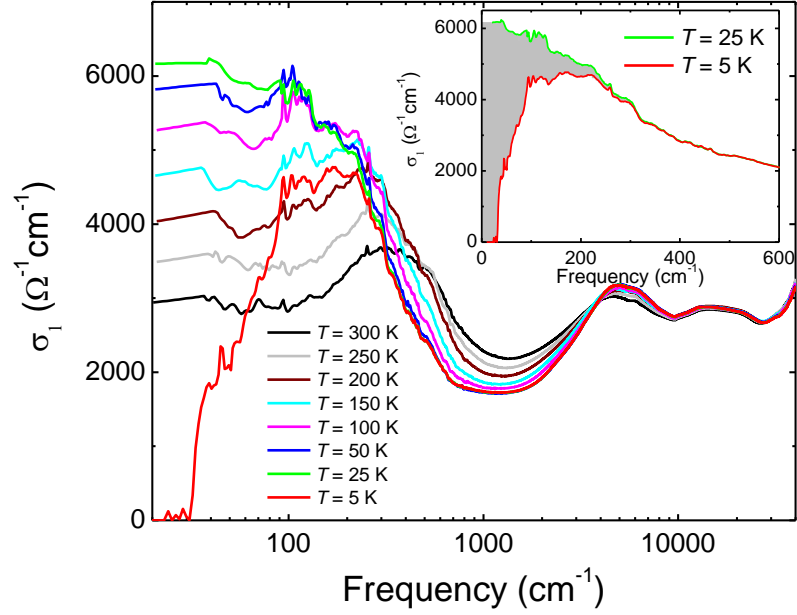


FIG. 5.3. The real part of the ab-plane optical conductivity σ_1 is plotted as a function of frequency at different temperatures. Inset: the “missing area” between normal and superconducting state real conductivity calculated from the Ferrell-Glover-Tinkham sum rule is shown as shade area.

obtained from Kramers-Kronig transformation constrained by cryogenic ellipsometry data, similar to procedure described in chapter 4. At $T = 5 \text{ K}$, the real part of the conductivity is zero below frequency 31.5 cm^{-1} , corresponding to the smallest gap. At higher frequencies, there is a sharp increase of the conductivity just above the gap and subsequently the conductivity reaches a maximum, which is a clear indication of superconductivity in the dirty limit. Indeed, the scattering rate of normal state (25 K) 370 cm^{-1} , which is the width of Drude peak, is much larger than the energy gap ($1/2\pi\tau \gg 2\Delta$) [84], indicating the superconductivity is in the dirty limit. The inset in Fig. 5.3 clearly shows the “missing” spectral weight

between normal state and superconducting state which is condensed into the delta function at zero frequency in the superconducting state. The missing area of spectral weight is proportional to the superfluid density, $\omega_{ps}^2 = \int_0^{\omega_c} d\omega [\sigma_1(\omega, T = 25K) - \sigma_1(\omega, T = 5K)] = 1.9 \times 10^7 \text{ cm}^{-2}$, which is consistent with low frequency limit $\omega_{ps}^2 = -\omega^2 \epsilon_1(\omega \rightarrow 0)$ [151].

The absorption in the superconducting state $A_S(T)$ for $T < T_c$ is obtained from the equation $A_S(T) = 1 - R_S(T)$, where $R_S(T)$ is the reflectance in the superconducting state. The normal state absorption $A_N(T = 25 \text{ K})$ is obtained from $A_N(25 \text{ K}) = 1 - R_N(25 \text{ K})$ where $R_N(25 \text{ K})$ is the reflectance in the normal state at $T = 25 \text{ K}$. The ratio $A_S(5 \text{ K})/A_N(25 \text{ K})$ is the absorption in the superconducting state at $T = 5 \text{ K}$ normalized to the absorption in the normal state at $T = 25 \text{ K}$ and is plotted as a function of frequency in Fig. 5.4. We plot this way to show strong features. There are clear features at 80–200 cm^{-1} which are larger than the error bars (see Fig. 5.4). The sharp peak at 87 cm^{-1} is due to the largest gap. Above this gap feature, we observe a ‘valley-peak-valley’ structure, which is not obvious from unnormalized reflectance or optical conductivity in either superconducting state or normal state. When we compare our normalized infrared absorption data of $\text{BaFe}_{1.9}\text{Pt}_{0.1}\text{As}_2$ to the normalized infrared absorption data of the well-known conventional strong-coupling superconductor lead (Pb) (see inset of Fig. 5.4, data

taken from Ref. [139,162]), we see they are remarkably similar. In Pb, acoustic phonons are the bosonic modes which mediate the formation of Cooper pairs, and the valleys in the absorption data are due to the peaks in the phonon density of states shifted by 2Δ . Hence, the valleys in the absorption data of $\text{BaFe}_{1.9}\text{Pt}_{0.1}\text{As}_2$ roughly correspond to peaks in the density of states of bosonic modes shifted by the largest gap $2\Delta_3$.

In the following sections 5.3.2 and 5.3.3, two different formalisms have been applied to model the normalized absorption of $\text{BaFe}_{1.9}\text{Pt}_{0.1}\text{As}_2$, in order to quantitatively determine the bosonic mode coupled to the electrons.

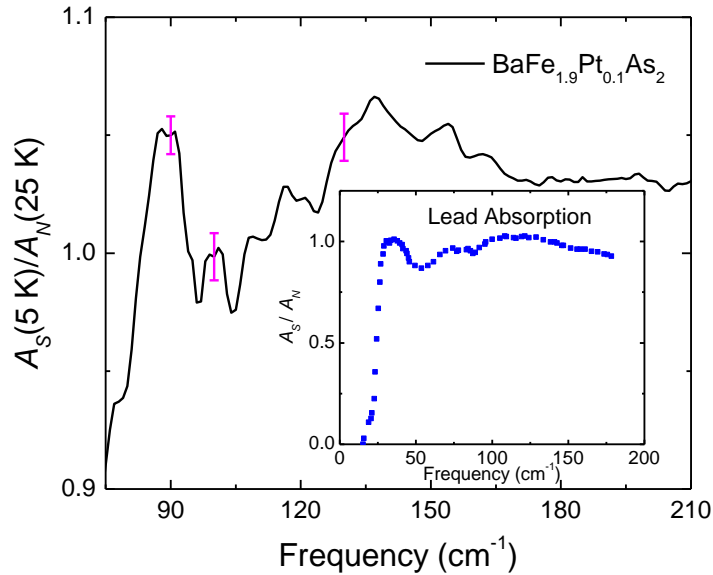


FIG. 5.4. Infrared absorption in superconducting state (5 K) normalized to infrared absorption in normal state (25 K). It clearly shows a ‘valley-peak-valley’ region ($\sim 80\text{--}200\text{ cm}^{-1}$) in the normalized absorption spectrum. Error bars at representative frequencies are also shown. Inset: normalized infrared absorption of Pb.

5.3.2 Modeling with Allen's formalism

Following Ref. [160], imaginary part of optical self-energy is:

$$\Sigma_2^{op}(\omega, T) = -\frac{1}{2} \left[\int_0^\infty d\Omega I^2 \chi(\Omega, T) K(\omega, \Omega, T) + \frac{1}{\tau_{imp}^{op}(\omega)} \right] \quad (5.1)$$

where $I^2 \chi$ is the electron-boson spectral density function, $K(\omega, \Omega, T)$ is the kernel of Allen's integral equation, and $1/\tau_{imp}^{op}(\omega)$ is the impurity scattering rate [160]. Eq. 5.1 is applicable to both the normal phase and the superconducting phase but $K(\omega, \Omega, T)$ and $1/\tau_{imp}^{op}(\omega)$ are different for the two phases.

$$K(\omega, \Omega, T) = \frac{\pi}{\omega} \left[2\omega \coth\left(\frac{\Omega}{2T}\right) - (\omega + \Omega) \coth\left(\frac{\omega + \Omega}{2T}\right) + (\omega - \Omega) \coth\left(\frac{\omega - \Omega}{2T}\right) \right]$$

(for normal state)

$$= \frac{2\pi}{\omega} (\omega - \Omega) \theta(\omega - 2\Delta - \Omega) \times E\left(\frac{\sqrt{(\omega - \Omega)^2 - (2\Delta)^2}}{\omega - \Omega}\right)$$

(for superconducting state)

(5.2)

where $\theta(x)$ represents the Heaviside step function, and $E(x)$ represents the complete elliptic integral of the second kind. The impurity scattering rate:

$$1/\tau_{imp}^{op}(\omega) = 370 \text{ cm}^{-1} \text{ (for normal state 25 K)}$$

$$= 370 \text{ cm}^{-1} \times E\left(\frac{\sqrt{\omega^2 - (2\Delta)^2}}{\omega}\right)$$

(for superconducting state 5K)

(5.3)

Then the real part can be obtained by Kramers-Kronig transformation:

$$\Sigma_1^{op}(\omega) = -\frac{2\omega}{\pi} P \int_0^\infty d\Omega \frac{\Sigma_2^{op}(\omega)}{\Omega^2 - \omega^2} \quad (5.4)$$

The complex optical conductivity for one channel is:

$$\tilde{\sigma}(\omega) = \frac{\omega_p^2}{8\pi i} \frac{1}{\tilde{\Sigma}^{op}(\omega) - \omega/2} \quad (5.5)$$

where $\tilde{\Sigma}^{op}(\omega) = \Sigma_1^{op}(\omega) + i\Sigma_2^{op}(\omega, T)$. The total conductivity is the sum of different channels (here we have 3 channels due to the multi-band nature of this material):

$$\tilde{\sigma}_{total}(\omega) = \tilde{\sigma}_{ch1}(\omega) + \tilde{\sigma}_{ch2}(\omega) + \tilde{\sigma}_{ch3}(\omega) \quad (5.6)$$

We then add the contributions of the evident interband transitions from the data at higher frequencies to the low-frequency conductivity calculated from the model.

The parameters in the model are as follows: the normal state impurity scattering rate is a constant 370 cm^{-1} , the normal state plasma frequency $\omega_p = 1.45 \pm 0.2 \text{ eV}$, and the three energy gaps in the superconducting state are discussed below. Our best fit and the corresponding electron-boson density function $I^2\chi$ are shown in Fig. 5.5(a), (b). The smallest gap $2\Delta_1 = 31.5 \text{ cm}^{-1}$ corresponds to the onset of absorption and the largest gap $2\Delta_3 = 87 \text{ cm}^{-1}$ corresponds to the peak at 87 cm^{-1} in the normalized absorption data. A third gap with energy $2\Delta_2 = 58 \text{ cm}^{-1}$ is required to fit the shoulder around 60 cm^{-1} . However, Δ_2 is associated with the Fermi surface with a small spectral weight (10% of the square of the normal state plasma frequency). The gaps Δ_1 and Δ_3 are associated with Fermi surfaces that respectively represent 55% and 35% of the square of the normal state plasma frequency. The smallest gap Δ_1 that we observe in $\text{BaFe}_{1.9}\text{Pt}_{0.1}\text{As}_2$ is consistent with four different experiments reported in Ref. [161].

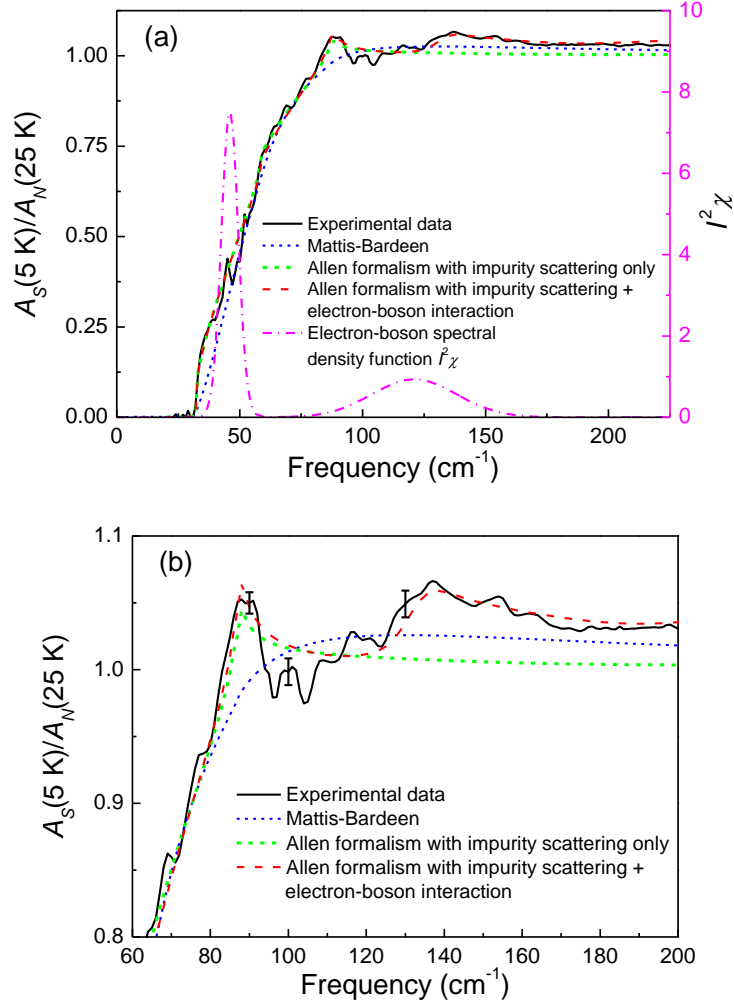


FIG. 5.5. Infrared absorption in superconducting state (5 K) normalized to infrared absorption in normal state (25 K), and the fits to different models. (a) The following three models are used while keeping the same energy gap magnitudes: weak-coupling multi-gap Mottis-Bardeen theory, the multi-band Allen formalism (optical self-energy method) with only impurity scattering, and the multi-band Allen formalism with both electron-boson interaction and impurity scattering. The electron-boson spectral density function $I^2\chi$ consists of one sharp large peak and one smaller broad peak. (b) Zoomed in view of the ‘valley-peak-valley’ region ($\sim 90 - 200 \text{ cm}^{-1}$) in the normalized absorption spectrum shown in (a). Error bars at representative frequencies are also shown in (b).

The existence of a larger gap has been previously suggested by point contact spectroscopy experiments [161]. The observation of multiple gaps is consistent

with several earlier studies of other types of iron-based superconductors [75,81,151]. For electron-doped Ba-122 system, ARPES data shows that a small gap occurs on two electron pockets γ and δ , while a larger gap is on the outer hole pocket (β band) [76]. The inner hole pockets are hard to observe [19,76] due to their small spectral weight. Hence Δ_2 could be the gap on the inner hole pockets.

The ratio $2\Delta_3/k_B T_c = 5.44$ is clearly in the strong-coupling limit compared to the BCS weak-coupling value of 3.53. The ratios of the other two gaps to T_c are either smaller than ($2\Delta_1/k_B T_c = 1.97$) or close to ($2\Delta_2/k_B T_c = 3.63$) the BCS weak-coupling value. This justifies using the electron-boson spectral density function only in the conductivity channel associated with the largest energy gap Δ_3 . In order to fit the two valleys in the experimental normalized absorption spectrum, the electron-boson spectral density function in the superconducting state consists of two Gaussian peaks: one large and sharp mode centered at frequency $\Omega_1 = 46 \text{ cm}^{-1}$ and one broad, weaker mode centered at frequency $\Omega_2 = 121 \text{ cm}^{-1}$. These two peaks approximately correspond to the two valleys respectively centered at frequencies 115 cm^{-1} ($\approx \Omega_1 + 2\Delta_3$) and 180 cm^{-1} ($\approx \Omega_2 + 2\Delta_3$) in the calculated normalized absorption spectrum. In order to obtain the correct absolute value of normalized absorption, only the weak, broad peak is necessary in the normal state.

Here we discuss the calculated normalized absorption using three methods while keeping the same energy gaps: the multi-band Allen formalism (optical self-energy method) including both electron-boson interaction and impurity scattering $1/\tau_{imp}^{op}(\omega)$; the multi-band Allen formalism with only impurity scattering; and multi-band Mattis-Bardeen theory. The model fits are compared in Fig. 5.5. Neither multiple band Mattis-Bardeen formalism [170] nor the optical self-energy method with only impurity scattering capture the “valley-peak-valley” features in the normalized absorption data above the peak feature of the largest gap. Introducing electron-boson interaction to the optical self-energy is required to fit the ‘valley-peak-valley’ features between 80 cm^{-1} and 200 cm^{-1} .

The model results for the complex optical conductivity are shown in Fig. 5.6. In Fig. 5.6, we also compare three different models: multiple band Mattis-Bardeen theory, optical self-energy model which only contains impurity scattering, and optical self-energy which includes both electron-boson interaction and impurity scattering rate. It is clear that Mattis-Bardeen theory doesn’t give us a good low frequency fit ($<100 \text{ cm}^{-1}$) for σ_1 and misses the fine features in the data. The model for optical self-energy method which only contains impurity scattering is not a good description for σ_2 and there is a clear discrepancy at all frequencies. While the model for optical self-energy method which includes both electron-boson

interaction and impurity scattering rate captures the features in the data at low frequencies very well (though there is some discrepancy with σ_1 data at frequencies higher than 100 cm^{-1}). The average error between the model and the data is around 10%. The corresponding model results for reflectance and absorption are shown in Fig. 5.7, and provide a good quantitative fit.

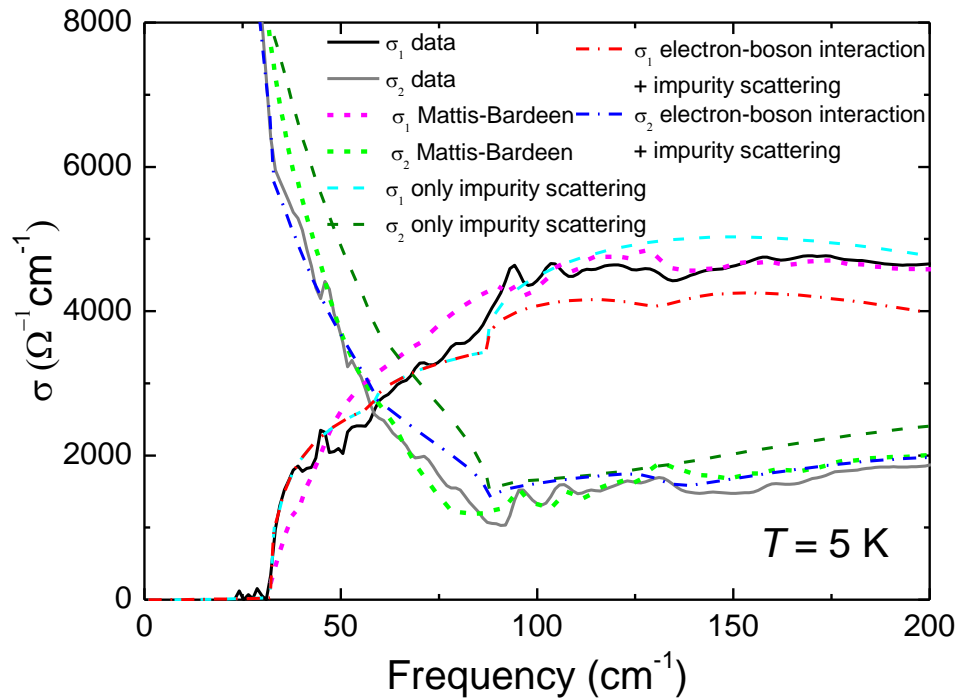


FIG 5.6. Model fits for low frequency complex optical conductivity in the superconducting state (5 K). Comparing fitting results of superconducting complex optical conductivity of Mattis-Bardeen theory, optical self-energy method which only contains impurity scattering and optical self-energy method which includes both electron-boson interaction and impurity scattering rate. The fitting of optical self-energy method which includes both electron-boson interaction and impurity scattering rate are clearly better than the other two fittings (both qualitatively and quantitatively).

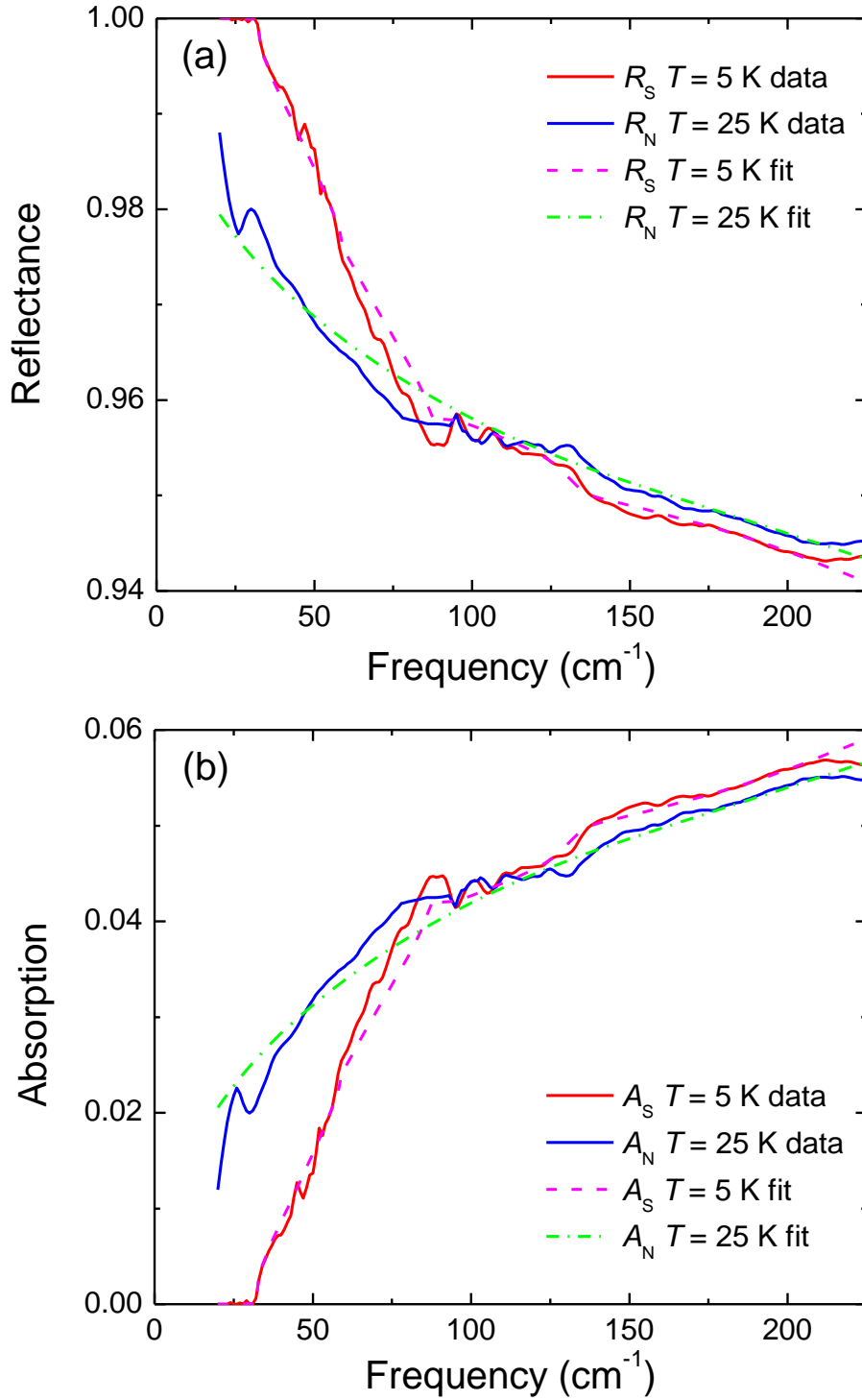


FIG. 5.7 Model fits of low frequency (a) reflectance and (b) absorption in the superconducting state (5 K) and the normal state (25 K).

Since the Allen formalism is expected to provide only an approximate quantitative description of strong-coupling superconductors [160,162], we take the important step to check the self-consistency of the energy gap, transition temperature, and the electron-boson spectral density function $I^2\chi(\Omega)$ by solving the full Eliashberg equations. Here we use an isotropic energy gap consistent with experiments [161] and the effective Coulomb pseudo-potential $\mu^* = 0.1$ [171]. The Eliashberg equations are solved using EPW4.2 as described in the Ref. [171] and Appendix D. EPW is an open source software which can be used to compute electron–phonon (boson) couplings and related properties in solids accurately and efficiently. We use EPW 4.2 to solve electron-phonon coupling strengths, superconducting gaps and renormalization function within the Migdal–Eliashberg theory. Renormalization function $Z(\omega)$ and the superconducting gap $\Delta(\omega)$ are first solved on imaginary energy axis and then an analytic continuation is performed to the real axis. The solutions of Eliashberg equations are shown in Fig. 5.8. The solved gap function is $2\Delta(\omega=0) = 85 \text{ cm}^{-1}$, which is almost identical to the largest gap $2\Delta_3$. The lower limit of T_c can be estimated from McMillan’s formula [172]:

$$T_{c,\min} = \frac{\langle\omega\rangle}{1.20} \exp[-1.04(1+\lambda)/(\lambda - \mu^* - 0.62\lambda\mu^*)] \quad (5.7)$$

where μ^* assumed to be 0.1, and

$$\lambda = 2 \int_0^\infty d\Omega I^2\chi(\Omega) / \Omega \quad (5.8)$$

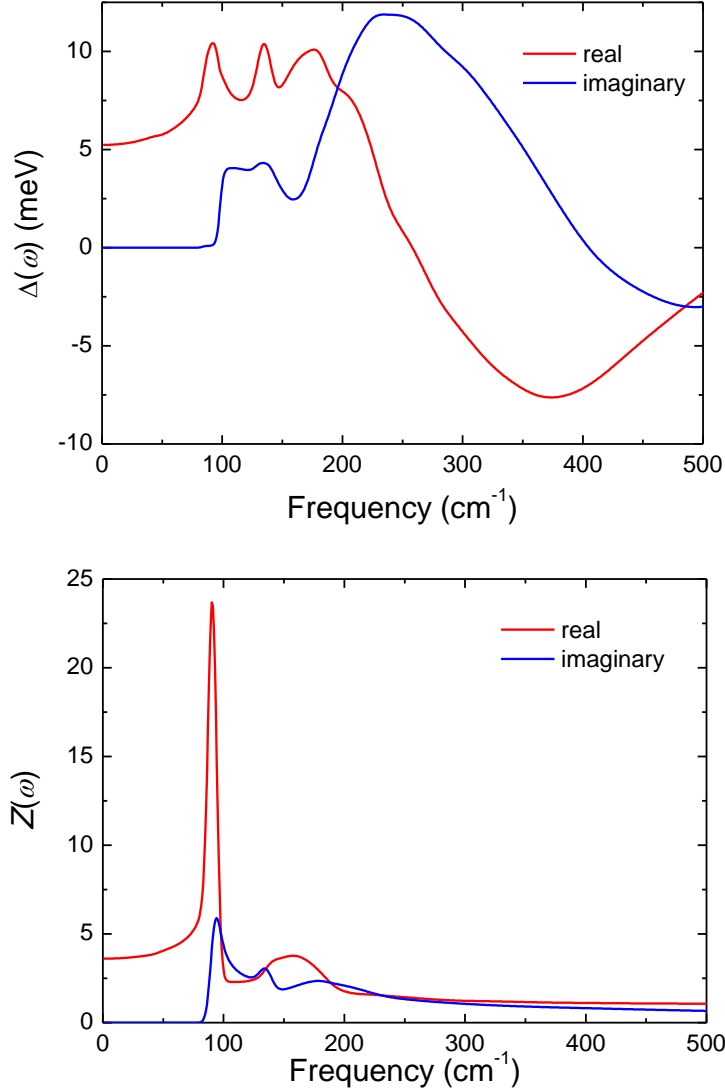


FIG. 5.8 Complex superconducting gap $\Delta(\omega)$ and the renormalization function $Z(\omega)$ obtained by solving Eliashberg equations.

$$\langle \omega \rangle = \frac{\int_0^\infty d\Omega I^2 \chi(\Omega)}{\int_0^\infty d\Omega I^2 \chi(\Omega) / \Omega} \quad (5.9)$$

and we obtain $T_{c,\min} = 17.1$ K. An upper limit of T_c is given by the generalized McMillan equation [160,172]:

$$k_B T_{c,\max} \cong 1.13 \hbar \omega_{ln} \exp[-(1 + \lambda)/\lambda] \quad (5.10)$$

where

$$\omega_{ln} = \exp\left[(2/\lambda) \int_0^\infty d\Omega \ln \Omega I^2 \chi(\Omega) / \Omega\right] \quad (5.11)$$

and this gives $T_{c,max} = 24.6$ K. The estimates of T_c are consistent with the experimental transition temperature of 23 K.

5.3.3 Modeling with Zimmermann's approach

Since the largest gap is in the strong-coupling limit, we apply the formalism of Zimmermann *et al.* [163] for calculating the optical conductivity in the strong-coupling regime. The temperature dependent complex conductivity in the superconducting state takes following form [163,173]:

$$\begin{aligned} \sigma(\omega, T) = & \frac{\omega_p^2}{16\pi^3\omega} \int_{-\infty}^{+\infty} d\varepsilon \left\{ \tanh\left(\frac{\varepsilon}{2k_B T}\right) M(\varepsilon, \omega) [g(\varepsilon)g(\varepsilon + \omega) + h(\varepsilon)h(\varepsilon + \omega) + \pi^2] - \right. \\ & \tanh\left(\frac{\varepsilon + \omega}{2k_B T}\right) M^*(\varepsilon, \omega) [g^*(\varepsilon)g^*(\varepsilon + \omega) + h^*(\varepsilon)h^*(\varepsilon + \omega) + \pi^2] + \left[\tanh\left(\frac{\varepsilon + \omega}{2k_B T}\right) - \right. \\ & \left. \left. \tanh\left(\frac{\varepsilon}{2k_B T}\right) \right] L(\varepsilon, \omega) [g^*(\varepsilon)g(\varepsilon + \omega) + h^*(\varepsilon)h(\varepsilon + \omega) + \pi^2] \right\} \quad (5.12) \end{aligned}$$

where ω_p is plasma frequency and

$$g(\varepsilon) = \frac{-\pi\tilde{\varepsilon}(\varepsilon)}{\sqrt{\tilde{\Delta}^2(\varepsilon) - \tilde{\varepsilon}^2(\varepsilon)}} \quad (5.13)$$

$$h(\varepsilon) = \frac{-\pi\tilde{\Delta}(\varepsilon)}{\sqrt{\tilde{\Delta}^2(\varepsilon) - \tilde{\varepsilon}^2(\varepsilon)}} \quad (5.14)$$

$$M(\varepsilon, \omega) = \left[\sqrt{\tilde{\Delta}^2(\varepsilon + \omega) - \tilde{\varepsilon}^2(\varepsilon + \omega)} + \sqrt{\tilde{\Delta}^2(\varepsilon) - \tilde{\varepsilon}^2(\varepsilon)} + 1/\tau \right]^{-1} \quad (5.15)$$

$$L(\varepsilon, \omega) = \left[\sqrt{\tilde{\Delta}^2(\varepsilon + \omega) - \tilde{\varepsilon}^2(\varepsilon + \omega)} + \sqrt{\tilde{\Delta}^{*2}(\varepsilon) - \tilde{\varepsilon}^{*2}(\varepsilon)} + 1/\tau \right]^{-1} \quad (5.16)$$

where $1/\tau$ is the impurity scattering rate. The quantities $\tilde{\Delta}$ and $\tilde{\epsilon}$ depend on energy ϵ , $\tilde{\epsilon}(\epsilon) = \epsilon Z(\epsilon)$ and $\tilde{\Delta} = Z(\epsilon)\Delta(\epsilon)$. And complex renormalization function $Z(\epsilon)$ and superconducting gap $\Delta(\epsilon)$ are obtained by solving the standard Eliashberg equations for isotropic systems at real energies. In eq. 5.12, since integral is implemented on the energy axis from negative infinity to positive infinity, extrapolations are needed to get negative energy dependence of $Z(\epsilon)$ and $\Delta(\epsilon)$. Note that the real part of both $Z(\epsilon)$ and $\Delta(\epsilon)$ are even functions, and the imaginary part of both $Z(\epsilon)$ and $\Delta(\epsilon)$ are odd functions.

For the normal state, the conductivity can be expressed as:

$$\sigma_N(\omega, T) = \frac{\omega_p^2}{8\pi\omega} \int_{-\infty}^{+\infty} d\epsilon \left[\tanh\left(\frac{\epsilon+\omega}{2k_B T}\right) - \tanh\left(\frac{\epsilon}{2k_B T}\right) \right] M_N(\epsilon, \omega) \quad (5.17)$$

where

$$M_N(\epsilon, \omega) = [-i\tilde{\epsilon}_N(\epsilon + \omega) + i\tilde{\epsilon}_N^*(\epsilon) + 1/\tau]^{-1} \quad (5.18)$$

$$\tilde{\epsilon}_N(\epsilon) = \epsilon + \int_{-\infty}^{+\infty} d\Omega \alpha^2 F(\Omega) \left[i\pi \coth\left(\frac{\Omega}{2k_B T}\right) - \Psi\left(\frac{1}{2} + i\frac{-\epsilon+\Omega}{2\pi k_B T}\right) + \Psi\left(\frac{1}{2} + i\frac{-\epsilon-\Omega}{2\pi k_B T}\right) \right] \quad (5.19)$$

where $\alpha^2 F(\Omega)$ is Eliashberg coupling function and $\Psi(x)$ is the digamma function. Similar to eq. 5.12, extrapolations needed to get negative energy dependent $\alpha^2 F(\Omega)$. Note that $\alpha^2 F(\Omega)$ is an odd function.

The parameters in the simulation are plasma frequency ω_p is 1.43 eV, and impurity scattering rate in the normal state is 370 cm^{-1} , and in the superconducting

state is 160 cm^{-1} . For weak-coupling channel Δ_1 and Δ_2 , we used Mattis-Bardeen theory. The spectral weight (square of the plasma frequency) ratio for the three conductivity channels for the best fit is the same as in Allen's formalism in 5.3.2, which is 55%, 10% and 35% for the gaps Δ_1 , Δ_2 and Δ_3 . The best fit and corresponding Eliashberg function are shown in Fig. 5.9.

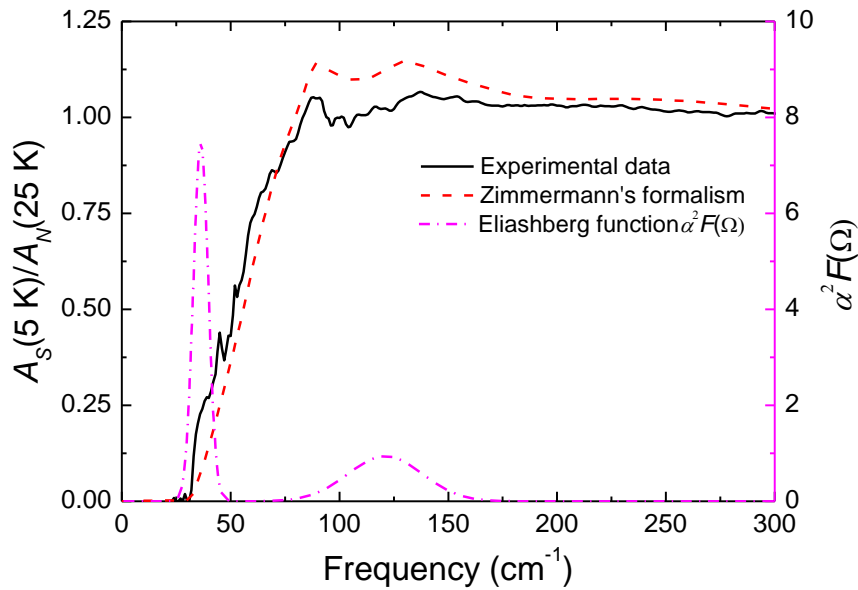


FIG. 5.9 Infrared absorption in superconducting state (5 K) normalized to infrared absorption in normal state (25 K), and the results from the model using Zimmermann's formalism. The Eliashberg function $\alpha^2 F(\Omega)$ consists of one sharp large peak and one smaller broad peak.

From Fig. 5.9, we see that the model has overall good quantitative agreement with the data. Importantly, it captures the 'valley-peak-valley' features between 80 cm^{-1} and 200 cm^{-1} and the frequencies of the peak and dip align very well with

those in the experimental data. Similar to Allen's method, the Eliashberg function in the superconducting state still consists of two peaks, one large sharp peak centered at 36.3 cm^{-1} (4.5 meV), and one small broad peak centered 121 cm^{-1} (15 meV). The coupling constant is $\lambda = 4.27$, and corresponding upper limit transition temperature T_c (similar in 5.3.2) is 20.5 K. Analogous with the results of Allen's formalism, in the normal state, only small broad peak is included in the Eliashberg function. Result of solving Eliashberg equations at 5 K gives gap function is $2\Delta(\omega=0) = 81.24 \text{ cm}^{-1}$, which is not very different from the result using Allen's formalism.

Through comparing the results of Allen's formalism and Zimmermann's formalism, we find that:

1. 'valley-peak-valley' features between 80 cm^{-1} and 200 cm^{-1} are a result of two peaks in the electron-boson spectral density function (Eliashberg function). And the large narrow peak Ω_1 is responsible for first valley, while the small broad peak Ω_2 is responsible for the weaker second valley.
2. low frequency large narrow peak Ω_1 only appears in the superconducting state. The center frequencies of Ω_1 from two methods are not exactly the same, giving us a range of Ω_1 in the $5.1 \pm 0.6 \text{ meV}$ ($41 \pm 5 \text{ cm}^{-1}$).
3. High frequency small broad peak Ω_2 appears both in the superconducting state

and the normal state. The center frequencies of Ω_2 is exactly the same in the two methods with 121 cm^{-1} (15 meV).

5.3.4 Origin of the two modes in the electron-boson spectral density function

Next we discuss the origin of the two peaks in the electron-boson spectral density function (Eliashberg function). The two promising candidates for bosons which mediate the formation of Cooper pairs are either spin fluctuations or orbital fluctuations (induced by Fe phonons). Spin resonance modes have been determined by inelastic neutron scattering experiments [57,142–144]. The spin resonance, which is observed only in the superconducting state in cuprates, heavy-fermion and iron-based superconductors, is generally considered a feedback effect from superconductivity. Despite some theoretical controversies, the resonance is viewed as a spin-exciton bound state in the particle-hole channel. The appearance of the resonance implies a sign change of superconducting gap(s) between either different patches of the Fermi surface or different Fermi pockets connected by a resonance mode at momentum q (see Ref. [174] and references therein). In our infrared experiments, the large sharp peak in the electron-boson

spectral density function of $\text{BaFe}_{1.9}\text{Pt}_{0.1}\text{As}_2$ is centered at 5.1 ± 0.6 meV (41 ± 5 cm^{-1}), with a full-width at half-maximum of 1 meV, and is only present in the superconducting state. We note that the spin resonance mode at 3D antiferromagnetic ordering wave vector $Q = (1, 0, -1)$ occurs in $\text{BaFe}_{1.9}\text{Ni}_{0.1}\text{As}_2$ (a superconductor with $T_c = 20$ K and similar to $\text{BaFe}_{1.9}\text{Pt}_{0.1}\text{As}_2$), with resonance energy $\hbar\omega_{\text{res}} = 7 \pm 0.5$ meV, and width $d = 1.9 \pm 0.7$ meV [142]. Inelastic neutron scattering experiments on $\text{BaFe}_{1.9}\text{Pt}_{0.1}\text{As}_2$ are not available at present. If the bosonic mode we have observed is due to spin fluctuations, then we expect that a spin resonance mode about 5 meV will be observed in future inelastic neutron scattering experiments. The center frequency of the bosonic mode in our infrared experiments is also not that different from the spin resonance mode of another electron-doped material $\text{Ba}(\text{Fe}_{1-x}\text{Co}_x)_2\text{As}_2$ which is $\sim 8 - 9$ meV [143,144]. Note that the bosonic mode observed in the optical response is the q averaged (all momenta in the Brillouin zone) local susceptibility. From the above discussion, we infer that the sharp peak at 5.1 ± 0.6 meV in the electron-boson spectral density function of $\text{BaFe}_{1.9}\text{Pt}_{0.1}\text{As}_2$ possibly represents the spin resonance in the superconducting state. The 5.1 meV peak cannot be due to phonons because it is lower in energy compared to the energy of the lowest peak in the phonon density of states in the parent compound BaFe_2As_2 [175,176]. Moreover, since phonons

are present in both the normal and superconducting states, the sharp peak cannot be due to phonons because it is only required in the superconducting state and not in the normal state for the best description of the data.

The broad, weak peak is centered at 15 meV (121 cm^{-1}), with a width of 5 meV, and is required in the models for both the superconducting and normal states. Inelastic X-ray scattering experiments have measured the lowest energy peak in the Fe phonon density of states centered at 13 meV, with width approximately 5 meV. The phonon density of states are nearly temperature independent [177]. Phonons are likely the origin of the weak, broad mode. Actually, the position and the width of the broad peak is also very similar to the prediction of the resonance peak of s_{++} wave pairing state [178]. Possible explanations are that the weak, broad mode is either due to electron-phonon interaction or due to phonon induced orbital fluctuations. Note that the total electron-boson coupling constant $\lambda = 3.5\text{--}4.3$ contains a significant contribution from the sharp peak of 2.8–3.6, and a minor contribution from the broad peak of only 0.7. If the sharp peak in the Eliashberg function is due to spin fluctuations, this means spin-fluctuations play the dominant role in superconductivity in $\text{BaFe}_{1.9}\text{Pt}_{0.1}\text{As}_2$. It would also support the presence of a predominant s_{\pm} gap in superconducting $\text{BaFe}_{1.9}\text{Pt}_{0.1}\text{As}_2$ [67].

5.3.5 Temperature dependent normalized absorption and superconducting gaps

Finally, we study the temperature dependence of the normalized absorption spectra. The absorption spectra in the superconducting state at $T = 5$ K, 10 K, 15 K, and 20 K, are normalized to the normal state absorption data ($T = 25$ K) and plotted in Fig. 5.10(a). It is clear that the amplitude of the strong-coupling features due to electron-boson interaction decreases when temperature increases toward T_c . However, there is little frequency dependence of these features for temperatures at and below 15 K. At $T = 20$ K, still below T_c , the strong-coupling features weaken further and move to lower frequencies. This may be caused by the reduction of energy gap $\Delta_3(T)$ and a downward shift in center frequency Ω_1 of the bosonic peak as the temperature approaches T_c from below. The Allen formalism for the superconducting state is meant for $T = 0$ K and works well for temperatures well below T_c . We cannot quantitatively model the temperature dependence of the bosonic modes with the Allen formalism because the Allen formalism for the superconducting state at higher temperatures does not exist and will need to be developed. We first attempt to follow the temperature dependence of the energy gaps using alternative means based on the Mattis-Bardeen theory. The temperature dependent energy gap $2\Delta_3(T)$ is estimated directly from the nor-

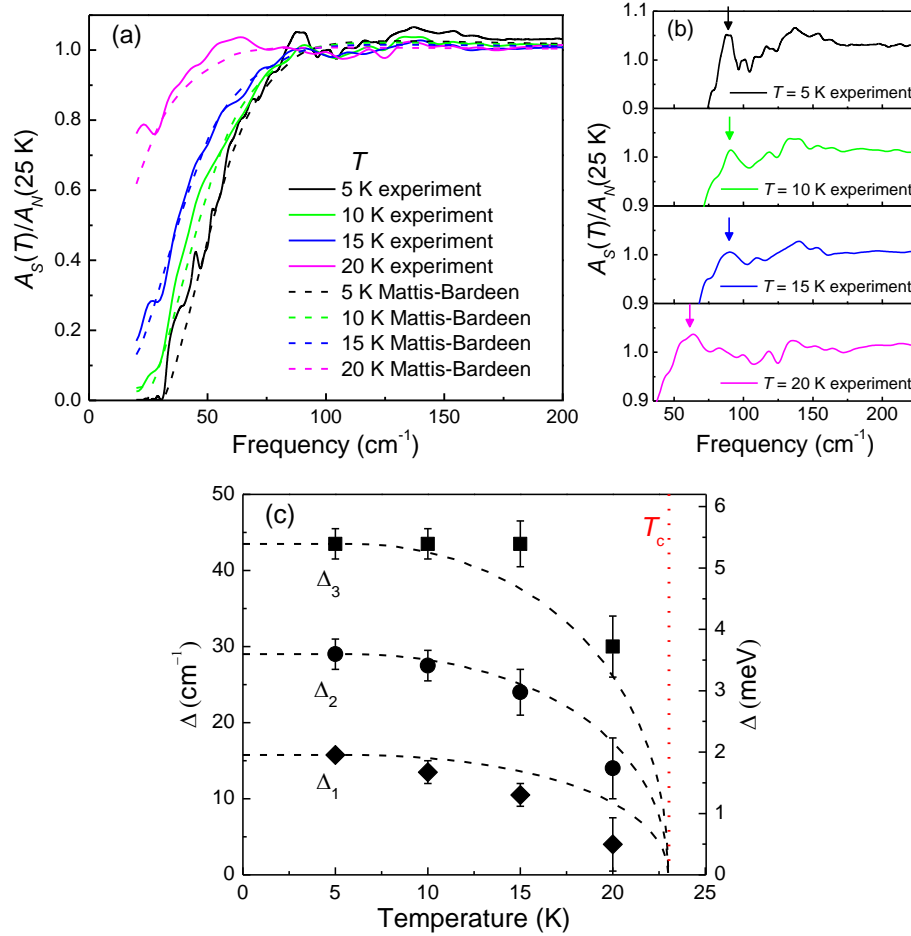


FIG. 5.10. (a) Solid lines are temperature dependent infrared absorption in the superconducting state normalized to infrared absorption in the normal state at $T = 25\text{ K}$. Dashed lines are Mattis-Bardeen fits to the normalized infrared absorption data (b) Zoomed in view of the spectra showing the peak associated with the largest gap $2\Delta_3$ and the “valley-peak-valley” strong-coupling features at different temperatures in the superconducting state. Arrows indicate the frequency of the first prominent peak in the normalized absorption spectrum due to the energy gap $2\Delta_3$ in the presence of impurity scattering. (c) Plot of the temperature dependence of the three energy gaps (filled symbols). The dashed lines are the BCS prediction of the temperature dependence of the energy gaps with Δ_1 , Δ_2 and Δ_3 as 15.75 cm^{-1} , 29 cm^{-1} and 43.5 cm^{-1} respectively at $T = 0\text{ K}$. The vertical dotted line represents $T_c = 23\text{ K}$.

malized absorption because it corresponds to the first prominent peak position (shown by arrows in Fig. 5.10(b)) and is plotted in Fig. 5.10(c). The temperature

dependence of Δ_1 and Δ_2 cannot be obtained directly from the data. However, since the ratio $2\Delta/k_B T_c$ for the smaller two gaps shows they are in the weak-coupling regime, we have modeled the normalized absorption using three-band Mattis-Bardeen formalism. The results are shown in Fig. 5.10(c). The largest and smallest gaps appear to deviate from the BCS prediction close to T_c .

Next, we attempt to fit the temperature dependent normalized absorption using Zimmermann's formalism for the largest gap, while keeping the two smaller gaps in the weak-coupling regime using Mattis-Bardeen theory. In the modeling, we use temperature dependent bosonic mode following temperature dependent spin resonance experimental result. As Ref. [56] shows, the resonance frequency follows the similar functional dependence of energy gap. Temperature dependent complex renormalization function $Z(\varepsilon)$ and superconducting gap $\Delta(\varepsilon)$ are obtained by solving the standard Eliashberg equations for isotropic systems at real energies, then the Zimmermann's formalism is applied in the largest energy gap. The simulation results are shown in the Fig. 5.11. The theoretical model captures the temperature-dependent trend of the 'valley-peak-valley' features well. At temperature $T = 10$ K and 15 K, the 'valley-peak-valley' features become weaker at higher temperatures compared to $T = 5$ K data, while there is little frequency dependence. At $T = 20$ K, a temperature close to T_c , the 'valley-peak-valley'

features are nearly washed out, and the frequency of the peak due to the largest gap and bosonic mode clearly shifts down (shown in Fig. 5.12) and aligns well the experimental data.

Temperature dependent energy gaps and bosonic mode in the model are shown in Fig. 5.12. There are larger error bars at higher temperature due to the larger uncertainty solution of the EPW software while temperature is close to T_c .

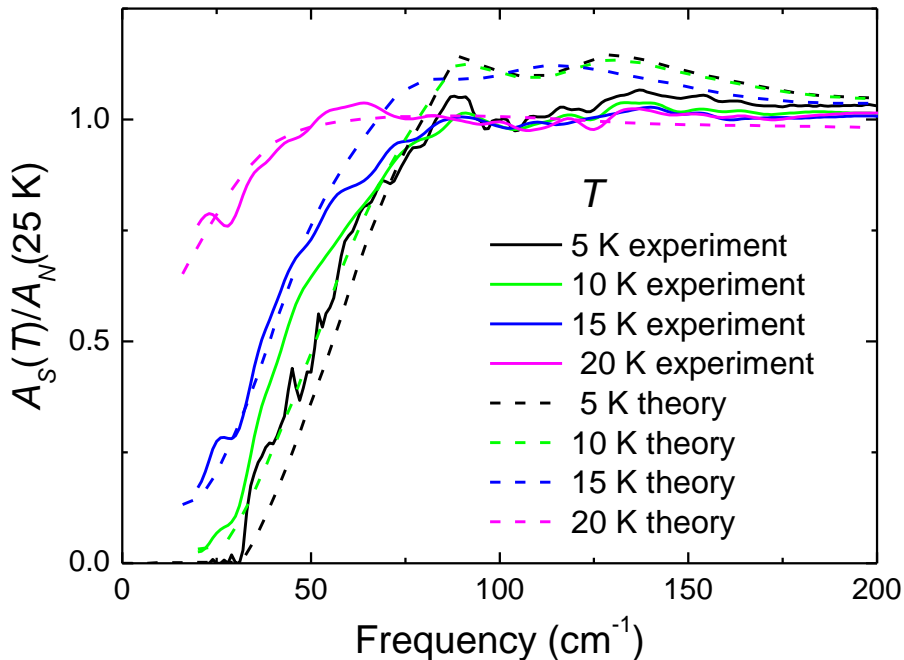


FIG. 5.11. Zimmermann's formalism for modeling the temperature dependent normalized absorption. Solid lines are temperature dependent infrared absorption in the superconducting state normalized to infrared absorption in the normal state at $T = 25\text{ K}$. Dashed lines are fits to the normalized infrared absorption data, using Zimmermann's formalism for the largest energy gap, and Mattis-Bardeen formalism for the two smaller energy gaps.

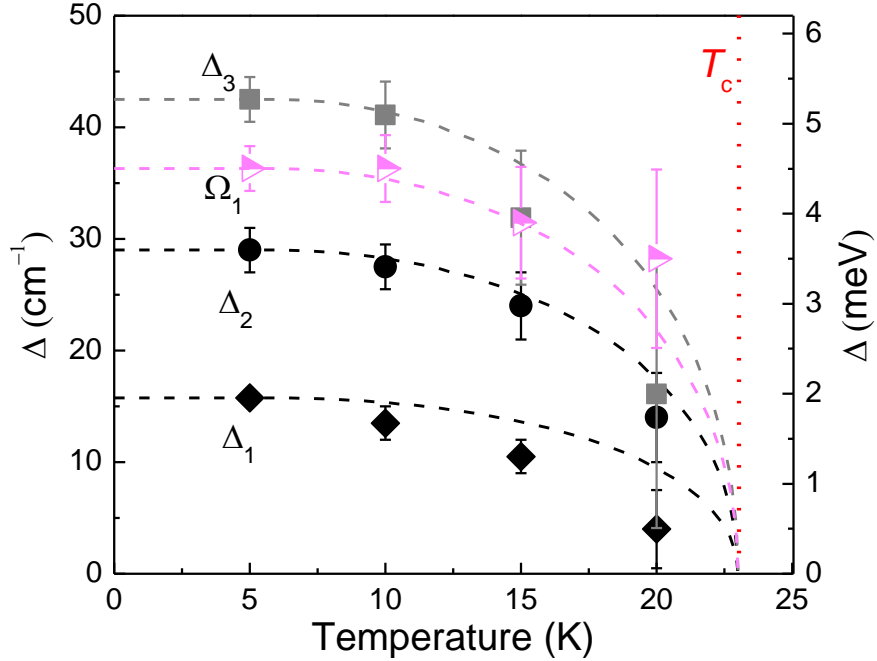


FIG. 5.12. Plot of the temperature dependence of the three energy gaps (filled symbols), and bosonic mode Ω_1 (half hollow symbols). The two smaller gaps are the same in Fig. 5.10(c), and the largest energy gap is derived from Zimmermann's model (gray square symbols). Note that there is a large error bar when temperature is high and close to T_c . The dashed lines are the BCS prediction of the temperature dependence of the energy gaps.

5.4 Summary

In summary, we have observed temperature dependent features in the infrared absorption spectra arising from the energy gaps and strong electron-boson interaction in the superconductor $\text{BaFe}_{1.9}\text{Pt}_{0.1}\text{As}_2$. The data is consistent with three nodeless energy gaps in the superconducting state, out of which only the largest gap is in the strong-coupling regime. We first obtain the electron-boson spectral density function by modeling the absorption data with the generalized Allen

formalism that relies on the optical self-energy method. The self-consistency of the largest gap, the T_c , and the electron-boson spectral density function was verified by solving the full Eliashberg equations. We then used Zimmermann's formalism in the strong-coupling regime and got comparable results with the Eliashberg function corresponding to the bosonic modes. We find that superconductivity in $\text{BaFe}_{1.9}\text{Pt}_{0.1}\text{As}_2$ arises primarily due to pairing of electrons induced by a bosonic mode centered at 5.1 ± 0.6 meV. This bosonic mode may originate from spin fluctuations and requires further investigation.

CHAPTER 6

Conclusion and outlook

In this work, we have studied charge dynamics in the metallic and superconducting states of the electron-doped 122-type iron arsenides using infrared and optical spectroscopy at cryogenic temperatures. We obtained detailed optical measurements on three different electron-doped 122-type iron arsenide samples: $\text{Ca}_{0.8}\text{La}_{0.2}\text{Fe}_2\text{As}_2$, $\text{Ca}_{0.85}\text{Pr}_{0.15}\text{Fe}_2\text{As}_2$ and $\text{BaFe}_{1.9}\text{Pt}_{0.1}\text{As}_2$ single crystals.

Here we summarize the role of doping in the rare-earth (La and Pr) doped and Pt-doped systems. Besides suppressing the spin density wave phase and doping extra electrons, the rare-earth elements La and Pr have similar ionic radii to Ca and are doped on the Ca site, so they don't increase impurity scattering. In fact, compared to the parent compound UT CaFe_2As_2 [179], the scattering rate decreases upon rare-earth doping and so does the resistivity (the plasma

frequency remains nearly the same). The decrease of scattering rate may be due to a decrease in electron-electron interactions. Pt has a huge ionic radius and is directly doped into the conducting FeAs_4 layer, and therefore it increases impurity scattering compared to the parent compound BaFe_2As_2 . Doping Pt suppresses the spin-density-wave phase transition, and increases the scattering rate and the plasma frequency. Similar to Co-doped BaFe_2As_2 [20,76], the chemical potential increases, and as a consequence the electron Fermi surfaces grow and the hole Fermi surfaces shrink.

We observed UT-CT phase transition in $\text{Ca}_{0.85}\text{Pr}_{0.15}\text{Fe}_2\text{As}_2$ and the metallic-to-superconducting phase transition in $\text{BaFe}_{1.9}\text{Pt}_{0.1}\text{As}_2$. Through careful measurements and data analysis, we studied in detail the electron-electron interactions in the rare-earth doped CaFe_2As_2 and electron-boson interactions in Pt-doped BaFe_2As_2 .

In Chapter 4, using cryogenic FTIR spectroscopy and spectroscopic ellipsometry, we have obtained the frequency and temperature dependent *ab*-plane optical conductivity of crystals of rare-earth-doped CaFe_2As_2 . In the UT La-doped and Pr-doped CaFe_2As_2 , we found that these materials are not canonical Fermi liquids, and the dominant scattering mechanism is of electronic origin. We observed that the scattering rate reveals a dominant scattering channel quadratic

in temperature and frequency. We also find saturation of the scattering rate above 200 K near the Mott-Ioffe-Regel limit in UT La-doped and Pr-doped CaFe_2As_2 . The spectral weight of free charge carriers in the UT phase decreases with increasing temperature in a broad temperature range and is recovered at an energy scale of ~ 0.5 eV which is much larger than the Fermi energy scale. In the CT phase of Pr-doped CaFe_2As_2 , due to weakening of electronic correlations, we observe a decrease of the scattering rate and a decrease in mobile carrier density which is consistent with partial loss of the hole Fermi surfaces.

In Chapter 5, we report temperature dependent features directly in the infrared absorption spectra arising from the energy gaps and strong electron-boson interaction in the superconductor $\text{BaFe}_{1.9}\text{Pt}_{0.1}\text{As}_2$. This was enabled by careful, systematic cryogenic infrared reflectance measurements. This is an important achievement, since it is the first report on strong-coupling features directly observed in infrared absorption spectra without applying complicated analyses like Kramers-Kronig transformations. The data is consistent with three nodeless energy gaps in the superconducting state, out of which only the largest gap is in the strong-coupling regime. We applied both the Allen formalism and Zimmermann formalism (quantitative approaches) based on the Eliashberg theory, and modeled the temperature dependent, normalized infrared absorption in the superconducting

state. The largest energy gap, the T_c , and the electron-boson spectral density function (Eliashberg function) from both models are found to be self-consistent within Eliashberg theory. We find that superconductivity in $\text{BaFe}_{1.9}\text{Pt}_{0.1}\text{As}_2$ arises primarily due to pairing of electrons induced by a bosonic mode centered at 5.1 ± 0.6 meV. The frequency of this bosonic mode is too low for it to be of phonon origin, so we rule out the possibility of primary phonon-mediated pairing in this material. The bosonic mode may originate from spin fluctuations although we cannot rule out the role of orbital fluctuations or another mechanism.

In the future, more 122-type superconducting materials need to be studied. Careful and very accurate infrared experiments will be needed to uncover the electron-boson interaction features. The Allen formalism and Zimmermann formalism would be very helpful to identify the frequency of bosonic modes in 122-type iron arsenides. Also, in recent years, new types of iron arsenides have been discovered, for example, 112 type and 1144 type materials. These materials can also be studied using the methods discussed in this dissertation. Other experimental techniques, like inelastic neutron scattering on $\text{BaFe}_{1.9}\text{Pt}_{0.1}\text{As}_2$ to detect the spin resonance frequency would also be very useful for shedding light on the origin of the bosonic mode identified using infrared spectroscopy .

Appendices

Appendix A: Reflectance, ellipsometry, and data analysis to obtain *ab*-plane optical constants of $\text{Ca}_{0.8}\text{La}_{0.2}\text{Fe}_2\text{As}_2$ and $\text{Ca}_{0.85}\text{Pr}_{0.15}\text{Fe}_2\text{As}_2$

Fig. A1(a) and (b) show *ab*-plane reflectance spectra of $\text{Ca}_{0.8}\text{La}_{0.2}\text{Fe}_2\text{As}_2$ and $\text{Ca}_{0.85}\text{Pr}_{0.15}\text{Fe}_2\text{As}_2$ respectively. The rather high reflectance at low frequencies is clearly indicative of metallicity. There is no evidence of bulk superconductivity in the infrared reflectance. This is consistent with the report of very low volume fraction superconductivity in these materials [46]. The reflectance of the $\text{Ca}_{0.85}\text{Pr}_{0.15}\text{Fe}_2\text{As}_2$ crystal in the far- and mid- infrared region shows subtle changes across the structure collapse transition which are more obvious in the optical conductivity, as discussed in the main text. The reflectance spectra were obtained in the Bruker Vertex 80v FTIR spectrometer that is fitted with an ultra-high vacuum chamber designed in-house for use with a continuous flow liquid helium cryostat.

In single crystal samples, the absolute value of the dc resistivity has a systematic error due to the difficulty in precise measurements of the geometry of the crystals. We use Hagen-Rubens extrapolation of room temperature infrared reflectance to determine the absolute value of the room temperature dc conductivity (in Hagen-Rubens extrapolation, dc conductivity is the only fit parameter). Then relative dc resistivity data measured at lower temperatures (in Ref. [46]) are used to find absolute temperature dependent dc conductivities which are employed in Hagen-Rubens extrapolations of temperature dependent infrared reflectance for Kramers-Kronig analysis. Hence, the dc extension of the optical conductivity agrees well with measured dc conductivity.

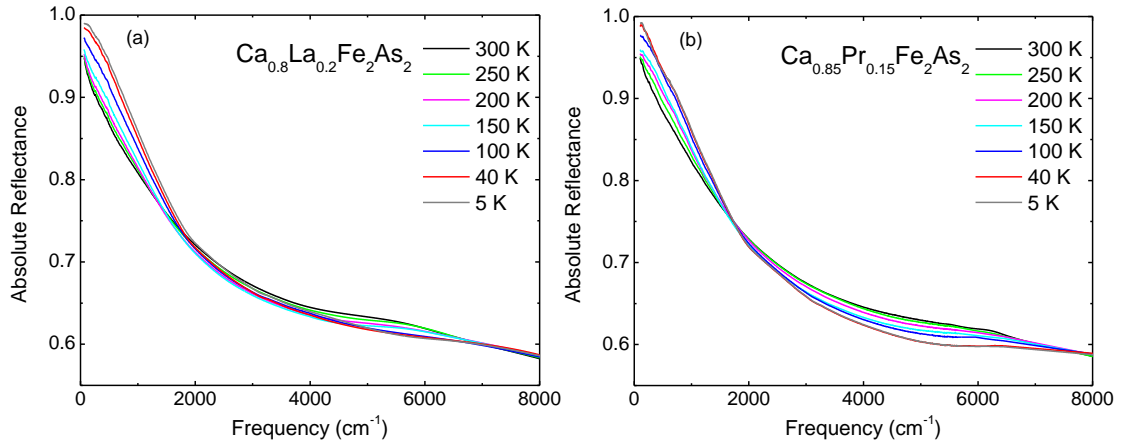


FIG. A1. Frequency dependence of absolute reflectance at representative temperatures for (a) $\text{Ca}_{0.8}\text{La}_{0.2}\text{Fe}_2\text{As}_2$ and (b) $\text{Ca}_{0.85}\text{Pr}_{0.15}\text{Fe}_2\text{As}_2$.

Frequency and temperature dependence of the ellipsometric coefficients Ψ

and Δ for $\text{Ca}_{0.8}\text{La}_{0.2}\text{Fe}_2\text{As}_2$ and $\text{Ca}_{0.85}\text{Pr}_{0.15}\text{Fe}_2\text{As}_2$ are shown in Fig. A2.

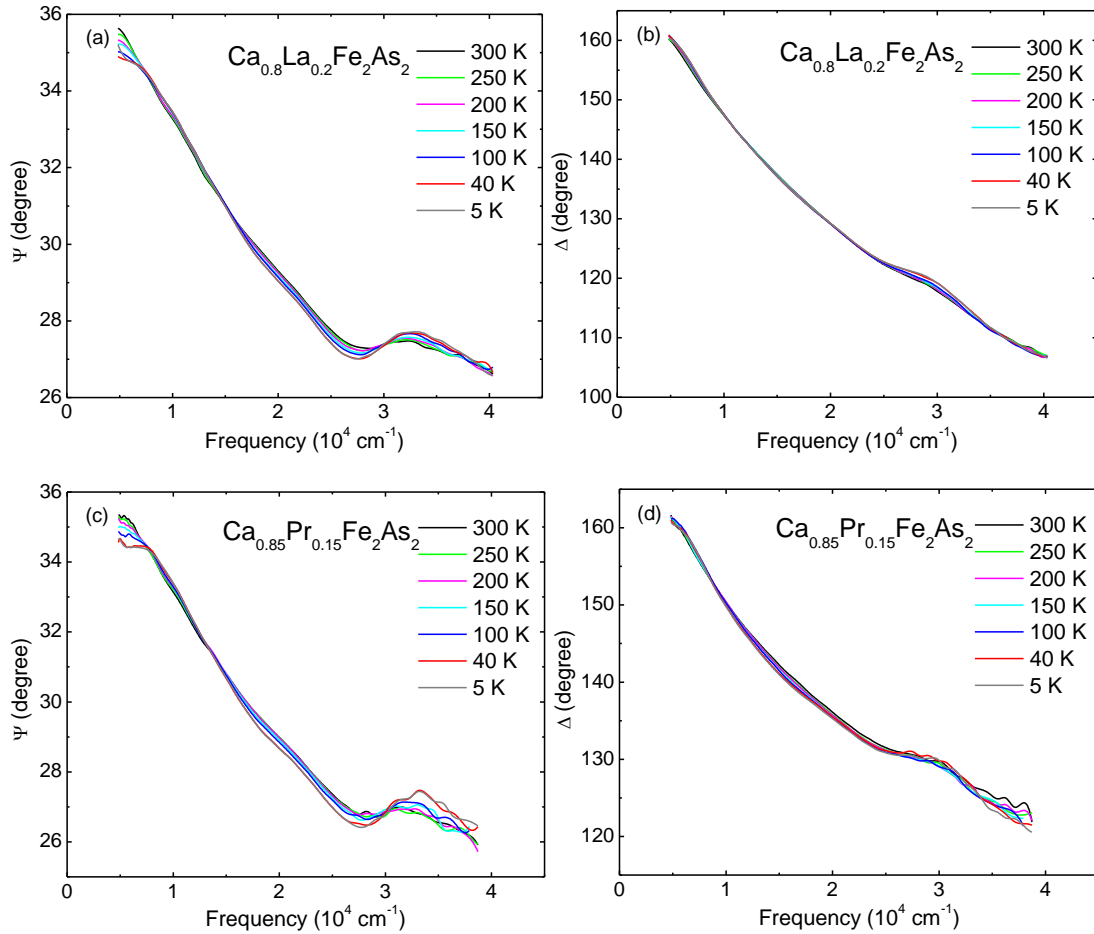


FIG. A2. (a) and (b) show frequency and temperature dependent ellipsometric coefficients Ψ and Δ for $\text{Ca}_{0.8}\text{La}_{0.2}\text{Fe}_2\text{As}_2$; (c) and (d) show frequency and temperature dependent ellipsometric coefficients Ψ and Δ for $\text{Ca}_{0.85}\text{Pr}_{0.15}\text{Fe}_2\text{As}_2$.

The ellipsometry data shown in Fig. A2 was obtained in an ultra-high vacuum chamber designed in-house for use with a continuous flow liquid helium cryostat and the Woollam VASE instrument. The pseudo-dielectric function calculated from

the ellipsometric coefficients of the rare-earth doped CaFe_2As_2 crystals with the c -axis normal to the crystal surface is nearly the same as the ab -plane optical constants. This is unlike the superconducting cuprates in which c -axis optical constants are quite different from ab -plane ones [180,181], and the pseudodielectric function for crystals with c -axis normal to the sample surface has to be corrected to obtain the ab -plane optical constants. In the 122 iron arsenides the ab -plane and c -axis optical conductivities differ by 20%-30% [182,183]. In the absence of c -axis optical spectroscopy data, it is reasonable for us to assume a similar level of anisotropy in the rare-earth doped CaFe_2As_2 . According to G. E. Jellison and J. S. Baba [184], for the special case like the measurements in principle symmetry directions (optical axis i.e. c -axis is perpendicular to the sample surface), the complex pseudodielectric function $\langle \varepsilon \rangle = \langle \varepsilon_1 \rangle - i\langle \varepsilon_2 \rangle$ measured directly from ellipsometry data can be expressed in terms of ε_{ab} and ε_c :

$$\langle \varepsilon \rangle = \sin^2 \varphi \left[1 + \sin^2 \varphi \left(\frac{\varepsilon_{ab}(\varepsilon_{ab} - \sin^2 \varphi)^{\frac{1}{2}} - \left[\frac{\varepsilon_{ab}(\varepsilon_c - \sin^2 \varphi)}{\varepsilon_c} \right]^{\frac{1}{2}}}{\varepsilon_{ab}(1 - \sin^2 \varphi) - (\varepsilon_{ab} - \sin^2 \varphi)^{\frac{1}{2}} \left[\frac{\varepsilon_{ab}(\varepsilon_c - \sin^2 \varphi)}{\varepsilon_c} \right]^{\frac{1}{2}}} \right)^2 \right] \quad (\text{A1})$$

where φ is the angle between beam and surface normal, ε_{ab} and ε_c are the ab -plane and c -axis complex dielectric functions respectively. The pseudodielectric function can be expressed by Taylor expansion in powers of $\Delta\varepsilon = \varepsilon_c - \varepsilon_{ab}$ (we keep three terms here):

$$\langle \varepsilon \rangle \approx \varepsilon_{ab} - \frac{\Delta\varepsilon}{\varepsilon_{ab}-1} + \frac{\Delta\varepsilon^2}{4\varepsilon_{ab}(\varepsilon_{ab}-1)^2} \frac{4\varepsilon_{ab}^2 - \varepsilon_{ab} - 3\varepsilon_{ab}\sin^2\varphi + \sin^2\varphi}{\varepsilon_{ab} - \sin^2\varphi} \quad (\text{A2})$$

According to our assumption, $\Delta\varepsilon / (\varepsilon_{ab}-1) \sim 20\%-30\%$ i.e. 0.2-0.3, so the third term of eq. (A2) which depends on the angle of incidence should be quite small (less than 1% for $\langle \varepsilon_2 \rangle$), and this is confirmed from our multiple angle of incidence ellipsometry measurements (as shown in Fig. A3). The pseudodielectric function we measured hardly shows any angle of incidence dependence. At 15000 cm^{-1} , $\langle \varepsilon_2 \rangle$ is about 10, which makes the contribution to $|\langle \varepsilon \rangle|$ of the term $\Delta\varepsilon / (\varepsilon_{ab}-1)$ about 2-3% at most. Also when $\langle \varepsilon_1 \rangle$ is small, both reflectance and phase used in Kramers-Kronig analysis based on Ref. [89] are mainly determined by $\langle \varepsilon_2 \rangle$. Above 15000 cm^{-1} to highest measured frequencies, the uncertainty in ab -plane ε_2 may be between 2% and 10% due to possible contribution to $\langle \varepsilon_2 \rangle$ from c -axis optical properties. However, this has negligibly small effect on calculations of ab -plane optical constants below 6000 cm^{-1} . Thus we can say $\langle \varepsilon \rangle \approx \varepsilon_{ab}$ i.e. the pseudodielectric function is the ab -plane dielectric function within the uncertainties stated above. In fact, the larger ε_{ab} the smaller the influence of the c -axis optical constants on the pseudodielectric function. So below $20,000 \text{ cm}^{-1}$ (where $\langle \varepsilon_2 \rangle$ is quite large), the pseudodielectric function we get directly from ellipsometry data is an accurate representation of the ab -plane dielectric function (within 3% uncertainty for ε_2), and correction due to c -axis optical properties is not necessary.

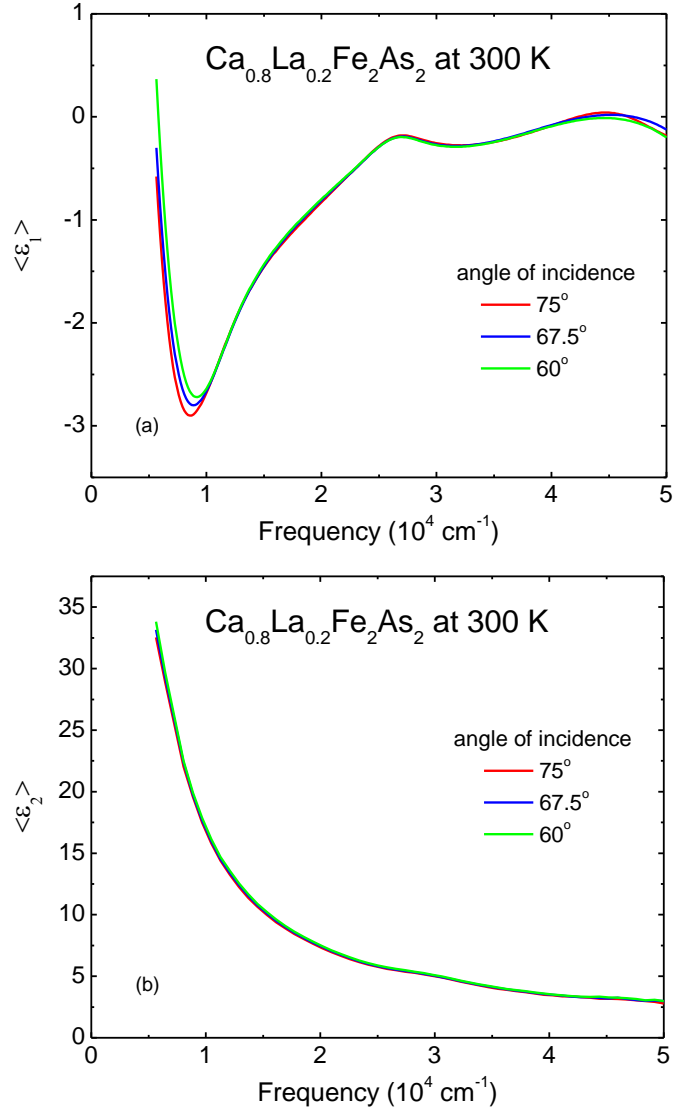


FIG. A3. (a) and (b) show the real and imaginary parts ($\langle \epsilon_1 \rangle$ and $\langle \epsilon_2 \rangle$) of the pseudo-dielectric function of $\text{Ca}_{0.8}\text{La}_{0.2}\text{Fe}_2\text{As}_2$ at room temperature for different angles of incidence.

Another piece of supporting evidence is that between 4800 cm^{-1} and 6400 cm^{-1} ($0.6\text{-}0.8 \text{ eV}$) *ab*-plane absolute reflectance we measured is remarkably consistent to within 0.5% of the reflectance generated from pseudodielectric function. For the purpose of performing Kramers-Kronig analysis on the infrared reflectance

constrained by ellipsometry data, we assume the reflectance generated from the ellipsometry data is more reliable (random uncertainty in reflectance generated from ellipsometric coefficients is about 0.2%). Next we adjust the *ab*-plane infrared reflectance in the range 4800-6000 cm^{-1} to match the reflectance generated from ellipsometric coefficients. The reflectance uncertainty in the range 4800-6000 cm^{-1} is around 0.5%, which leads to 1.5% uncertainty in conductivity in the same frequency range and even lower uncertainty of about 1% in the far infrared region. To summarize, the *ab*-plane optical conductivity below 6000 cm^{-1} we obtain from this method has a few percent systematic error at most, and the relative uncertainty for different temperatures is much smaller.

Appendix B: Phonon shift across CT phase transition in $\text{Ca}_{0.85}\text{Pr}_{0.15}\text{Fe}_2\text{As}_2$

Here we discuss the effect of the CT phase transition in $\text{Ca}_{0.85}\text{Pr}_{0.15}\text{Fe}_2\text{As}_2$ on the optical phonons. For the parent compound (space-group $I4/mmm$) CaFe_2As_2 , there are two *ab*-plane infrared-active E_u modes [185,186]. Both phonons have been observed in Pr-doped CaFe_2As_2 although the impact of the structural

transition is more clearly evident in the behavior of the higher frequency Fe-As vibration.

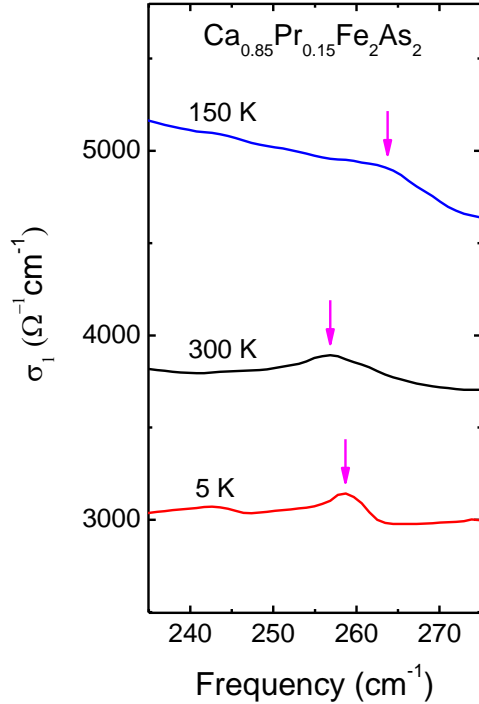


FIG. A4: Temperature dependence of the Fe-As phonon feature in the optical conductivity of $\text{Ca}_{0.85}\text{Pr}_{0.15}\text{Fe}_2\text{As}_2$. Arrows indicate the center frequencies of the phonon.

Fig. A4 shows the impact of structural collapse on the center frequency of the Fe-As phonon in $\text{Ca}_{0.85}\text{Pr}_{0.15}\text{Fe}_2\text{As}_2$. The phonon center frequency in the uncollapsed tetragonal (UT) phase increases as temperature decreases as in the 300 K and 150 K data. However, the center frequency of Fe-As phonon decreases below CT phase transition as seen in the 5 K data. This is direct evidence of the CT phase transition from infrared spectroscopy. We note that the feature at $\approx 140 \text{ cm}^{-1}$ in the conductivity of $\text{Ca}_{0.85}\text{Pr}_{0.15}\text{Fe}_2\text{As}_2$ (Fig. 4.1(b)) is attributed to the

phonon mode associated primarily with vibrations of the Ca ion. [186] We do not expect Pr doping to significantly affect this phonon feature because the ionic radius of the Pr ion is nearly the same as that of the Ca ion. Also, this phonon feature becomes weaker and possibly moves to $\approx 175 \text{ cm}^{-1}$ across the structural collapse into the CT phase (Fig. 4.1(b)). This phonon feature is much weaker in the conductivity data on $\text{Ca}_{0.8}\text{La}_{0.2}\text{Fe}_2\text{As}_2$. It is likely broadened out due to the lower concentration of Ca and the significant difference in the ionic radii of the Ca and La ions [46].

Appendix C: Representative fits of rare-earth doped CaFe_2As_2

Both the real and imaginary parts of the conductivity are fit well to the Drude-Lorentz model. Here we show and discuss the fits to the real part of the conductivity (σ_1). Fig. A5 shows a comparison of the fits to σ_1 at 40 K for $\text{Ca}_{0.8}\text{La}_{0.2}\text{Fe}_2\text{As}_2$ (UT phase) and $\text{Ca}_{0.85}\text{Pr}_{0.15}\text{Fe}_2\text{As}_2$ (CT phase). In the UT phase, one Drude mode and one Lorentz oscillator is sufficient for a good fit to the low frequency optical conductivity. Unlike the UT phase, another Lorentz oscillator (Lorentzian 2) is required to fit the hump in σ_1 around 400 cm^{-1} in the CT phase. The error bars of

Drude parameters plotted in Fig. 3 and Fig. 4 in the main text are calculated as follows. We manually vary each Drude parameter, while fitting the other parameters of the Drude and Lorentz modes, until the sum of the squared error between data and model increases by 10% of the best fit value.

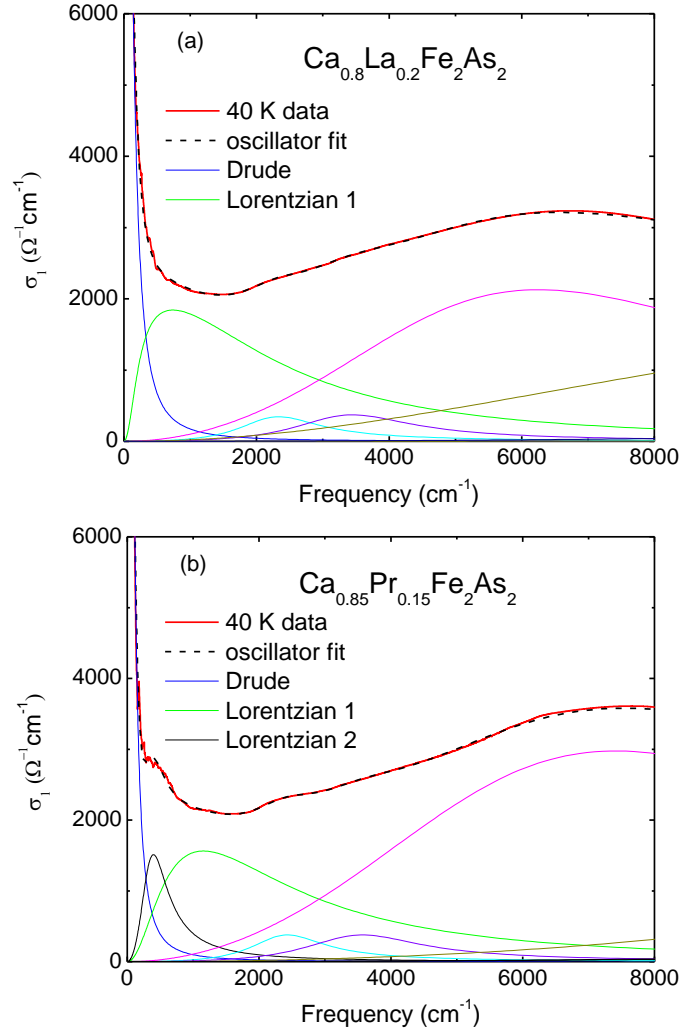


FIG. A5. Oscillator fits to the measured σ_1 at 40 K for (a) $\text{Ca}_{0.8}\text{La}_{0.2}\text{Fe}_2\text{As}_2$ and (b) $\text{Ca}_{0.85}\text{Pr}_{0.15}\text{Fe}_2\text{As}_2$. The thick solid line (red) is the data and the black dashed line is the sum of the Drude-Lorentz oscillators. The Drude and Lorentz oscillators used in the fits are shown as thin solid lines.

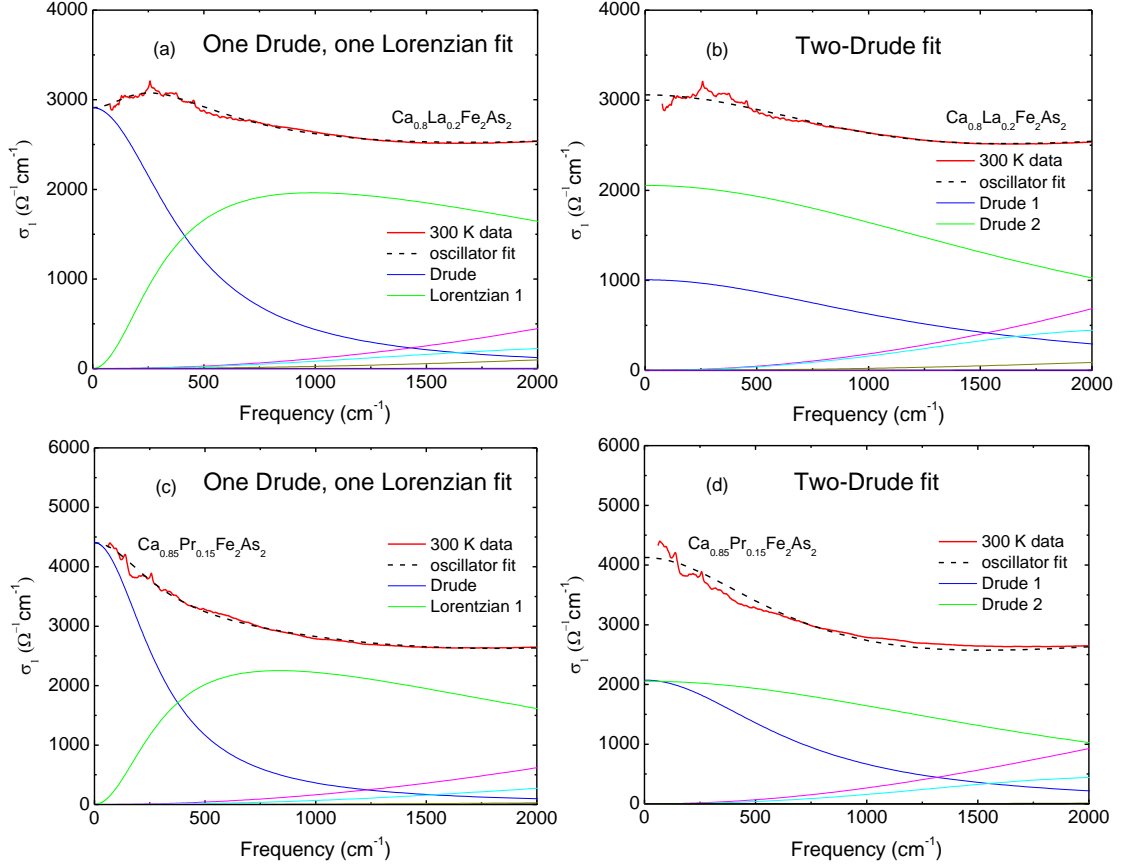


FIG. A6. (a) One Drude and one Lorentzian fit and (b) two-Drude fit to room temperature infrared conductivity of $\text{Ca}_{0.8}\text{La}_{0.2}\text{Fe}_2\text{As}_2$; (c) One Drude and one Lorentzian fit and (d) two-Drude fit to room temperature infrared conductivity of $\text{Ca}_{0.85}\text{Pr}_{0.15}\text{Fe}_2\text{As}_2$.

The one Drude-one Lorentzian fit and two-Drude fit (one broad and one narrow) to the low frequency, room temperature conductivity of La-doped and Pr-doped CaFe_2As_2 are shown in Fig. A6. In both materials, there is clear discrepancy between the data and the two-Drude fits for frequencies below 700 cm^{-1} . Especially for $\text{Ca}_{0.8}\text{La}_{0.2}\text{Fe}_2\text{As}_2$, due to the decreasing conductivity at very low frequencies, the two-Drude fits are emphatically ruled out. On the other hand, the one Drude-

one Lorentzian fits work well for the infrared data in the UT phase at room temperature and at all measured cryogenic temperatures.

Appendix D: Validation of the EPW 4.2 software

In order to make sure the EPW 4.2 software works properly when solving the isotropic Eliashberg equations, we run a test calculation to obtain results that can be compared to published work. The isotropic Eliashberg functions on the imaginary energy axis can be written as:

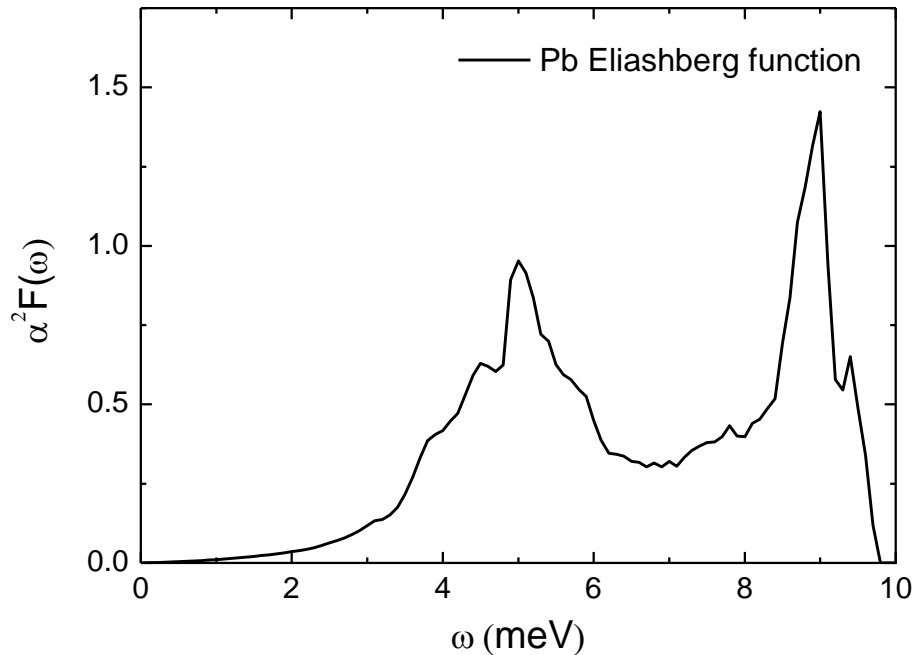


FIG. A7. Eliashberg function $\alpha^2 F(\Omega)$ of lead (Pb) used in the EPW to solve the isotropic Eliashberg equations. Data are taken from Ref. [187].

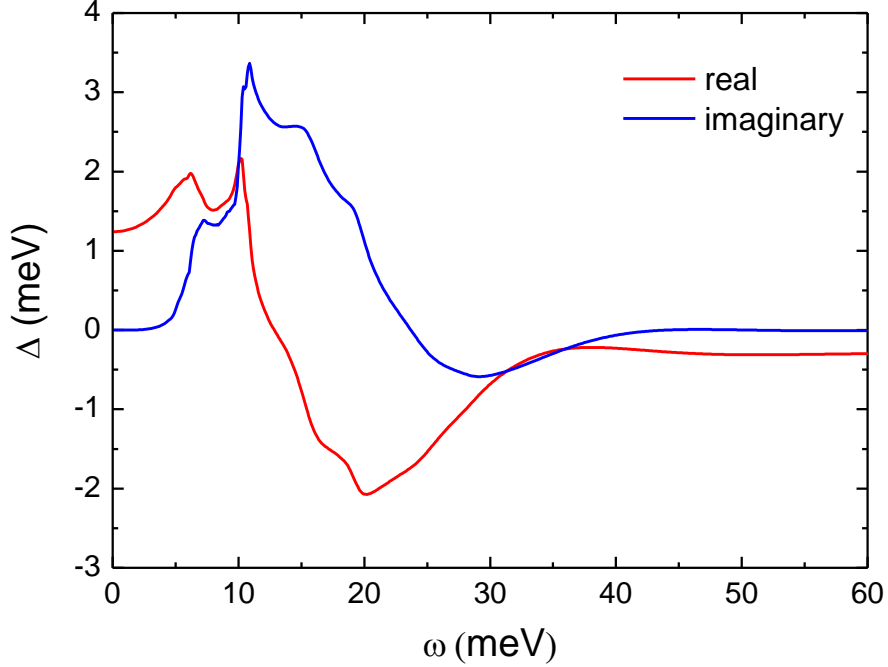


FIG. A8. Energy dependent complex superconducting energy gap function of lead calculated using EPW. The gap is obtained by solving the isotropic Eliashberg equations with $\mu^* = 0.1$ at $T = 0.3$ K. The superconducting gap is first solved on the imaginary energy axis and then iterative analytic continuation applied to obtain the solutions on the real energy axis.

$$Z(i\omega_n) = 1 + \frac{\pi T}{\omega_n} \sum_{n'} \frac{\omega_{n'}}{\sqrt{\omega_{n'}^2 + \Delta^2(i\omega_{n'})}} \lambda(n - n') \quad (\text{A1})$$

$$Z(i\omega_n)\Delta(i\omega_n) = \pi T \sum_{n'} \frac{\Delta(i\omega_{n'})}{\sqrt{\omega_{n'}^2 + \Delta^2(i\omega_{n'})}} [\lambda(n - n') - \mu^*] \quad (\text{A2})$$

$$\lambda(n - n') = \int_0^\infty d\omega \frac{2\omega\alpha^2 F(\omega)}{(\omega_n - \omega_{n'})^2 + \omega^2} \quad (\text{A3})$$

where $i\omega_n = i(2n + 1)T$ (n is integer) stands for the fermion Matsubara frequencies, and T is the absolute temperature. $\alpha^2 F(\omega)$ is the Eliashberg spectral function.

We follow Ref. [187] to repeat the calculations on superconducting lead (Pb). Fig. A7 shows the Eliashberg function $\alpha^2F(\omega)$ used in solving the Eliashberg equations. Data are digitized from Fig. 1 of Ref. [187]. The isotropic Eliashberg equations are solved at $T = 0.3$ K, with effective Coulomb pseudo-potential $\mu^* = 0.1$. The superconducting gap is first solved on the imaginary energy axis, then iterative analytic continuation applied to obtain the solutions on the real energy axis. The energy dependent complex superconducting gap function is shown in Fig. A8, which is identical with Fig. 2(b) in Ref. [187]. Hence, we have validated the EPW 4.2 software.

Bibliography

- [1] J. Bardeen, L. N. Cooper, and J. R. Schrieffer, *Phys. Rev.* **108**, 1175 (1957).
- [2] A. B. Migdal, *Sov. Phys. JETP* **34**, 996 (1958).
- [3] G. M. Eliashberg, *Sov. Phys. JETP* **11**, 696 (1960).
- [4] K. M. George Vlatakis, Lars I. Andersson, Ralf Muller, *Lett. to Nat.* **366**, 461 (1993).
- [5] Y. Kamihara, T. Watanabe, M. Hirano, and H. Hosono, *J. Am. Chem. Soc.* **130**, 3296 (2008).
- [6] Z. Ren, J. Yang, W. Lu, W. Yi, G. Che, X. Dong, L. Sun, and Z. Zhao, *Chinese Phys. Lett.* **967**, 2215 (2008).
- [7] J. Paglione and R. L. Greene, *Nat. Phys.* **6**, 645 (2010).
- [8] C. W. Chu, *Nat. Phys.* **5**, 787 (2009).
- [9] K. Kudo, Y. Kitahama, K. Fujimura, T. Mizukami, H. Ota, and M. Nohara, *J. Phys. Soc. Japan* **83**, 093705 (2014).
- [10] A. Iyo, K. Kawashima, T. Kinjo, T. Nishio, S. Ishida, H. Fujihisa, Y. Gotoh, K. Kihou, H. Eisaki, and Y. Yoshida, *J. Am. Chem. Soc.* **138**, 3410 (2016).
- [11] D. C. Johnston, *Adv. Phys.* **59**, 803 (2010).

- [12] Y. Mizuguchi, Y. Hara, K. Deguchi, S. Tsuda, T. Yamaguchi, K. Takeda, H. Kotegawa, H. Tou, and Y. Takano, *Supercond. Sci. Technol.* **23**, 054013 (2010).
- [13] F. jie Ma, Z. yi Lu, and T. Xiang, *Front. Phys. China* **5**, 150 (2010).
- [14] Z. R. Ye, Y. Zhang, F. Chen, M. Xu, J. Jiang, X. H. Niu, C. H. P. Wen, L. Y. Xing, X. C. Wang, C. Q. Jin, B. P. Xie, and D. L. Feng, *Phys. Rev. X* **4**, 031041 (2014).
- [15] C. Liu, T. Kondo, N. Ni, A. D. Palczewski, A. Bostwick, G. D. Samolyuk, R. Khasanov, M. Shi, E. Rotenberg, S. L. Bud'Ko, P. C. Canfield, and A. Kaminski, *Phys. Rev. Lett.* **102**, 167004 (2009).
- [16] J. Fink, S. Thirupathaiah, R. Ovsyannikov, H. A. Dürr, R. Follath, Y. Huang, S. de Jong, M. S. Golden, Y.-Z. Zhang, H. O. Jeschke, R. Valentí, C. Felser, S. Dastjani Farahani, M. Rotter, and D. Johrendt, *Phys. Rev. B* **79**, 155118 (2009).
- [17] M. Fuglsang Jensen, V. Brouet, E. Papalazarou, A. Nicolaou, A. Taleb-Ibrahimi, P. Le Fèvre, F. Bertran, A. Forget, and D. Colson, *Phys. Rev. B* **84**, 014509 (2011).

- [18] T. Shimojima, K. Ishizaka, Y. Ishida, N. Katayama, K. Ohgushi, T. Kiss, M. Okawa, T. Togashi, X. Y. Wang, C. T. Chen, S. Watanabe, R. Kadota, T. Oguchi, A. Chainani, and S. Shin, *Phys. Rev. Lett.* **104**, 057002 (2010).
- [19] V. Brouet, M. Marsi, B. Mansart, A. Nicolaou, A. Taleb-Ibrahimi, P. Le Fèvre, F. Bertran, F. Rullier-Albenque, A. Forget, and D. Colson, *Phys. Rev. B* **80**, 165115 (2009).
- [20] Y. Sekiba, T. Sato, K. Nakayama, K. Terashima, P. Richard, J. H. Bowen, H. Ding, Y. M. Xu, L. J. Li, G. H. Cao, Z. A. Xu, and T. Takahashi, *New J. Phys.* **11**, 025020 (2009).
- [21] C. Liu, G. D. Samolyuk, Y. Lee, N. Ni, T. Kondo, A. F. Santander-Syro, S. L. Bud'Ko, J. L. McChesney, E. Rotenberg, T. Valla, A. V. Fedorov, P. C. Canfield, B. N. Harmon, and A. Kaminski, *Phys. Rev. Lett.* **101**, 177005 (2008).
- [22] N. Ni, S. Nandi, A. Kreyssig, A. Goldman, E. Mun, S. Bud'ko, and P. Canfield, *Phys. Rev. B* **78**, 014523 (2008).
- [23] X. F. Wang, T. Wu, G. Wu, H. Chen, Y. L. Xie, J. J. Ying, Y. J. Yan, R. H. Liu, and X. H. Chen, *Phys. Rev. Lett.* **102**, 117005 (2009).

- [24] A. I. Goldman, D. N. Argyriou, B. Ouladdiaf, T. Chatterji, A. Kreyssig, S. Nandi, N. Ni, S. L. Bud'ko, P. C. Canfield, and R. J. McQueeney, *Phys. Rev. B* **78**, 100506(R) (2008).
- [25] M. Rotter, M. Tegel, and D. Johrendt, *Phys. Rev. B* **78**, 020503 (2008).
- [26] J.-Q. Yan, A. Kreyssig, S. Nandi, N. Ni, S. Bud'ko, A. Kracher, R. McQueeney, R. McCallum, T. Lograsso, A. Goldman, and P. Canfield, *Phys. Rev. B* **78**, 024516 (2008).
- [27] M. D. Lumsden and A. D. Christianson, *J. Phys. Condens. Matter* **22**, 203203 (2010).
- [28] T. Yildirim, *Phys. Rev. Lett.* **101**, 057010 (2008).
- [29] S. O. Diallo, V. P. Antropov, T. G. Perring, C. Broholm, J. J. Pulikkotil, N. Ni, S. L. Bud'ko, P. C. Canfield, A. Kreyssig, A. I. Goldman, and R. J. McQueeney, *Phys. Rev. Lett.* **102**, 187206 (2009).
- [30] S. A. J. Kimber, A. Kreyssig, Y.-Z. Zhang, H. O. Jeschke, R. Valenti, F. Yokaichiya, E. Colombier, J. Yan, T. C. Hansen, T. Chatterji, R. J. McQueeney, P. C. Canfield, A. I. Goldman, and D. N. Argyriou, *Nat. Mater.* **8**, 471 (2009).
- [31] K. Ishida, Y. Nakai, and H. Hosono, *J. Phys. Soc. Japan* **78**, 062001 (2009).

- [32] J. Zhao, D. T. Adroja, D.-X. Yao, R. Bewley, S. Li, X. F. Wang, G. Wu, X. H. Chen, J. Hu, and P. Dai, *Nat. Phys.* **5**, 555 (2009).
- [33] Z. P. Yin, K. Haule, and G. Kotliar, *Nat. Phys.* **7**, 294 (2011).
- [34] E. Bascones, B. Valenzuela, and M. J. Calderón, *Comptes Rendus Phys.* **17**, 36 (2016).
- [35] Y. Nakajima, R. Wang, T. Metz, X. Wang, L. Wang, H. Cynn, S. T. Wier, J. R. Jeffries, and J. Paglione, *Phys. Rev. B* **91**, 060508(R) (2015).
- [36] W. Yu, A. A. Aczel, T. J. Williams, S. L. Bud'ko, N. Ni, P. C. Canfield, and G. M. Luke, *Phys. Rev. B* **79**, 020511 (2009).
- [37] M. S. Torikachvili, S. L. Bud'ko, N. Ni, and P. C. Canfield, *Phys. Rev. Lett.* **101**, 057006 (2008).
- [38] A. I. Goldman, A. Kreyssig, K. Prokeš, D. K. Pratt, D. N. Argyriou, J. W. Lynn, S. Nandi, S. A. J. Kimber, Y. Chen, Y. B. Lee, G. Samolyuk, J. B. Leão, S. J. Poulton, S. L. Bud'ko, N. Ni, P. C. Canfield, B. N. Harmon, and R. J. McQueeney, *Phys. Rev. B* **79**, 024513 (2009).
- [39] D. K. Pratt, Y. Zhao, S. A. J. Kimber, A. Hiess, D. N. Argyriou, C. Broholm, A. Kreyssig, S. Nandi, S. L. Bud'ko, N. Ni, P. C. Canfield, R. J. McQueeney, and A. I. Goldman, *Phys. Rev. B* **79**, 060510 (2009).
- [40] S. Mandal, R. E. Cohen, and K. Haule, *Phys. Rev. B* **90**, 060501 (2014).

- [41] K. Gofryk, B. Sagarov, T. Durakiewicz, A. Chikina, S. Danzenbächer, D. V. Vyalikh, M. J. Graf, and A. S. Sefat, *Phys. Rev. Lett.* **112**, 186401 (2014).
- [42] R. Mittal, S. K. Mishra, S. L. Chaplot, S. V. Ovsyannikov, E. Greenberg, D. M. Trots, L. Dubrovinsky, Y. Su, T. Brueckel, S. Matsuishi, H. Hosono, and G. Garbarino, *Phys. Rev. B* **83**, 054503 (2011).
- [43] K. Zhao, Q. Q. Liu, X. C. Wang, Z. Deng, Y. X. Lv, J. L. Zhu, F. Y. Li, and C. Q. Jin, *Phys. Rev. B* **84**, 184534 (2011).
- [44] L. Harnagea, S. Singh, G. Friemel, N. Leps, D. Bombor, M. Abdel-Hafiez, A. U. B. Wolter, C. Hess, R. Klingeler, G. Behr, S. Wurmehl, and B. Büchner, *Phys. Rev. B* **83**, 094523 (2011).
- [45] S. Kasahara, T. Shibauchi, K. Hashimoto, Y. Nakai, H. Ikeda, T. Terashima, and Y. Matsuda, *Phys. Rev. B* **83**, 060505(R) (2011).
- [46] S. R. Saha, N. P. Butch, T. Drye, J. Magill, S. Ziemak, K. Kirshenbaum, P. Y. Zavalij, J. W. Lynn, and J. Paglione, *Phys. Rev. B* **85**, 024525 (2012).
- [47] S. R. Saha, T. Drye, S. K. Goh, L. E. Klintberg, J. M. Silver, F. M. Grosche, M. Sutherland, T. J. S. Munsie, G. M. Luke, D. K. Pratt, J. W. Lynn, and J. Paglione, *Phys. Rev. B* **89**, 134516 (2014).
- [48] T. Yildirim, *Phys. Rev. Lett.* **102**, 037003 (2009).

- [49] I. I. Mazin, D. J. Singh, M. D. Johannes, and M. H. Du, Phys. Rev. Lett. **101**, 057003 (2008).
- [50] H. Kontani and S. Onari, Phys. Rev. Lett. **104**, 157001 (2010).
- [51] F. Ning, K. Ahilan, T. Imai, A. S. Sefat, R. Jin, M. A. McGuire, B. C. Sales, and D. Mandrus, J. Phys. Soc. Japan **77**, 103705 (2008).
- [52] S. Graser, T. A. Maier, P. J. Hirschfeld, and D. J. Scalapino, New J. Phys. **11**, 25016 (2009).
- [53] T. Hanaguri, S. Niitaka, K. Kuroki, and H. Takagi, Science. **328**, 474 (2010).
- [54] M. L. Teague, G. K. Drayna, G. P. Lockhart, P. Cheng, B. Shen, H. H. Wen, and N. C. Yeh, Phys. Rev. Lett. **106**, 087004 (2011).
- [55] H. Ding, P. Richard, K. Nakayama, K. Sugawara, T. Arakane, Y. Sekiba, A. Takayama, S. Souma, T. Sato, T. Takahashi, Z. Wang, X. Dai, Z. Fang, G. F. Chen, J. L. Luo, and N. L. Wang, EPL **83**, 47001 (2008).
- [56] D. S. Inosov, J. T. Park, P. Bourges, D. L. Sun, Y. Sidis, A. Schneidewind, K. Hradil, D. Haug, C. T. Lin, B. Keimer, and V. Hinkov, Nat. Phys. **6**, 178 (2010).
- [57] A. D. Christianson, E. A. Goremychkin, R. Osborn, S. Rosenkranz, M. D. Lumsden, C. D. Malliakas, I. S. Todorov, H. Claus, D. Y. Chung, M. G. Kanatzidis, R. I. Bewley, and T. Guidi, Nature **456**, 930 (2008).

- [58] C. W. Hicks, T. M. Lippman, M. E. Huber, Z. A. Ren, J. Yang, Z. X. Zhao, and K. A. Moler, *J. Phys. Soc. Japan* **78**, 013708 (2009).
- [59] X. Zhang, Y. S. Oh, Y. Liu, L. Yan, K. H. Kim, R. L. Greene, and I. Takeuchi, *Phys. Rev. Lett.* **102**, 147002 (2009).
- [60] C.-T. Chen, C. C. Tsuei, M. B. Ketchen, Z.-A. Ren, and Z. X. Zhao, *Nat. Phys.* **6**, 260 (2010).
- [61] F. Wang and D.-H. Lee, *Science*. **332**, 200 (2011).
- [62] F. F. Tafti, A. Juneau-Fecteau, M.-È. Delage, S. René de Cotret, J.-P. H. . Reid, A. F. Wang, X.-G. . Luo, X. H. Chen, N. Doiron-Leyraud, and L. Taillefer, *Nat. Phys.* **9**, 349 (2013).
- [63] D. Guterding, S. Backes, H. O. Jeschke, and R. Valentí, *Phys. Rev. B* **91**, 140503(R) (2015).
- [64] P. M. R. Brydon, M. Daghofer, C. Timm, and J. van den Brink, *Phys. Rev. B* **83**, 060501(R) (2011).
- [65] L. Boeri, O. V Dolgov, and A. A. Golubov, *Phys. Rev. Lett.* **101**, 026403 (2008).
- [66] L. Boeri, M. Calandra, I. I. Mazin, O. V. Dolgov, and F. Mauri, *Phys. Rev. B* **82**, 020506(R) (2010).

- [67] P. J. Hirschfeld, M. M. Korshunov, and I. I. Mazin, *Rep. Prog. Phys.* **74**, 124508 (2011).
- [68] N.-L. Wang, H. Hosono, and P. Dai, *Iron-Based Superconductors: Materials, Properties and Mechanisms* (Pan Stanford Publishing, 2012).
- [69] K. Kuroki, S. Onari, R. Arita, H. Usui, Y. Tanaka, H. Kontani, and H. Aoki, *Phys. Rev. Lett.* **101**, 087004 (2008).
- [70] K. Jin, N. P. Butch, K. Kirshenbaum, J. Paglione, and R. L. Greene, *Nature* **476**, 73 (2011).
- [71] P. Monthoux, D. Pines, and G. G. Lonzarich, *Nature* **450**, 1177 (2007).
- [72] S. Onari and H. Kontani, *Phys. Rev. Lett.* **103**, 177001 (2009).
- [73] K. W. Kim, M. Rössle, A. Dubroka, V. K. Malik, T. Wolf, and C. Bernhard, *Phys. Rev. B* **81**, 214508 (2010).
- [74] Y. M. Dai, B. Xu, B. Shen, H. H. Wen, X. G. Qiu, and R. P. S. M. Lobo, *EPL* **104**, 47006 (2013).
- [75] A. Charnukha, O. V. Dolgov, A. A. Golubov, Y. Matiks, D. L. Sun, C. T. Lin, B. Keimer, and A. V. Boris, *Phys. Rev. B* **84**, 174511 (2011).
- [76] K. Terashima, Y. Sekiba, J. H. Bowen, K. Nakayama, T. Kawahara, T. Sato, P. Richard, Y.-M. Xu, L. J. Li, G. H. Cao, Z.-A. Xu, H. Ding, and T. Takahashi, *Proc. Natl. Acad. Sci.* **106**, 7330 (2009).

- [77] P. Szabó, Z. Pribulová, G. Pristáš, S. L. Bud'ko, P. C. Canfield, and P. Samuely, *Phys. Rev. B* **79**, 012503 (2009).
- [78] P. Samuely, Z. Pribulová, P. Szabó, G. Pristáš, S. L. Bud'ko, and P. C. Canfield, *Phys. C* **469**, 507 (2009).
- [79] L. Shan, Y. L. Wang, J. Gong, B. Shen, Y. Huang, H. Yang, C. Ren, and H. H. Wen, *Phys. Rev. B* **83**, 060510(R) (2011).
- [80] L. Shan, Y.-L. Wang, B. Shen, B. Zeng, Y. Huang, A. Li, D. Wang, H. Yang, C. Ren, Q.-H. Wang, S. H. Pan, and H.-H. Wen, *Nat. Phys.* **7**, 325 (2011).
- [81] D. S. Inosov, J. T. Park, A. Charnukha, Y. Li, A. V. Boris, B. Keimer, and V. Hinkov, *Phys. Rev. B* **83**, 214520 (2011).
- [82] https://en.wikipedia.org/wiki/Fourier-Transform_infrared_spectroscopy.
- [83] P. R. Griffiths and J. A. de Haseth, *Fourier Transform Infrared Spectrometry*, Second Edi (John Wiley & Sons, Inc., Hoboken, New Jersey, 2007).
- [84] M. Dressel and G. Grüner, *Electrodynamics of Solids* (Cambridge University Press, Cambridge, 2002).
- [85] F. Wooten, *Optical Properties of Solids* (Academic Press, Inc., New York and London, 1972).
- [86] J. Hwang, T. Timusk, and G. D. Gu, *J. Phys. Condens. Matter* **19**, (2007).

- [87] D. Neubauer, A. V. Pronin, S. Zapf, J. Merz, H. S. Jeevan, W.-H. Jiao, P. Gegenwart, G.-H. Cao, and M. Dressel, *Phys. Status Solidi* **254**, 1600148 (2017).
- [88] G. Li, P. Zheng, N. L. Wang, Y. Z. Long, Z. J. Chen, J. C. Li, and M. X. Wan, *J. Phys. Condens. Matter* **16**, 6195 (2004).
- [89] I. Bozovic, *Phys. Rev. B* **42**, 1969 (1990).
- [90] Z. Xing, T. J. Huffman, P. Xu, A. J. Hollingshad, D. J. Brooker, N. E. Penthorn, M. M. Qazilbash, S. R. Saha, T. Drye, C. Roncaioli, and J. Paglione, *Phys. Rev. B* **94**, 064514 (2016).
- [91] <https://www.jawoollam.com/resources/ellipsometry-Tutorial/ellipsometry-Measurements>.
- [92] H. G. Tompkins and E. A. Irene, editors, *Handbook of Ellipsometry* (William Andrew, Inc., Norwich, NY, 2005).
- [93] A. Hollingshad, *Spectroscopic Ellipsometry and Cryogenic Capability*, College of William & Mary, 2014.
- [94] G. R. Stewart, *Rev. Mod. Phys.* **83**, 1589 (2011).
- [95] J. Paglione and R. L. Greene, *Nat. Phys.* **6**, 645 (2010).
- [96] D. C. Johnston, *Adv. Phys.* **59**, 803 (2010).

- [97] T. Park, E. Park, H. Lee, T. Klimczuk, E. D. Bauer, F. Ronning, and J. D. Thompson, *J. Phys. Condens. Matter* **20**, 322204 (2008).
- [98] A. Kreyssig, M. A. Green, Y. Lee, G. D. Samolyuk, P. Zajdel, J. W. Lynn, S. L. Bud'ko, M. S. Torikachvili, N. Ni, S. Nandi, J. B. Leão, S. J. Poulton, D. N. Argyriou, B. N. Harmon, R. J. McQueeney, P. C. Canfield, and A. I. Goldman, *Phys. Rev. B* **78**, 184517 (2008).
- [99] P. L. Alireza, Y. T. C. Ko, J. Gillett, C. M. Petrone, J. M. Cole, G. G. Lonzarich, and S. E. Sebastian, *J. Phys. Condens. Matter* **21**, 012208 (2009).
- [100] K. Matsubayashi, N. Katayama, K. Ohgushi, A. Yamada, K. Munakata, T. Matsumoto, and Y. Uwatoko, *J. Phys. Soc. Japan* **78**, 073706 (2009).
- [101] W. Uhoya, A. Stemshorn, G. Tsoi, Y. K. Vohra, A. S. Sefat, B. C. Sales, K. M. Hope, and S. T. Weir, *Phys. Rev. B* **82**, 144118 (2010).
- [102] M. Danura, K. Kudo, Y. Oshiro, S. Araki, T. C. Kobayashi, and M. Nohara, *J. Phys. Soc. Jpn* **80**, 103701 (2011).
- [103] S. Kasahara, T. Shibauchi, K. Hashimoto, Y. Nakai, H. Ikeda, T. Terashima, and Y. Matsuda, *Phys. Rev. B* **83**, 060505 (2011).
- [104] K. Gofryk, M. Pan, C. Cantoni, B. Saparov, J. E. Mitchell, and A. S. Sefat, *Phys. Rev. Lett.* **112**, 047005 (2014).

- [105] H. Gretarsson, S. R. Saha, T. Drye, J. Paglione, J. Kim, D. Casa, T. Gog, W. Wu, S. R. Julian, and Y.-J. Kim, Phys. Rev. Lett. **110**, 047003 (2013).
- [106] L. Ma, G.-F. Ji, J. Dai, S. R. Saha, T. Drye, J. Paglione, and W.-Q. Yu, Chinese Phys. B **22**, 057401 (2013).
- [107] A. Sanna, G. Profeta, S. Massidda, and E. K. U. Gross, Phys. Rev. B **86**, 014507 (2012).
- [108] B. Lv, L. Deng, M. Gooch, F. Wei, Y. Sun, J. K. Meen, Y.-Y. Xue, B. Lorenz, and C.-W. Chu, Proc. Natl. Acad. Sci. U. S. A. **108**, 15705 (2011).
- [109] R. S. Dhaka, R. Jiang, S. Ran, S. L. Bud'ko, P. C. Canfield, B. N. Harmon, A. Kaminski, M. Tomić, R. Valentí, and Y. Lee, Phys. Rev. B **89**, 020511 (2014).
- [110] Y.-Z. Zhang, H. C. Kandpal, I. Opahle, H. O. Jeschke, and R. Valentí, Phys. Rev. B **80**, 094530 (2009).
- [111] D. F. Xu, D. W. Shen, J. Jiang, Z. R. Ye, X. Liu, X. H. Niu, H. C. Xu, Y. J. Yan, T. Zhang, B. P. Xie, and D. L. Feng, Phys. Rev. B **90**, 214519 (2014).
- [112] R. Yang, C. Le, L. Zhang, B. Xu, W. Zhang, K. Nadeem, H. Xiao, J. Hu, and X. Qiu, Phys. Rev. B **91**, 224507 (2015).
- [113] C. C. Homes, M. Reedyk, D. A. Cradles, and T. Timusk, Appl. Opt. **32**, 2976 (1993).

- [114] K. Takenaka, J. Nohara, R. Shiozaki, and S. Sugai, Phys. Rev. B **68**, 134501 (2003).
- [115] W. Z. Hu, J. Dong, G. Li, Z. Li, P. Zheng, G. F. Chen, J. L. Luo, and N. L. Wang, Phys. Rev. Lett. **101**, 257005 (2008).
- [116] J. J. Tu, J. Li, W. Liu, A. Punnoose, Y. Gong, Y. H. Ren, L. J. Li, G. H. Cao, Z. A. Xu, and C. C. Homes, Phys. Rev. B **82**, 174509 (2010).
- [117] D. Wu, N. Barišić, P. Kallina, A. Faridian, B. Gorshunov, N. Drichko, L. J. Li, X. Lin, G. H. Cao, Z. A. Xu, N. L. Wang, and M. Dressel, Phys. Rev. B **81**, 100512 (2010).
- [118] M. Nakajima, S. Ishida, K. Kihou, Y. Tomioka, T. Ito, Y. Yoshida, C. H. Lee, H. Kito, A. Iyo, H. Eisaki, K. M. Kojima, and S. Uchida, Phys. Rev. B **81**, 104528 (2010).
- [119] B. Cheng, B. F. Hu, R. Y. Chen, G. Xu, P. Zheng, J. L. Luo, and N. L. Wang, Phys. Rev. B **86**, 134503 (2012).
- [120] X. B. Wang, H. P. Wang, T. Dong, R. Y. Chen, and N. L. Wang, Phys. Rev. B **90**, 144513 (2014).
- [121] O. Gunnarsson, M. Calandra, and J. E. Han, Rev. Mod. Phys. **75**, 1085 (2003).

- [122] Y.-B. Huang, P. Richard, J.-H. Wang, X.-P. Wang, X. Shi, N. Xu, Z. Wu, A. Li, J.-X. Yin, T. Qian, B. Lv, C.-W. Chu, S.-H. Pan, M. Shi, and H. Ding, Chinese Phys. Lett. **30**, 017402 (2013).
- [123] N. E. Hussey, K. Takenaka, and H. Takagi, Philos. Mag. **84**, 2847 (2004).
- [124] P. L. Bach, S. R. Saha, K. Kirshenbaum, J. Paglione, and R. L. Greene, Phys. Rev. B **83**, 212506 (2011).
- [125] P. B. Allen, W. E. Pickett, and H. Krakauer, Phys. Rev. B **37**, 7482 (1988).
- [126] G. R. Parkins, W. E. Lawrence, and R. W. Christy, Phys. Rev. B **23**, 6408 (1981).
- [127] P. Xu, T. J. Huffman, N. C. Branagan, M. M. Qazilbash, P. Srivastava, T. Goehringer, G. Yong, V. Smolyaninova, and R. Kolagani, Philos. Mag. **95**, 2078 (2015).
- [128] X. Deng, A. Sternbach, K. Haule, D. N. Basov, and G. Kotliar, Phys. Rev. Lett. **113**, 246404 (2014).
- [129] N. Barišić, D. Wu, M. Dressel, L. J. Li, G. H. Cao, and Z. A. Xu, Phys. Rev. B **82**, 054518 (2010).
- [130] F. Rullier-Albenque, D. Colson, A. Forget, and H. Alloul, Phys. Rev. Lett. **103**, 057001 (2009).

- [131] C. C. Homes, A. Akrap, J. S. Wen, Z. J. Xu, Z. W. Lin, Q. Li, and G. D. Gu, Phys. Rev. B **81**, 180508 (2010).
- [132] M. M. Qazilbash, J. J. Hamlin, R. E. Baumbach, L. Zhang, D. J. Singh, M. B. Maple, and D. N. Basov, Nat. Phys. **5**, 647 (2009).
- [133] C. Berthod, J. Mravlje, X. Deng, R. Žitko, D. van der Marel, and A. Georges, Phys. Rev. B **87**, 115109 (2013).
- [134] A. Tytarenko, Y. Huang, A. de Visser, S. Johnston, and E. van Heumen, Sci. Rep. **5**, 12421 (2015).
- [135] S. I. Mirzaei, D. Stricker, J. N. Hancock, C. Berthod, A. Georges, E. van Heumen, M. K. Chan, X. Zhao, Y. Li, M. Greven, N. Barišić, and D. van der Marel, Proc. Natl. Acad. Sci. U. S. A. **110**, 5774 (2013).
- [136] A. Charnukha, P. Popovich, Y. Matiks, D. L. Sun, C. T. Lin, A. N. Yaresko, B. Keimer, and A. V. Boris, Nat. Commun. **2**, 219 (2011).
- [137] D. J. Scalapino, W. L. McMillan, and J. M. Rowell, in *Superconductivity*, edited by R. D. Parks (Marcel Dekker, Inc., New York, 1969), pp. 449–614.
- [138] R. Stedman, L. Almqvist, and G. Nilsson, Phys. Rev. **162**, 549 (1967).
- [139] R. R. Joyce and P. L. Richards, Phys. Rev. Lett. **24**, 1007 (1970).
- [140] Q. Si, R. Yu, and E. Abrahams, Nat. Rev. Mater. **1**, 16017 (2016).
- [141] S. Onari and H. Kontani, Phys. Rev. Lett. **109**, 137001 (2012).

- [142] S. Chi, A. Schneidewind, J. Zhao, L. W. Harriger, L. Li, Y. Luo, G. Cao, Z. Xu, M. Loewenhaupt, J. Hu, and P. Dai, *Phys. Rev. Lett.* **102**, 107006 (2009).
- [143] D. S. Inosov, J. T. Park, P. Bourges, D. L. Sun, Y. Sidis, A. Schneidewind, K. Hradil, D. Haug, C. T. Lin, B. Keimer, and V. Hinkov, *Nat. Phys.* **6**, 178 (2010).
- [144] M. D. Lumsden, A. D. Christianson, D. Parshall, M. B. Stone, S. E. Nagler, G. J. Macdougall, H. A. Mook, K. Lokshin, T. Egami, D. L. Abernathy, E. A. Goremychkin, R. Osborn, M. A. McGuire, A. S. Sefat, R. Jin, B. C. Sales, and D. Mandrus, *Phys. Rev. Lett.* **102**, 107005 (2009).
- [145] M. Eschrig, *Adv. Phys.* **55**, 47 (2006).
- [146] L. Shan, J. Gong, Y. Wang, B. Shen, X. Hou, C. Ren, C. Li, H. Yang, H. Wen, S. Li, and P. Dai, *Phys. Rev. Lett.* **108**, 227002 (2012).
- [147] P. Popovich, A. V. Boris, O. V. Dolgov, A. A. Golubov, D. L. Sun, C. T. Lin, R. K. Kremer, and B. Keimer, *Phys. Rev. Lett.* **105**, 027003 (2010).
- [148] M. P. Allan, K. Lee, A. W. Rost, M. H. Fischer, F. Masee, K. Kihou, C. Lee, A. Iyo, H. Eisaki, T. Chuang, J. C. Davis, and E. Kim, *Nat. Phys.* **11**, 177 (2015).
- [149] E. van Heumen, Y. Huang, S. de Jong, A. B. Kuzmenko, M. S. Golden, and D. van der Marel, *EPL* **90**, 37005 (2010).

- [150] E. G. Maksimov, A. E. Karakozov, B. P. Gorshunov, A. S. Prokhorov, A. A. Voronkov, E. S. Zhukova, V. S. Nozdrin, S. S. Zhukov, D. Wu, M. Dressel, S. Haindl, K. Iida, and B. Holzapfel, *Phys. Rev. B* **83**, 140502(R) (2011).
- [151] J. J. Tu, J. Li, W. Liu, A. Punnoose, Y. Gong, Y. H. Ren, L. J. Li, G. H. Cao, Z. A. Xu, and C. C. Homes, *Phys. Rev. B* **82**, 174509 (2010).
- [152] T. Fischer, A. V. Pronin, J. Wosnitza, K. Iida, F. Kurth, S. Haindl, L. Schultz, B. Holzapfel, and E. Schachinger, *Phys. Rev. B* **82**, 224507 (2010).
- [153] D. Wu, N. Barišić, M. Dressel, G. H. Cao, Z. A. Xu, J. P. Carbotte, and E. Schachinger, *Phys. Rev. B* **82**, 184527 (2010).
- [154] S. V. Dordevic, C. C. Homes, J. J. Tu, T. Valla, M. Strongin, P. D. Johnson, G. D. Gu, and D. N. Basov, *Phys. Rev. B* **71**, 104529 (2005).
- [155] E. Schachinger, D. Neuber, and J. P. Carbotte, *Phys. Rev. B* **73**, 184507 (2006).
- [156] S. J. Moon, A. A. Schafgans, S. Kasahara, T. Shibauchi, T. Terashima, Y. Matsuda, M. A. Tanatar, R. Prozorov, A. Thaler, P. C. Canfield, A. S. Sefat, D. Mandrus, and D. N. Basov, *Phys. Rev. Lett.* **109**, 027006 (2012).
- [157] S. J. Moon, Y. S. Lee, A. A. Schafgans, A. V. Chubukov, S. Kasahara, T. Shibauchi, T. Terashima, Y. Matsuda, M. A. Tanatar, R. Prozorov, A. Thaler,

- P. C. Canfield, S. L. Bud'ko, A. S. Sefat, D. Mandrus, K. Segawa, Y. Ando, and D. N. Basov, *Phys. Rev. B* **90**, 014503 (2014).
- [158] J. Yang, D. Huvonen, U. Nagel, T. Rõõm, N. Ni, P. C. Canfield, S. L. Bud'ko, J. P. Carbotte, and T. Timusk, *Phys. Rev. Lett.* **102**, 187003 (2009).
- [159] D. Wu, N. Barišić, M. Dressel, G. H. Cao, Z.-A. Xu, E. Schachinger, and J. P. Carbotte, *Phys. Rev. B* **82**, 144519 (2010).
- [160] J. Hwang, *J. Phys. Condens. Matter* **28**, 125702 (2016).
- [161] S. Ziemak, K. Kirshenbaum, S. R. Saha, R. Hu, J.-P. Reid, R. Gordon, L. Taillefer, D. Evtushinsky, S. Thirupathaiiah, B. Büchner, S. V Borisenko, A. Ignatov, D. Kolchmeyer, G. Blumberg, and J. Paglione, *Supercond. Sci. Technol.* **28**, 014004 (2015).
- [162] P. B. Allen, *Phys. Rev. B* **3**, 305 (1971).
- [163] W. Lee, D. Rainer, and W. ZIMMERMANN, *Phys. C* **159**, 535 (1989).
- [164] S. R. Saha, T. Drye, K. Kirshenbaum, N. P. Butch, P. Y. Zavalij, and J. Paglione, *J Phys Condens Matter* **22**, 72204 (2010).
- [165] X. Zhu, F. Han, G. Mu, P. Cheng, J. Tang, J. Ju, K. Tanigaki, and H.-H. Wen, *Phys. Rev. B* **81**, 104525 (2010).
- [166] A. Guler, M. Sertkol, L. Saribaev, M. Ozdemir, Y. Oner, and J. H. Ross, *IEEE Trans. Magn.* **51**, 1000504 (2015).

- [167] Y. F. Guo, J. J. Li, X. X. Wang, S. B. Zhang, A. A. Belik, K. Yamaura, and E. Takayama-Muromachi, *J. Phys. Conf. Ser.* **400**, 22138 (2012).
- [168] G. Li, W. Z. Hu, J. Dong, Z. Li, P. Zheng, G. F. Chen, J. L. Luo, and N. L. Wang, *Phys. Rev. Lett.* **101**, 107004 (2008).
- [169] K. Kamarás, S. L. Herr, C. D. Porter, N. Tache, D. B. Tanner, S. Etemad, T. Venkatesan, E. Chase, A. Inam, X. D. Wu, M. S. Hegde, and B. Dutta, *Phys. Rev. Lett.* **64**, 84 (1990).
- [170] D. C. Mattis and J. Bardeen, *Phys. Rev.* **111**, 412 (1958).
- [171] S. Poncé, E. R. Margine, C. Verdi, and F. Giustino, *Comput. Phys. Commun.* **209**, 116 (2016).
- [172] P. B. Allen and R. C. Dynes, *Phys. Rev. B* **12**, 905 (1975).
- [173] R. Akis, J. P. Carbotte, and T. Timusk, *Phys. Rev. B* **43**, 804 (1991).
- [174] A. Hinojosa, A. V. Chubukov, and P. Wölfle, *Phys. Rev. B* **90**, 104509 (2014).
- [175] M. Zbiri, H. Schober, M. R. Johnson, S. Rols, R. Mittal, Y. Su, M. Rotter, and D. Johrendt, *Phys. Rev. B* **79**, 064511 (2009).
- [176] D. Reznik, K. Lokshin, D. C. Mitchell, D. Parshall, W. Dmowski, D. Lamago, R. Heid, K.-P. Bohnen, A. S. Sefat, M. A. McGuire, B. C. Sales, D. G. Mandrus, A. Subedi, D. J. Singh, A. Alatas, M. H. Upton, A. H. Said, A. Cunsolo, Y. Shvyd'ko, and T. Egami, *Phys. Rev. B* **80**, 214534 (2009).

- [177] O. Delaire, M. S. Lucas, A. M. dos Santos, A. Subedi, A. S. Sefat, M. A. McGuire, L. Mauger, J. A. Muñoz, C. A. Tulk, Y. Xiao, M. Somayazulu, J. Y. Zhao, W. Sturhahn, E. E. Alp, D. J. Singh, B. C. Sales, D. Mandrus, and T. Egami, *Phys. Rev. B* **81**, 094504 (2010).
- [178] S. Onari and H. Kontani, *Phys. Rev. B* **84**, 144518 (2011).
- [179] Y. M. Dai, A. Akrap, S. L. Bud'ko, P. C. Canfield, and C. C. Homes, **94**, 195142 (2016).
- [180] S. L. Cooper, D. Reznik, A. Kotz, M. A. Karlow, R. Liu, M. V. Klein, W. C. Lee, J. Giapintzakis, D. M. Ginsberg, B. W. Veal, and A. P. Paulikas, *Phys. Rev. B* **47**, 8233 (1993).
- [181] D. N. Basov, S. I. Woods, A. S. Katz, E. J. Singley, R. C. Dynes, M. Xu, D. G. Hinks, C. C. Homes, and M. Strongin, *Science*. **283**, 49 (1999).
- [182] B. Cheng, Z. G. Chen, C. L. Zhang, R. H. Ruan, T. Dong, B. F. Hu, W. T. Guo, S. S. Miao, P. Zheng, J. L. Luo, G. Xu, P. Dai, and N. L. Wang, *Phys. Rev. B* **83**, 144522 (2011).
- [183] Z. G. Chen, T. Dong, R. H. Ruan, B. F. Hu, B. Cheng, W. Z. Hu, P. Zheng, Z. Fang, X. Dai, and N. L. Wang, *Phys. Rev. Lett.* **105**, 097003 (2010).
- [184] J. Jellison and J. S. Baba, *J. Opt. Soc. Am. A* **23**, 468 (2006).
- [185] M. Rende, Y. Li, Z. Bai, L. Wang, and L. Chen, *Phys. B* **405**, 4226 (2010).

[186] A. Charnukha, D. Pröpper, T. I. Larkin, D. L. Sun, Z. W. Li, C. T. Lin, T. Wolf,

B. Keimer, and A. V. Boris, Phys. Rev. B **88**, 184511 (2013).

[187] E. R. Margine and F. Giustino, Phys. Rev. B **87**, 024505 (2013).